Full Simulation of Detector Performance of Neutron Instrumentation at ESS

PhD Thesis

Milán Klausz

Supervisor : Dr. Péter Zagyvai
Consultants: Dr. Dávid Légrády
Prof. Dr. Richard Hall-Wilton

Centre for Energy Research
Budapest University of Technology and Economics
European Spallation Source ESS ERIC

Budapest
2020

Contents

List of Acronyms

BCS Boron-Coated Straws

DMSC Data Management and Software Centre

ESS European Spallation Source

FWHM Full Width at Half Maximum

ILL Institut Laue-Langevin

ISIS ISIS Neutron and Muon Source

J-PARC Japan Proton Accelerator Research Complex

MCNP Monte Carlo N-Particle

MCNPX Monte Carlo N-Particle eXtended

MCPL Monte Carlo Particle List

PHS Pulse-Height Spectra

PSC Pulse-Shaping Chopper

PSI Paul Scherrer Institute

SANS Small-Angle Neutron Scattering

SCS Scattering Characterisation System

SNS Spallation Neutron Source

ToF Time-of-Flight

Preamble

This thesis is the result of a four-year PhD work. During this time a lot of my friends and family members asked me what I actually do, having little understanding about neutrons scattering instruments or neutron detectors. Nonetheless, I was always keen to answer them, and they were mostly happy with my explanations. For this reason, in order to satisfy the curiosity of readers who are not experts in this field, in this preamble I intend to give an insight to the content of this thesis with barely any background knowledge required. To do so, I'll use my own somewhat far-fetched analogy drawn between the audiovisual experience of watching a movie in a cinema, and a scientific experiment in a neutron scattering facility.

Imagine a large cinema complex with as many as 20 auditoriums, in all of which movies are simultaneously played most of the day, almost every day of a year. A neutron scattering facility is similar to that in many ways, except that instead of auditoriums there are scientific instruments, and the movies played are actually scientific experiments on material samples to learn about their properties.

To have a satisfying experience while watching a movie, the auditoriums and the cinema complex itself have to comply with certain conditions. Everything has to stand on flat and steady ground, for example. In fact, the auditoriums have to be isolated from the outside world in all possible ways, not just from vibrations but from lights and sounds too. It is also true the other way around, the outside world should not be exposed to the constant loud noises and flashing lights from movies. Pedestrians just passing by the building might be okay with that, but people living close, or actually working at the cinema selling that delicious popcorn would certainly not. Of course movies are played simultaneously in several auditoriums, therefore they also have to be isolated from each other.

The analogy in this case stands for the elimination of vibrations that could ruin precise positioning, and protection against radiation that could be harmful both for people nearby, and for the experiments. The neutrons used in the experiments to probe samples are in fact one form of radiation, but their production and absorption are accompanied by other forms of radiation, e.g. photons similar to those used to make X-ray images but with generally higher energies.

It is photons with much lower energies that are used in cinemas to project frames of a film, photons of an energy range called visible light. The main concept of film projection is rather simple; a light source is placed behind a film that absorbs some of the light passing through it, and the remaining "transmitted" part forms an image on the movie screen. With high enough frame rate (frame per second) our visual system perceives the changes in subsequent images as motion.

The arrangement of experiments is quite similar to this. As the name suggests, in a neutron scattering experiment new information is gained about the sample by shooting neutrons at it and observing how they are scattered on it. It is therefore a neutron source that needs to be present behind the sample, and something must be placed after or more like around the sample to show how many neutrons are scattered on it in each direction. This something is called a "neutron detector", that can have several forms, but generally they can be thought of as an object that records how many neutrons enter it, and in most cases it also records the position where they enter. Usually plenty of detectors are used to cover a larger area around the sample, or several of them are moved around it, in order to show a picture of how neutrons are scattered on the sample, that can be related to its structural or dynamic properties on even the atomic scale.

There are numerous settings and parameters that all have to be adjusted correctly to make a movie look and sound like the director of the movie intended it. The speakers have to be well positioned, and the volume cannot be too loud or too quiet. The projector and the screen have to be aligned, with correct focusing and maybe with keystone correction to give sharp and undistorted picture. The light source of the projector cannot be too weak or too intense, otherwise the picture would be dim or too bright to look at. The film has to have a good physical quality, just as the screen. At first sight the screen does not seem like a complex component, however it has several important properties. It has to have the correct size and shape (mostly flat), and uniform surface. It has to have a surface that reflects as much light as possible, and do it uniformly, but should not have any afterglow effect like phosphorescence materials do. It has to be durable and maintain its quality preferably for decades, so that is does not need to be replaced unless there is some kind of upgrade.

There are many similarities in neutron scattering instruments. Precise positioning of all components including the sample and the detectors is essential. The neutron beam has to be focused on the sample, or sometimes on the detectors. The intensity of the neutron source has to be high enough to enable fast measurements but cannot be too high because the neutron detectors have finite count rate capability, that means

that there is a limit on how many neutrons they can record in a time unit. The sample has to have good quality, just as do the detectors. The detectors have to have high and uniform efficiency; that means that they have to be able to record as many of the incident neutrons as possible, regardless of their direction. The material selection of the detectors is important too, as depending on it more or fewer neutrons can get scattered on detectors that changes the information they carry about the sample. Materials also absorb neutrons, and some of them get radioactive after it, that can negatively impact the measurements, and prevent people from getting close to the detectors for maintenance.

The essence of the whole movie experience is, of course, the movie itself. It can be a cliche that shows nothing new, but it can also be something that has such a deep impact that it changes the way people think. There can be expectations beforehand, but one can only really know after watching it. Most movies were created to fit within the constraints of cinemas, however there are ideas that cannot be realised with presently existing tools. This is why 3D or IMAX appeared relatively recently, but there were many steps from silent black and white movies to current standards.

This is the case in science too, where the whole point of the facilities and instruments is to carry out experiments on samples that extend our knowledge of existing materials and also help develop new ones. These materials investigated impact every aspect of modern life. Capabilities of existing instruments cause limitations on some measurements, therefore instruments are being upgraded, and occasionally new research facilities are being built.

One such new facility is the European Spallation Source (ESS) mentioned in the title of the thesis, that is currently being built in Lund, Sweden. When finished, it will employ the brightest neutrons source in the world. A strong neutron source can be a nuclear (research) reactor, or as in the case of ESS, a spallation neutron sources where heavy elements like lead or tungsten are bombarded and exploded by high energy nuclei. The explosion of these elements containing lot of neutrons results in a vast number of free neutrons that can be used in the scattering experiments. This strong source and the new instruments designed to harness its power will enable measurements that were never done before. Just imagine them as movies recorded in such dark places that their films can be projected only with a really strong light source to have sufficient contrast to distinguish dark shapes from even darker ones.

On the other hand, using a cinematic quote: “with great power comes great responsibility”. The exceptional neutron intensity can exceed the rate capability of the neutron detectors. There are some samples which show interesting features only with

very low intensity, that necessitates the use of a strong neutron source to observe them, however from time to time they scatter an intense burst of neutrons in particular directions that can temporarily blind or even damage a detector. It is like a movie recorded in a dark cave that can only been watched using an intense light source, but with the sun suddenly appearing every now and then, that might burn a hole in the screen.

One way of preventing it from happening is using computer software to simulate new instruments in advance, and carry out virtual experiments to define what is the highest possible intensity that the detectors have to endure, so that only such detectors will be used that are capable of handling it. These simulation software tools are developed to mimic the ongoing physical processes in neutron experiments, but due to the immense complexity of such systems, they always use approximations. Therefore, they cannot replace real measurements on interesting new samples, but within certain uncertainties they can predict the outcome of experiments, and they can be used to estimate the major effects, and to identify and understand potential problems, like the occasional bursts on neutrons mentioned earlier. These tools can simulate not only the process of neutrons scattering on samples, but also the processes of how neutrons are detected in neutron detectors. This gives the opportunity to use them in the development of new detectors and characterisation of existing ones.

These are exactly the things that I had done during my PhD. Using such software I implemented simulation models for two neutron instruments that will be built at the ESS, named LoKI and BIFROST, and did virtual experiments on them. I simulated various samples including those that are expected to pose the greatest challenge for the detectors, and defined how many neutrons are expected to enter or be detected in each detector. I concluded in both cases that for some samples the number of neutrons entering the detectors per time unit will exceed the capability of detectors in certain moments. I also did a thorough study of the so-called "BCS detectors" that will be used at the LoKI instrument, as they are novel for neutron scattering applications. I defined how efficient they will be in detecting neutrons under different conditions, showed that the absorption of neutrons in the materials of the detectors, and the resulting radioactivity will be tolerable, and demonstrated how important the scattering of neutrons on these materials will be.

To shorty conclude, my PhD work and this thesis are all about the computer simulation of two future auditoriums named LoKI and BIFROST at the ESS cinema under construction, to help preventing their movie screens becoming the bottleneck hindering perfect movie experiences for visiting scientists.

Aims and objectives

Understanding the nature of materials is fundamental for many scientific fields such as engineering, physics, chemistry, geology, biology and medicine. Scientists probe the structure and behaviour of materials using different methods like microscopy, X-ray scattering and neutron scattering. Different techniques usually give complementary information about the observed sample of material due to the different interaction between the probing particles (e.g. photons, electrons, neutrons) and the building blocks of the sample.

Neutrons have the unique advantage of being able to penetrate bulky materials due to their weak interaction with atoms through the short-ranged nuclear force, and can provide information of even the atomic scales. On the other hand, this weak interaction is also a major drawback of the neutron scattering techniques, as it necessitates the use of powerful neutron sources with high fluxes which are not as easily accessible as for other techniques such as X-ray scattering. For this reason, scientific experiments involving neutron scattering techniques are concentrated in research facilities using strong neutron sources, that are mainly research reactors or spallation sources.

In order to push the boundaries of science, it is inevitable to upgrade scientific instruments and to build new facilities which exceed the capabilities of their predecessors. Both upgrading instrument at existing facilities and building new ones at new facilities require significant development in many fields of neutron scattering. This is especially true for the European Spallation Source (ESS), a new research facility being built in Lund, Sweden, that is designed to operate using the most powerful spallation neutron source in the world. Building ESS is one of the largest science and technology infrastructure projects today, and when finished, it will provide unprecedentedly high neutron fluxes for instruments of various neutron scattering techniques.

Harnessing this powerful neutron source carries a high potential risk for neutron intensities that can saturate the detectors and therefore degrade the performance of the instruments. In order to avoid the detectors becoming the bottleneck of the instrument's performance, Monte Carlo simulation studies can be carried out as part of the design process to serve basis for detector requirements.

In this PhD work multiple Monte Carlo simulation tools such as McStas and Geant4

are used together to implement full simulation models of two ESS instruments, namely LoKI and BIFROST. These models are used to define the anticipated detector rates for both instruments in various scenarios including those which are expected to result in the highest rates, and thus can help to formulate detector requirements. In case of the LoKI instrument, part of the simulation model is also used to perform a comprehensive characterisation of the novel Boron-Coated Straws (BCS) neutron detector technology to evaluate its performance and confirm its applicability for the LoKI instrument.

In this thesis the first two chapters are dedicated for the introduction of the scientific background, and the simulation tools and methods. In chapter 1 the ESS facility is briefly introduced, concentrating on information relevant for the two instrument of interest, LoKI and BIFROST, that are also introduced, along with the chosen detector technology of LoKI, the BCS detectors. In chapter 2, the simulation tools and methods used throughout the work are introduced, including the McStas and Geant4 simulation software, the McStas model of the two instruments implemented as part of the design process, and method of chaining different simulation tools.

In the following six chapters the implemented simulation models and the results acquired with them are presented. In chapter 3 the anticipated detector rates for the LoKI instrument are defined using the McStas model of the instrument, and a generic Geant4 model of a detector bank consisting of BCS detector tubes. Then, in chapters 4 and 5 the same Geant4 model is used to carry out a complex evaluation of the BCS detector performance, covering aspects such as conversion and detection efficiency, absorption, activation, and scattering effects. In chapter 6 the full simulation of the BIFROST instrument is demonstrated using a standard calibration sample with the pre-existing McStas model of the instrument and the Geant4 model of the full scattering characterisation system. After that, in chapter 7 the "worst-case" incident detector rates of the BIFROST instrument are defined in two ways, using McStas and Geant4, and a comparison of the two simulation tool is also provided. Finally, in chapter 8 a study of the incident detector rates of the BIFROST instrument is carried out with the parameter space including the sample and analyser mosaicity, sample size, and pulse-shaping chopper opening time, ended with the presentation of the incident detector rates in case of a representative operational scenario.

The thesis ends with the summary of the results in chapter 9, including the new scientific statements in the form of thesis points, an outlook on the afterlife of the presented work. Additional verification of the simulation results, and supplementary figures are presented in Appendix A and Appendix B respectively.

Chapter 1

Introduction

The European Spallation Source (ESS) [1–3] is designed to become the most powerful spallation neutron source in the world and the flagship of neutron science in the upcoming decades. The exceptionally high neutron flux will provide unique opportunities for scientific experiments, but also set high requirements for the detectors. One of the most challenging aspects is the rate capability and in particular the peak instantaneous rate capability, i.e. the number of neutrons hitting the detector per channel or cm^2 at the peak of the neutron pulse [4]. In order to design detectors and detector systems with the appropriate rate capability and prevent performance compromises on this front, a detailed analysis of the instrument requirements and how they translate to detector requirements is vital.

In this thesis the problems of detector rate capabilities and other detector requirements of neutron instrumentation are addressed by simulation studies of neutron scattering instruments and detectors. The subjects of the studies are two ESS instruments; namely the small-angle neutron scattering (SANS) instrument, LoKI [5, 6], and the indirect geometry cold neutron spectrometer, BIFROST [7, 8], as well as the chosen detector technology of LoKI, the Boron-Coated Straws (BCS) [9, 10] detector. To carry out such analyses, and to understand the relevance of this work, it is important to have general understanding of the scientific case and operation of these instruments, the BCS detector technology, and of the ESS itself. This chapter is dedicated to serve as introduction to the scientific background of the thesis.

In the following sections, first the most relevant aspects of the ESS research facility are presented, followed by the introduction of the LoKI instrument including the Boron-Coated Straws detector technology, and the introduction of the BIFROST instrument.

1.1 The European Spallation Source

The ESS [1–3] is a European Research Infrastructure Consortium (ERIC), a multidisciplinary research facility that aims be world-leading in neutron science. It is currently under construction in Lund, Sweden, where the instrument commissioning and the first user program will begin in 2022 and 2023 respectively, according to the current timeline.

The spallation source of ESS employs a linear accelerator delivering 2 GeV proton pulses of 2.86 ms length, with a repetition rate of 14 Hz. When used at the intended full power of 5 MW, it will be the world's most powerful accelerator [11]. The uniquely long proton pulses bombard a rotated tungsten target in which fast neutrons are produced by the spallation process. These neutrons are then slowed down from MeV to the sub-eV energy range by a special moderator assembly [12–14], that contains both water as thermal moderator, slowing down neutrons to thermal energies, and parahydrogen (the form of molecular hydrogen where the two proton spins are aligned antiparallel) as cold moderator, slowing down neutrons to cold energies. The geometry of the moderator assembly and the surrounding part of the target station is depicted in Figure 1.1, showing the simulation model used for the MCNPX [15] brightness calculations.

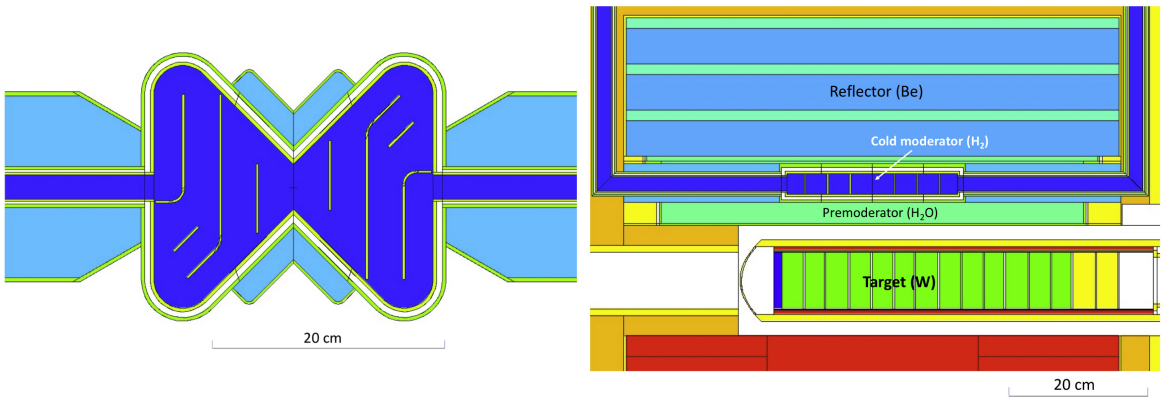

Figure 1.1: MCNPX geometry used for the brightness calculations.The top view of the moderator design (on left) shows the parahydrogen cold moderator (dark blue) and the water thermal moderator (light blue). The side view of the full geometry (on right) depicts the moderator in context, with the water premoderator (light green) below, and the beryllium reflector (light blue) including water channels (light green) above. The figure also the depicts proton target containing tungsten (green) and stainless steel (yellow) bombarded by protons from the left. From [13].

The eventual operational power of ESS is 5 MW, however, it will initially operate at 2 MW accelerator power. Nevertheless, the combination of the long proton pulse and the moderator assembly results in the brightest neutron source in the world even in this stage. The brightness of a neutron source is the number of neutrons emitted

per unit time, per unit solid angle, per unit energy (or wavelength), per unit area of the surface, that is a key parameter of neutron moderators. The great potential of ESS is illustrated in Figure 1.2 showing the brightness of the ESS cold moderator at a wavelength of 5 Å in one pulse, compared to today's world leading neutron research facilities.

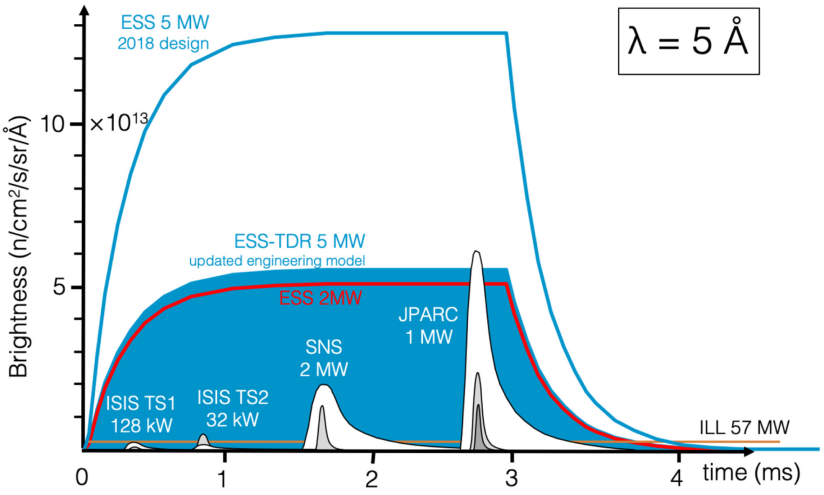

Figure 1.2: Time-dependent brightness of the ESS cold moderator at a wavelength of 5 Å. For comparison, the source brightness available at the neutron sources ISIS in the UK, SNS in the US, J-PARC in Japan, and ILL in France are shown for the moderators used for this wavelength. For ISIS, SNS and J-PARC, the pulse shapes of more than one moderator are shown, to illustrate the trade-off between resolution and intensity available there. For ESS, three pulse heights are shown: that corresponding to the Technical Design Report [1] moderator design (full blue), the current design at 5 MW of accelerator power (blue line), and at 2 MW (red line). From [3].

The target and the moderator assembly is surrounded by a monolith shielding designed with 42 beamports inserts, all available for bi-spectral extraction for thermal and cold neutrons. For the current foreseen scope of ESS, 22 of these beamports will be used to extract beams for neutron instruments, the remaining 20 will be sealed with temporary plugs, giving the opportunity for later expansion of the instrument suite. The target monolith is surrounded by a shielding structure, commonly referred to as the "bunker", that provides additional 3.5 m thick shielding wall to satisfy the low background requirements of the instruments, and encloses a common area with high dose rate requirement to install instrument components such as choppers.

As a result of the instrument selection process the proposal of 15 instruments are accepted, which will give the initial instrument suite of ESS. The layout of these 15 user instruments and a test beamline for characterising the moderator performance is depicted in Figure 1.3. The two instruments studied in this thesis and therefore introduced in details in the upcoming sections are LoKI, a SANS instrument located

in the north sector, and BIFROST, an indirect geometry spectrometer located in the west sector.

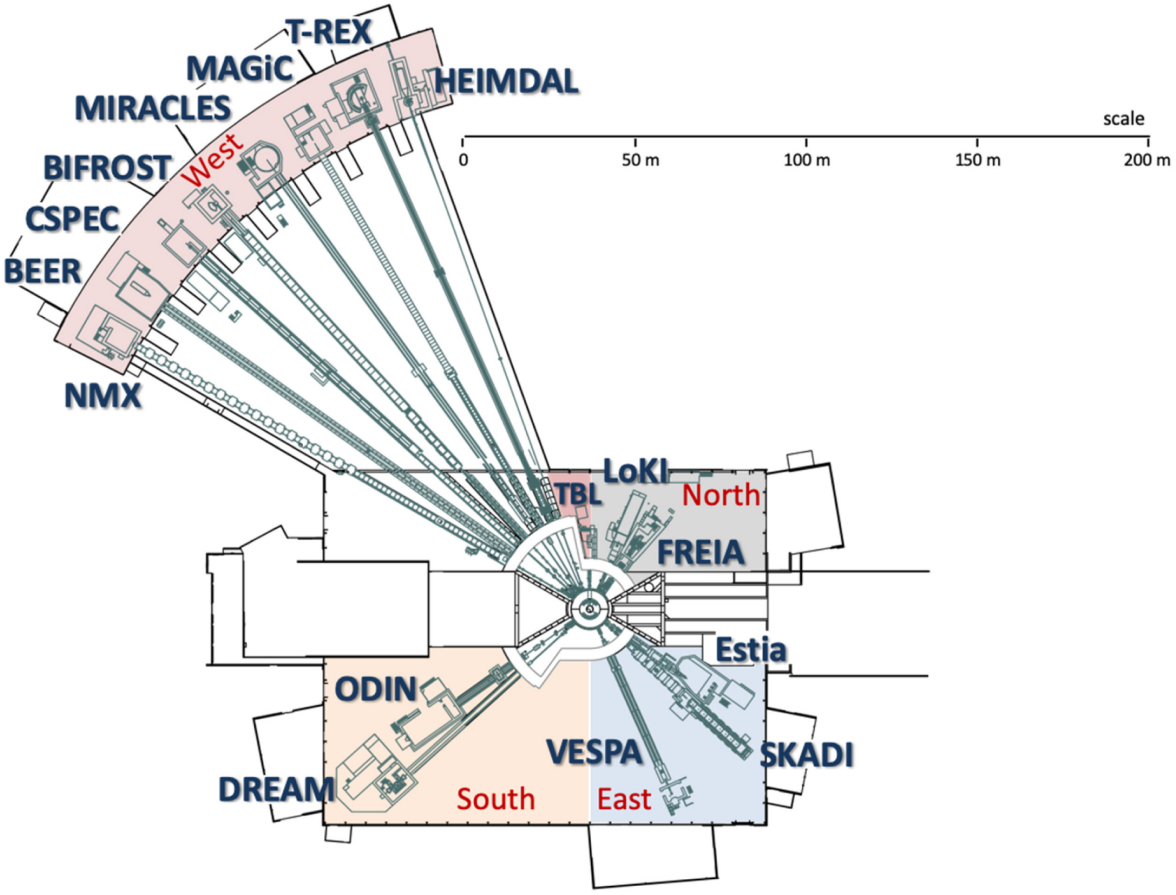

Figure 1.3: Layout of ESS initial instrument suite with 15 instruments and the test beamline (TBL). From [3]. The proton beam is incident from the right.

1.2 The LoKI instrument

SANS is one of the most widely used experimental techniques for the investigation of soft matter properties [16, 17]. It uses neutrons that are elastically scattered on the sample at small scattering angles to provide information about the size, shape and orientation of the components in the sample. Scattering takes place from aggregates of atoms, and the structural information one seeks is at a coarser level than the atomic sizes. The scale of the structures of interest that SANS can access is 1–100 nm.

As an elastic neutron scattering technique, the measured quantity in experiments is essentially the differential cross-section $d\sigma/d\Omega$ where σ is the cross-section, and Ω is the solid angle. The cross-section in general is a measure of probability that a specific

reaction will take place; the reaction being elastic or inelastic scattering in the case of scattering experiments; elastic scattering in the case of SANS.

One of the main applications of SANS is the study of nano-sized particles (e.g. large protein molecules, polymers or micelles), suspended in a solution (e.g. water or organic liquid). The fundamental equation of SANS for this application is presented in Equation 1.1, showing a general expression of the differential cross-section, explained in details in section *Small-angle neutron scattering* of [17].

$$\frac{d\sigma(Q)}{d\Omega} = N_p V_p^2 \overline{\rho}_p^2 P(Q) S(Q), \tag{1.1}$$

N_p and V_p are the number and volume of particles in the sample respectively. Q is the magnitude of the scattering vector given by $4\pi(\sin\Theta)/\lambda$ where 2Θ is the scattering angle, and λ is the neutron wavelength. The term $\overline{\rho}_p$ is the particle contrast given by $\overline{\rho}_p = \rho_V - \rho_S$ for scattering on particles dissolved or dispersed in a solvent where ρ_V and ρ_S are the average scattering length density within the volume V and the solvent respectively. $P(Q)$ and $S(Q)$ are the shape or form factor and the interparticle structure factor. They describe the influence of the shape of the scattering particle and the local order between the scattering particles on the measured cross-section respectively.

The strong dependence of the scattering cross-section on the contrast means that the scattered intensity can be changed strongly by varying the scattering length density of the solvent. The method exploiting this feature is the contrast variation, done mainly by using the difference in scattering length between hydrogen and deuterium. Systematically changing the D_2O/H_2O ratio of the solvent, and thereby the contrast, scattering on specific domains of the system under investigation can be enhanced at the same time as other domains are made practically invisible. This method is largely responsible for the success of SANS, making it a very powerful tool especially for studies of biological and pharmaceutical interest.

SANS instruments can also be used to study periodic crystalline arrangements with large enough lattice parameter, e.g. crystals of very large molecules, and magnetic structures with long repetition length.

The popularity of the SANS technique makes it a ubiquitous tool at every neutron scattering facility, usually with multiple instruments, targeting both at high availability for the scientific community, as well as satisfying complementary scientific requirements. For the same reason, two SANS instruments have been endorsed at ESS, LoKI [5, 6] and SKADI [18, 19].

LoKI (the Low-K Instrument) is a wide simultaneous Q range instrument designed primarily with the needs of the soft matter, biophysics and materials science communities in mind. The trend in all of these fields is towards complexity and heterogeneity.

Multi-component systems need to be studied as a function of multiple environmental conditions with different structures occurring at different length scales. Small gauge volumes are important to study both intrinsically small samples and for performing scans of heterogeneous samples. There is a need to study systems under the sort of non-equilibrium conditions, such as shear fields, found in real world applications. The ESS flux will enable more routine access of these conditions and also permit fast kinetic studies on a wider range of samples than is possible today. These scientific requirements motivate the requirements that the detector system have a large angular coverage, have decent spatial resolution, and have a high rate capability.

The layout of LoKI is depicted in Figure 1.4.

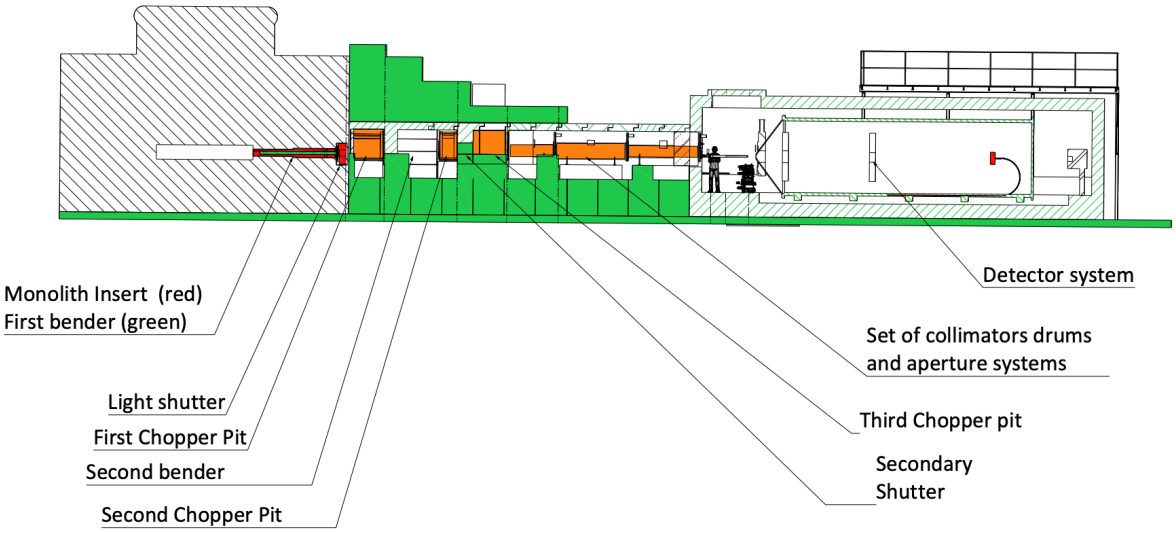

Figure 1.4: Schematic model of LoKI from source to detection position. From [20].

LoKI views at the cold moderator and employs a pair of benders, curved neutron guides used to bend the beam, located in the monolith and the bunker wall to get twice out of line-of-sight, meaning that due to the curvature there is no direct view to the neutron source, and thereby minimise high energy neutron background at the sample position. Two chopper pairs are used in the instrument, the first of being a 'bandwidth chopper' pair placed inside the bunker to select the required wavelength range, and the second pair being 'frame overlap choppers' placed right after the bunker wall to avoid signals from consecutive pulses to overlap. With different choppers settings a wavelength band of up to 10 Å at 14 Hz, and up to 20 Å at 7 Hz can be selected. The collimation section, employed to reduce the angular divergence of the neutron beam, consists of two moveable blocks, giving the possible collimation lengths of 8 m, 5 m, and 3 m, with 4-jaw slits used to define the beam size and position. After the collimation section a flight tube of adjustable length leads the neutrons to the sample position,

where a choice of 4-jaw slit or pre-defined apertures are available to match the beam size to sample requirements.

The detector system of LoKI, depicted in Figure 1.5 consist of multiple detector banks covering different scattering angles (Q-ranges) at different distances from the sample. The first two, the front and middle banks are placed at distances centred at ∼1.5 m and ∼3 m from the sample respectively, tilted slightly to maximise coverage. The rear bank, on the other hand is moveable between 5 m and 10 m from the sample.

The detector banks are composed of multiple overlapping layers of Boron-Coated Straws detectors, that are introduced in details in Section 1.2.1.

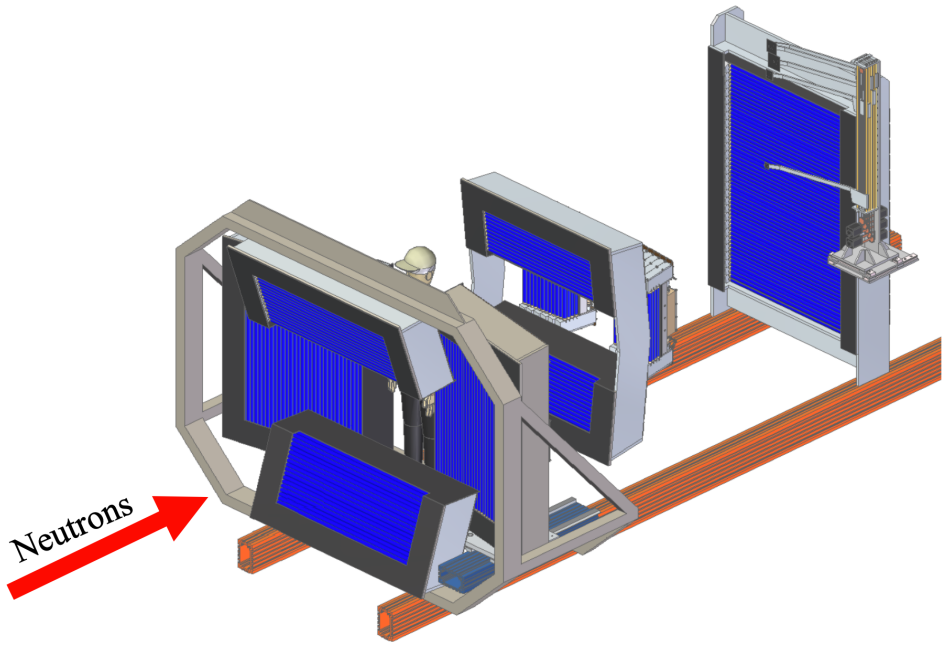

Figure 1.5: Detector layout of LoKI. From [21].

1.2.1 Boron-Coated Straws detector

For many years ^{3}He-based detectors have been dominant in the field of neutron scattering science, as they satisfied scientific requirements and ^{3}He was available in sufficient quantities at an affordable price. The situation has changed in recent years due to the worldwide ^{3}He crisis [22–24] that necessitated the development of alternative neutron detector technologies based on $^{10}B_4C$ [4, 10, 25–30], ^{6}LiF [31–33] and scintillators [34–41]. One of such ^{3}He replacement technologies is the Boron-Coated Straws (BCS) [9, 10], a position sensitive ^{10}B-based gaseous neutron detector developed by Proportional Technologies, Inc. (PTI) [42].

A BCS detector consists of a long thin-walled aluminium tube, containing seven copper straws arranged hexagonally with one in the centre (see Figure 1.6). The inner

wall of the straws is coated with a 1 μm thin B_4C converter layer enriched in ^{10}B by 95%. The straws are filled with an Ar/CO_2 mixture (90/10 by volume) at 0.7 atm. The basis of the neutron detection is the conversion of the incident electrically neutral neutrons in the converter layer into charged particles which can ionize the Ar/CO_2 gas.

Figure 1.6: Cross-sectional view of the BCS detector from [42]. The copper straws inside the aluminium tubes are exposed.

The underlying process in which the conversion products are created is the $^{10}B(n,\alpha)^7Li$ reaction detailed in Equation 1.2 with two branches.

$$ {}^{10}_{5}B + {}^{1}_{0}n \rightarrow \begin{cases} {}^{7}_{3}Li^{*} + {}^{4}_{2}\alpha \quad (94\%) \quad \text{Q=2.31 MeV} & \begin{matrix} \text{E}_{Li}\text{=0.84 MeV} \\ \text{E}_{\alpha}\text{=1.47 MeV} \end{matrix} \\ {}^{7}_{3}Li + {}^{4}_{2}\alpha \quad\quad (6\%) \quad \text{Q=2.79 MeV} & \begin{matrix} \text{E}_{Li}\text{=1.01 MeV} \\ \text{E}_{\alpha}\text{=1.78 MeV} \end{matrix} \end{cases} \tag{1.2} $$

In the less probable branch (with ~6% branching ratio) the kinetic energy of the ^{7}Li and α-particle that they can deposit in the counting gas is E_{Li}=1.01 MeV and E_α=1.78 MeV. In the main branch (with ~94% branching ratio) however the ^{7}Li is produced in an excited state, thereby the kinetic energy of the conversion products is lower, E_{Li}=0.84 MeV and E_α=1.47 MeV. During the de-excitation of $^7Li^*$, a photon is emitted with the energy of E_γ=0.48 MeV.

The neutron capture cross-section is much higher for thermal neutrons than in the high energy region, therefore in most cases the kinetic energy of the incident neutron is negligible compared to energy released in the nuclear reaction. According to the energy and momentum conservation laws this means that the ^{7}Li and α-particle leave in the opposite directions, therefore only one of them is expected to escape the converter layer. It is claimed that for 1 μm of B_4C, one of the two charged conversion products has a 78% probability to escape the converter and ionise the counting gas in the straw [43].

A bias voltage is applied between the tube and resistive Stablohm wires tensioned in the centre of each straw as anodes, making them work in proportional mode [44]. The charge is read out at both ends of the detector using charge division to acquire longitudinal position information along the straws.

The length and diameter of the straws, and therefore of the tubes, can vary depending on the application. It is claimed that a straw diameter of 2 mm up to 15 mm or even more can be achieved [10], but in most publications either 4 mm or 7.5 mm is used [43, 45, 46]. Generally, several BCS tubes are placed behind each other in successive layers in order to achieve the desired coverage, uniformity and detection efficiency.

The main application field of the BCS detectors is homeland security but they have the potential to be used as large area position-sensitive detectors for SANS and chopper spectrometers. This detector technology is novel to neutron scattering applications, it is therefore necessary to carefully evaluate its performance in order to avoid it becoming the bottleneck of the instrument's scientific performance.

1.3 The BIFROST instrument

Neutron spectroscopy is the study of dynamics in materials by inelastic neutron scattering [17]. The quantity measured in experiments is the double differential cross-section as a function of solid angle and scattered neutron energy. This has coherent and incoherent components, as shown in Equation 1.3:

$$\frac{d^2\sigma}{d\Omega dE_f} = \frac{d^2\sigma}{d\Omega dE_f}_{coherent} + \frac{d^2\sigma}{d\Omega dE_f}_{incoherent}, \tag{1.3}$$

where σ is the cross-section, Ω is the solid angle, and E_f is the final energy of the neutron after scattering. Scattering on the sample can be either coherent or incoherent and thus the differential cross-section can be divided into coherent and incoherent components. The coherent part depends on the correlation of the position of nuclei in the sample at different times, while the incoherent part depends on the correlation between the positions of the same nucleus at different times. The latter is only apparent in case of isotope or spin incoherence in the sample. Studying coherent inelastic scattering on a sample gives information about collective excitations like lattice vibrations (phonons) and spin waves (magnons), while incoherent inelastic scattering gives insight to non-collective excitations like internal molecular vibrations, and diffusion of atoms and molecules.

In inelastic neutron scattering both energy and momentum are transferred between the neutron and the sample, governed by the conservation laws, both carrying infor-

mation about the observed system. Measuring these quantities in experiments means defining the scattering angle, and both the initial and the final neutron energy. Three types of neutron spectroscopy are possible depending on how the scattering process is examined, using three types of spectrometers: triple-axis-spectrometers, and direct and indirect geometry time-of-flight spectrometers. Triple-axis-spectrometers are used with continuous neutron sources, where it is necessary to directly select both the initial and final neutron energies, done by crystal analysers, also commonly referred to as monochromator crystals. On instruments at pulsed sources it is possible to use neutron time-of-flight to determine either the initial or the final neutron energy or both, resulting in two different types of spectrometer geometries. On direct geometry time-of-flight spectrometers the incoming neutrons are monochromatized by a chopper system or crystal analysers and the neutron time-of-flight is used to determine final energy of the neutrons after scattering. On indirect geometry time-of-flight spectrometers a polychromatic "white" beam of neutrons hit the sample, the fixed final neutron energies are selected by crystal analysers, and it is the initial neutron energy that is calculated from the neutron time-of-flight. It is also an option to use the time-of-flight techniques at continuous sources, that is achieved by producing pulses by chopping the neutron beam.

Neutron spectroscopy is a powerful and versatile technique with applications is many research fields [17]. In molecular spectroscopy it is a complementary tool to the optical techniques of infrared and Raman spectroscopy, both of which are restricted by certain selection rules that do not allow the measurement of the full frequency spectrum of vibrational modes, as inelastic neutrons scattering does. The energy and wavelength of thermal neutrons are comparable to the thermal energy and spacing of the atoms in solids, inelastic scattering is therefore suitable for study of excitations in various single crystals, yielding in both the frequency spectrum of the lattice vibrations and the dependence of the frequencies on the wave vectors of the vibrations. Due to its magnetic dipole moment, the neutron can interact with the magnetic field inside materials, making it invaluable for investigation of magnetic excitations. Furthermore, the ability of neutrons to penetrate bulky materials enables measurements with complex sample environments.

Initially ESS will house 5 neutron spectrometers covering an excitation energy range of five orders of magnitude, from micro-eV to energies approaching the eV-range [3]. They will all greatly benefit from the world leading brightness of the ESS neutron source, that is immensely important for inelastic scattering signals which are inherently weak. The scientific case of these instruments overlap to some degree, however their

unique capabilities make them highly complementary. Two of these instruments are direct and three them are indirect geometry time-of-flight spectrometers.

The two direct geometry spectrometers are CSPEC [47], that focuses on the cold regime and the corresponding broad scientific profile of low energy excitations, and T-REX [48], that has a broader dynamic range and a scientific emphasis on magnetism. Three indirect geometry spectrometers are VESPA [49], a vibrational spectrometer with an emphasis on the energy range of primary importance to the study of functional groups in energy materials, MIRACLES [50], a high-resolution backscattering spectrometer that covers an energy transfer range that a uniquely large among backscattering instruments, and BIFROST [7, 8], the extreme environment cold spectrometer optimised for the study of single-crystal excitations at high magnetic fields and pressures.

BIFROST is a 162 m long instrument, that combines an indirect geometry time-of-flight (ToF) front end, and an angular and energy multiplexed crystal analyser-based back end. The envisioned application fields include materials science, life sciences, planetary sciences, and most importantly magnetism. It is designed [51] to maximise the use of the ESS long pulse to enable measurements on small samples and study their dynamic properties. The exceptional flux allows for entirely new options for detailed investigations of complex multimode dynamics, hybrid modes, electro-magnons, spin wave continua and gap studies, under extreme conditions with controlled temperature, pressure, and magnetic fields, as described in details in [3, 8].

The instrument consists of three main technical subsystems: the beam transport and conditioning system, the sample exposure system and the scattering characterisation system. The schematic model of the instrument is depicted in Figure 1.7.

The beam transport and conditioning system is relatively simple. It has a curved guide section inside the bunker to lose line-of-sight, and four choppers as the only moving parts. Three of these choppers are placed inside the bunker and the fourth one in placed in the middle of the instrument. The first one is a pulse-shaping chopper, that is the only chopper determining the energy resolution. The other three – two frame overlap and one bandwidth chopper – serve to sort out unwanted frames from the fast pulse-shaping chopper and to avoid pulse overlap at the sample position respectively. The use of the chopper system is illustrated in Figure 1.8. The pulse-shaping chopper can reduce the ESS pulse width by a factor of up to 30 to match the best analyser resolution, or allow the full pulse to reach the sample that will result in a relaxed resolution but an order of 10^{10} n/s/cm^2 flux on sample. It is this mode which poses the greatest rate challenge for the detectors.

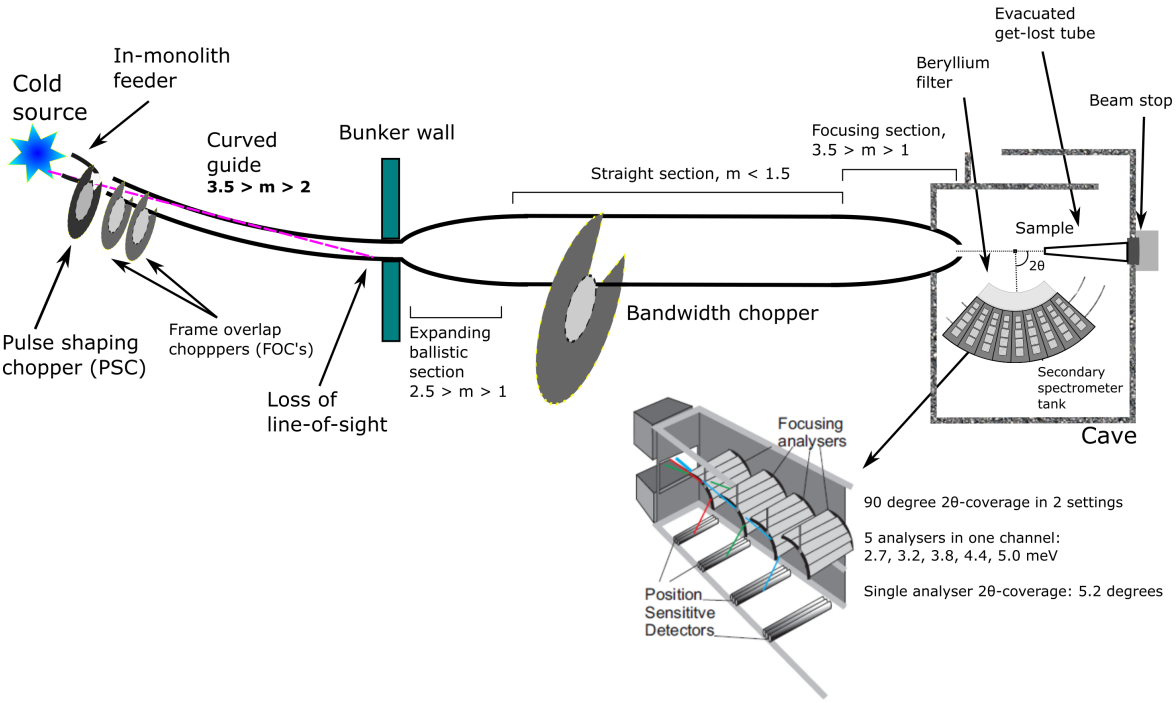

Figure 1.7: Schematic model of BIFROST from source to detection position. From [52].

The sample exposure system allows measurements with strong magnetic field, high pressure and cryogenic temperatures. One of the main limitations today in single crystal neutron spectroscopy is that measurements are only possible with large samples, which are not available for many sample types, but BIFROST will enable the study of sub-cubic millimetre samples thanks to its exceptional flux on sample and the efficient scattering characterisation system. Although the instrument is designed to facilitate measurements on small samples, dimensions up to 1.5 cm are possible.

The back end of BIFROST is similar in principle to that installed recently at the CAMEA spectrometer at the PSI facility [53, 54]. The scattering characterisation system in Figure 1.9 consists of the filtering system and the secondary spectrometer tank, covering a 90° scattering angle in the horizontal plane in two tank settings. The filtering system, that is essential for background reduction on BIFROST, includes a cooled beryllium filter with roughly 90% transmission of neutrons with an energy below 5 meV but very low transmission of neutrons with energies above, and coated lamellas as a radial collimator [55].

The secondary spectrometer tank houses multiple sets of analysers and detectors for different neutron energies, arranged in nine so called Q-channels, applying a variant of a novel analyser setup called CAMEA [53, 54], an acronym for Continuous Angle Multiple Energy Analysis. Depending on the scattering angle of a neutron on the sample, it enters one of the Q-channels, which cover distinct scattering angle ranges

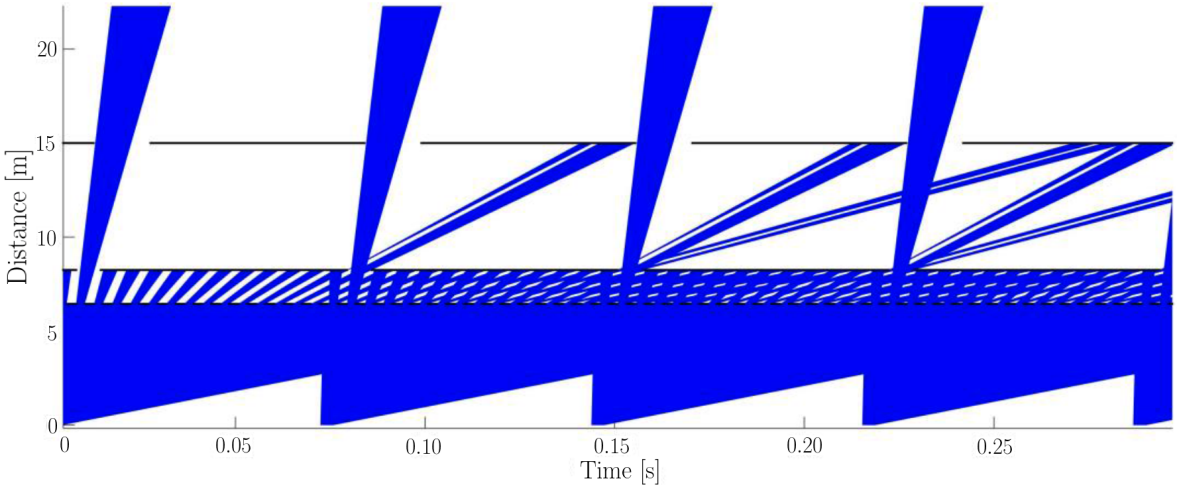

(a)

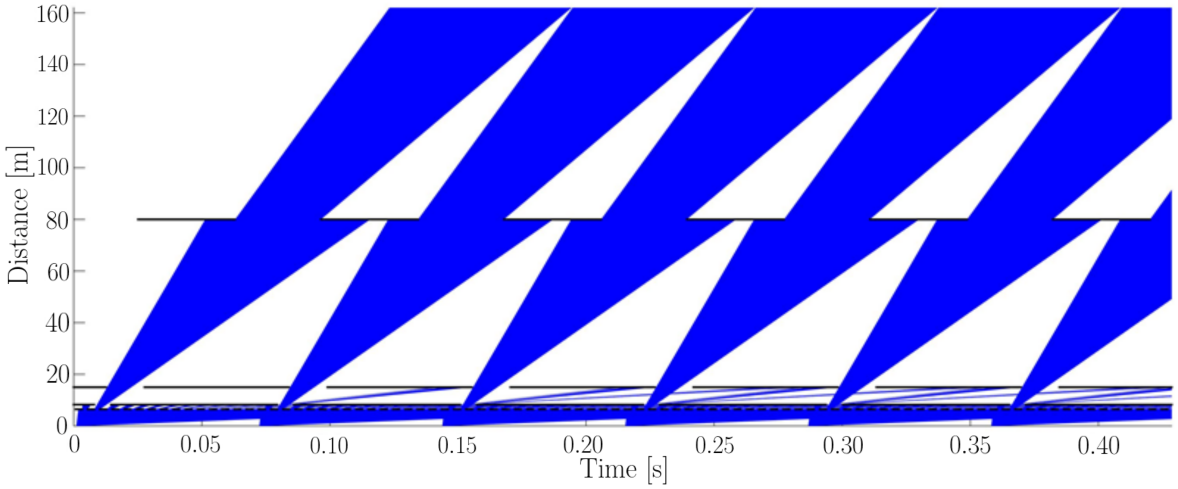

(b)

Figure 1.8: A typical time-distance diagram of BIFROST. (a) the first segment of the instrument including the pulse-shaping chopper and the two frame overlap choppers and (b) the full beamline including the frame overlap chopper too. From [52].

and are separated by absorbant shielding between them to disable neutron transition between the channels, commonly referred to as cross-talk shielding. In each Q-channel, several crystal analyser arcs are placed one behind the other to select different final energies by scattering neutrons vertically (down) towards the corresponding set of position sensitive detectors (see Figure 1.9b). Enabling multi-energy analysis in a single Q-channel by placing the analysers for higher neutron energies behind the ones for lower energies is possible due to the high transparency of the 1 mm thin highly-oriented pyrolytic graphite blades [56]. In each analyser arc 7–9 analyser crystals are located and positioned according to the Rowland geometry [57]. In this focusing geometry the sample, analysers and the detector lie on the Rowland circle, with the reflecting planes for each crystal set toward the centre of the focusing circle, that is also

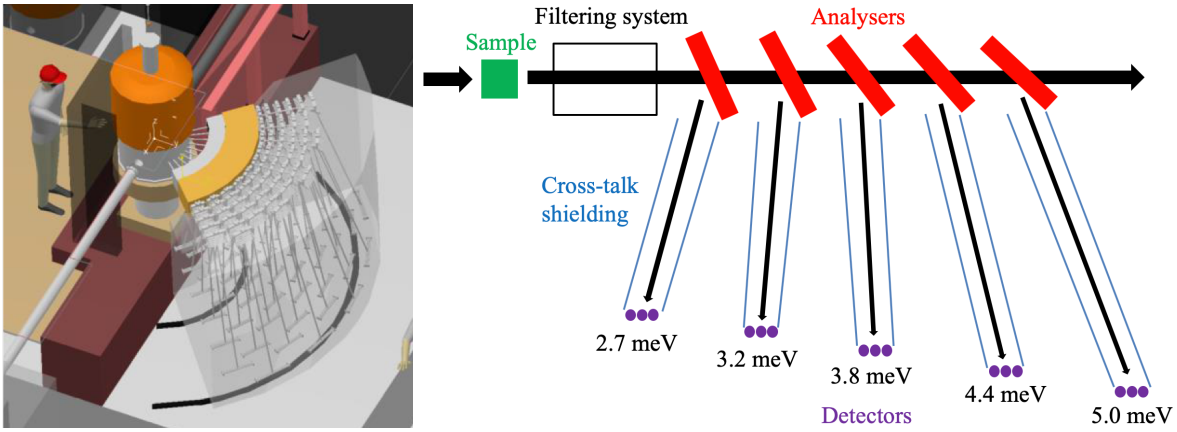

(a) (b)

Figure 1.9: The BIFROST scattering characterisation system. (a) 3D model of the secondary spectrometer tank from [7] and (b) side view sketch of the sample and a single Q-channel with five energy channels in it.

located on circumference of the Rowland circle. In order to ensure that neutrons can reach the detectors only by scattering from the corresponding analyser arcs, further cross-talk shielding is applied, separating the so-called energy channels.

A perfect single-crystals analyser would select only those neutrons which fulfil the Bragg-condition in Equation 1.4 for the chosen scattering planes, that is (h,k,l)=(0,0,2) in case of the pyrolytic graphite.

$$2 \cdot d_{h,k,l} \sin(\theta) = n \cdot \lambda, \tag{1.4}$$

where d_{hkl} is the interplanar distance of the crystal, θ is the scattering angle, n is a positive integer and λ is the wavelength of the incident neutrons. Higher order scattering ($n > 1$) is eliminated by the filtering system, so this would mean that precisely one neutron wavelength is selected. Real analysers, however are not perfect, and have a spread of crystal plane orientations, and therefore accept a range of wavelength centred around that selected by the perfect crystal. The measure of the spread of crystal plane orientations in crystallography is the mosaicity, with the ideal value of zero for a perfect single-crystal. The higher (coarser) the mosaicity, the wider the wavelength range selected by the analyser, as the higher spread of crystal plane orientations enables them to fulfil the Bragg-condition. This is also true for a wider incident angle range, meaning that neutrons of a divergent beam with higher incident angle have the possibility to be Bragg-scattered on the selected scattering plane. The higher spread of crystal plane orientations, on the other hand, lowers the probability of neutrons with energy and incident angle close to the ideal values to be scattered. The cumulative effect

and optimal analyser mosaicity depends on the applications and the incident neutron beam.

The blades to be used at BIFROST have a mosaicity of 60 arcmin to apply the prismatic analyser concept [58], using ^{3}He detector triplets for all five neutron energies chosen for BIFROST (2.7 meV, 3.2 meV, 3.8 meV, 4.4 meV, 5.0 meV) in each Q-channel. According to the prismatic analyser concept, illustrated in Figures 1.10 each of the three detectors of a triplet records a slightly different region of energy, as neutrons with different energies are scattered in slightly different angles, given by the Equation 1.4. Although the Rowland circle is not the same for the different energies, the Rowland geometry is not sensitive to small changes in energy, therefore the outer detectors will be in almost perfect focussing condition even though the analysers are focused on the central detector.

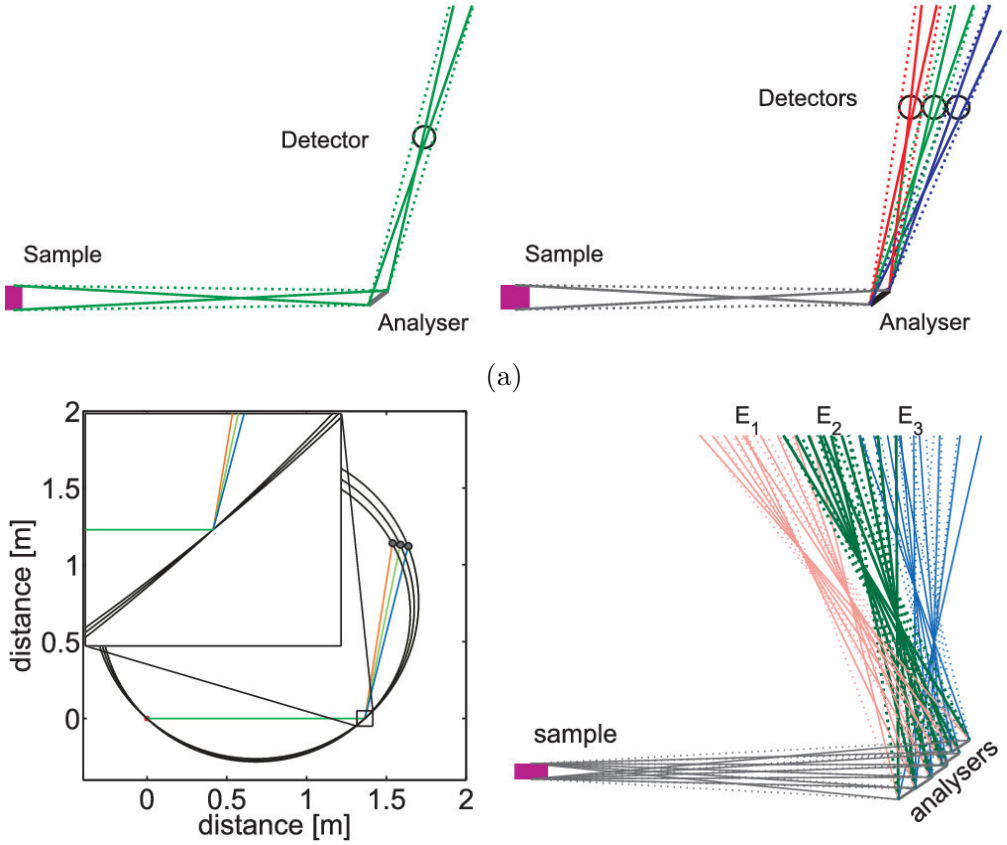

Figure 1.10: Illustration of prismatic analyser concept from [58]. (a) Reflection of a monochromatic beam from a single analyser crystal focussing at a certain distance (on left). Reflection of three specific energies (red, green, blue, respectively) from a single analyser crystal (on right). The solid and dashed lines represent the limits of the scattered rays. (b) Illustration of the optimal Rowland circles for three parallel detector tubes (on left). The principle shown for five analysers arranged in a Rowland geometry, the three energies, represented by different colors, are separated at the focussing distance (on right).

In order to provide enough space for the detector tubes, the analysers and corresponding detectors in adjacent Q-channels are slightly shifted radially. The sample–analyser distances are increased or decreased by 4.6–7.5% in two out of three Q-channels, however the analyser-detector distances are kept unchanged to keep the detectors of same energy on the same vertical planes and by that keeping the spectrometer tank geometry simple. As a result, the sample–analyser distance is shorter or longer than the analyser–detector distance in two out of three Q-channels, showing a slight asymmetry to the Rowland-geometry. The three different types of Q-channels are repeated three times, giving the nine Q-channels a "triple stagger" geometry.

The final neutron energy for each detector triplet is fixed by the corresponding analysers. Knowing the final energy, the incident neutron energy is calculated from the ToF of the neutron, and the distance travelled by it. The path length of a neutron is calculated with respect to its detection point given by the position sensitive ^{3}He detector tubes. The 9 Q-channels each cover a scattering angle range of 5.2°. To cover a continuous 90° scattering angle range, two tank settings has to be used. Within each Q-channel, the detectors are positioned perpendicularly to the neutron path, therefore the scattering angle of each neutron is also given by the position of the detection point along the detectors, of course, with respect to the rotation of whole detector tank and relevant Q-channel in particular.

Position sensitive ^{3}He tubes are the "gold standard" for neutron detection [59]. They are however quite rate limited. Non-position sensitive tubes saturate at 100 kHz; however for position sensitive ^{3}He tubes, operation at instantaneous rate above 30 kHz can be problematic. The exact rate capability of a detector is dependent on the details of readout electronics, that is usually the bottleneck in this aspect. It is therefore essential to evaluate the rates anticipated for high-flux instruments such as BIFROST, in order to extract the respective detector requirements.

Chapter 2

Simulation tools and methods

Monte Carlo simulation [60] plays a key role in the development and characterisation of instruments as a reliable, cheap and versatile tool [61], as CPU cycles are cheaper than prototyping cascade for complicated scientific instrumentation. Feedback from simulations taken into account in the development of the instrument design can reduce the number of physical prototypes needed, and also enable the quantification of otherwise unmeasurable properties. Development of complete and detailed instrument simulation models enables simulations from source to detectors, offering the opportunity to discover and decouple otherwise undetectable cumulative effects. These models can provide valuable input for developing calibration and correction routines for data reduction and analysis, and could later be used for experiment planning by users, to predict experimental conditions from specific proposed samples, i.e. sample size and composition.

The simulation of a complex system such as a neutron scattering instrument is not straightforward and is subject of certain limitations. At the moment, there is no single software that enables detailed and efficient simulation of all aspects like production of neutrons, their transport for long distances through neutron guides, transport in crystalline materials, and detection via production of secondary particles. There are, however a handful of simulation tools with different strengths and weaknesses. Recent developments enabled interchange of particle data between some of these tools, making it possible to use a chain of simulations to carry out the full simulation of a neutron scattering instrument using the adequate software at each part of the system. Such simulation of full instruments is a novel method that has been applied only in a handful of cases. Two out of the first three published cases are presented in this thesis [62–64].

In this chapter the simulation tools and methods used throughout the thesis are introduced, as well as the pre-existing simulation models of the LoKI and BIFROST instruments. In the first two sections the two main particle transport codes used are introduced, namely McStas and Geant4, then an additional tool, NCrystal is presented,

that enhances their capabilities of the correct treatment of neutron transport in typical components of neutron instruments. After that, MCPL is introduced, the file format and associated tools that facilitates the transition between simulation software. That is followed by the introduction of the simulation schemas and methods of how the full simulation of instruments is carried out by connection of tools. Finally, in the last section the rate definitions used throughout the thesis are presented.

2.1 McStas - A neutron ray-trace simulation package

McStas [65, 66] is a simple and user friendly cross-platform, open source Monte Carlo tool dedicated for simulation of neutron scattering instruments and experiments, that is broadly used for instrument design. It can model all major components of an instrument by sampling an external neutron source distribution and then propagating neutrons through guides, choppers, monochromators, collimators etc. until the sample and beyond. A collection of sample components is also available allowing the neutrons to scatter based on underlying physics models and then be histogrammed by monitor components that act like "detectors". The latter process is of particular interest for the detector design, as it allows the visualisation of the neutrons entering the detector geometry accessing at the same time their full list of properties, e.g. wavelength (λ), time-of-flight (ToF), position, scattering angle (θ) and optionally user-defined flags. These properties are necessary to differentially study the picture of the impinging neutrons on the detector as a function of time (within a neutron pulse), wavelength and polar angle.

McStas uses a ray-tracing algorithm which enables fast neutron transport simulations over long distances and through many components, that is necessary for long instruments like BIFROST, but it has important downsides. In a McStas instrument definition file, the geometrical components like the source, guide sections, choppers, slits and the sample are placed one after the other. McStas by default propagates neutrons from component to component in the exact order as they appear in this file. All neutrons that miss or do not interact with the component downstream are removed from further simulation. This process makes the simulation of long instruments really fast, but on the other hand restricts the neutrons to follow one exact path.

It is possible to change this behaviour by grouping components together, as described in the users and programmers guide [67]. This way it is possible to some extent to split the beam, by having a group of components as the potential next target of neu-

trons, but after the interaction with strictly one of the group members, McStas tries to propagate all neutrons to the same component that appears next in the instrument file. This is suitable for simulations where a set of analysers scatter neutrons to a sample or to a single detector, but does not allow the simulation of multiple Q-channels in the detector bank of the BIFROST instrument simultaneously. If a user wants to split the beam and allow propagation in multiple directions through different components, consecutive groups must be implemented, all of which include the subsequent component in each direction. Extensive use of such grouping makes the instrument file immensely complex and still prohibits multiple interactions within one group, or back and forth propagation between groups of components.

The process of ending simulation of neutrons that miss or do not interact with a component or group of components disables proper treatment of transmission, that is vital in case of BIFROST where multiple set of analysers are placed behind each other in a Q-channel. In order to allow neutrons to proceed without interaction e.g. with a set of analyser blades, an extra virtual component can be added to each group, that mimics an interaction without changing the neutron state, and thereby prevents neutrons to be removed from the simulation.

Even with grouped and virtual components, neutrons still have to follow the order of components or groups of them in the instrument definition file, so back-scattering or multiple scattering among components of the same group is still not possible in the simulations.

Both the LoKI and BIFROST instruments are modelled in McStas as part of the design progression. In the next subsections these models are introduced briefly and demonstrated using the visualisation tool of McStas.

2.1.1 The LoKI instrument model

The baseline McStas model of LoKI [68] is depicted in Figure 2.1. In this work it is used for the study of the detector rates for the SANS instruments at ESS. It is assumed that no major modifications are anticipated or that future modifications will not impact the predicted rates in a way that completely resets the detector design effort.

The model includes the official McStas component of the ESS butterfly moderator source ("ESS_butterfly") [13, 69], that is based on functional fits to the underlying data from MCNP simulations of the moderator. It is claimed that the spatial variation of the brightness across the moderator face should be considered to have an uncertainty of the order of 10%. The accelerator power is an input parameter for this component and it is treated as a linear scaling factor for the source intensity.

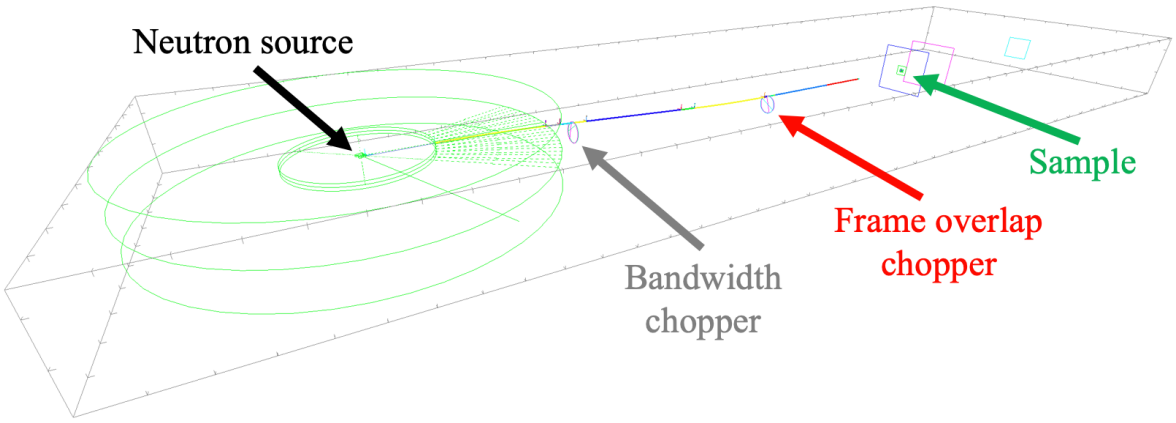

Figure 2.1: McStas model of the LoKI instrument beam transport and conditioning system.

The model also includes the bender pair, the bandwidth and the frame overlap chopper pairs, the four slits, all guide sections and the sample. The parameters of these components enable simulations with various instrument configurations. Neither the sample environment nor realistic detector arrays are modelled, only the rear detector panel is included as simple monitor components.

2.1.2 The BIFROST instrument model

The McStas model of the BIFROST instrument [70] is depicted in Figure 2.2.

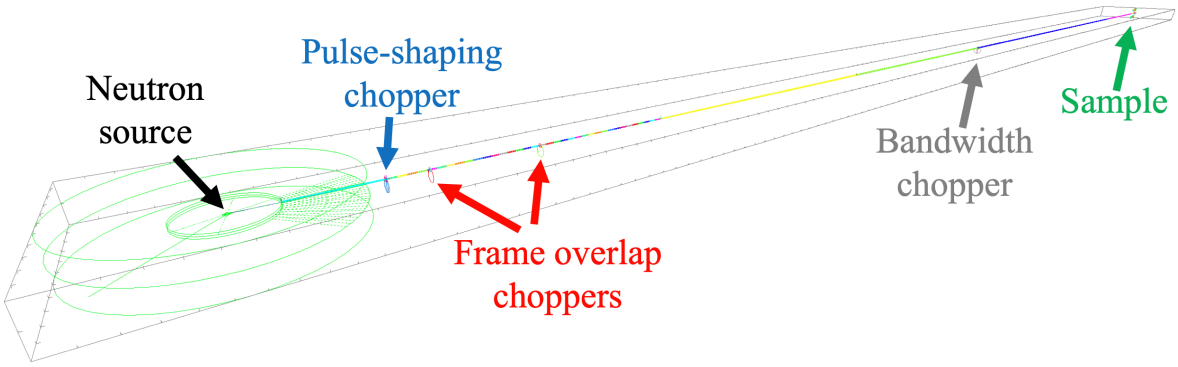

Figure 2.2: McStas model of the BIFROST instrument beam transport and conditioning system.

The source of neutrons is the same ESS butterfly moderator source as for the LoKI instrument model, and the expected rates for BIFROST will also scale linearly with source power for constant proton energy. The model contains the pulse-shaping chopper, two frame overlap choppers, the bandwidth chopper, the slits, all guide sections, the sample and several McStas monitor components to characterise the beam at multiple locations along the guide. Neither the sample environment nor the scattering characterisation system is included in the base instrument model.

2.2 Geant4 - Detailed detector simulation

Geant4 [71–73] is a general purpose Monte Carlo particle transport toolkit developed at CERN with applications in many fields, e.g. high energy physics, nuclear physics, accelerators and medical physics. Its usability for simulation of neutron detectors has been greatly improved by the ESS Detector Group by building a framework [61, 74] around it, which adds several functionalities and integrates NCrystal and MCPL, both of which are described in details in the upcoming Sections 2.3 and 2.4.

Currently Geant4 is not capable of simulating neutron transport through long neutron guides as McStas is. It is, on the other hand, much better suited for simulation of complex geometries and neutron detectors. The definition of the simulated geometry in composed of un-ordered nested volumes filled with different materials. This means that there is no strict order of the geometrical components and particles can naturally scatter back and forth among them any times. This gives the possibility to simulate geometries with high level of complexity, like the scattering characterisation system of BIFROST where 369 analyser blades are arranged in 9 Q-channels and 5 energy-channels in each. It also gives the option to analyse effects of cross-talk on signals and to evaluate shielding strategies.

Another big advantage of Geant4 is that it is capable of simulating practically any kind of particles, not just neutrons. The unit of simulation is a so-called event which not only contains the track of the launched primary particle but also the track of produced secondary and any further particles. This is ideal for the simulation of detection process in neutron detectors. With these simulation events it is possible to calculate the energy deposited in the counting gas of a ^{3}He tube by the proton and tritium produced in the neutron capture of ^{3}He. The same can be done for detectors with solid boron converter layer, where either or both the alpha and lithium particles – productions of the neutron capture of ^{10}B – have to escape the converter layer to deposit energy in the counting gas. This gives the possibility to define detection events with certain energy threshold to model detection in real measurements where such threshold is always necessary to eliminate gamma background. This way it is possible to separate neutrons which trigger detection event from those which get converted but the their conversion products do not deposit enough energy to the counting gas to overcome the threshold.

Using the aforementioned ESS Detector Group framework, the process of simulation and data analysis can be separated. The simulations can result in so called Geant4 Results in Friendly Format (GRIFF) files containing trajectories and properties of all

particles (all simulation events). These files can then be processed by self-defined analysis where all information of the simulated events can be accessed. This process makes the simulation slower, but the analysis can be changed and the results can be re-evaluated without the need to re-run the simulations. That is not the case for McStas where the simulation has to be repeated if a monitor component is missing, or the resolution of one is not fine enough.

At the analysis level filters and custom conditions can be applied to efficiently select events that are of interest. Multiple definitions of efficiency can be used for complex detector systems simultaneously and absorption can be observed in all materials separately. Knowing all information about the past of a neutron that trigger detection events makes it possible to study how certain parameters of neutrons are changed due to scattering in materials of the detector, and how does this affect measurable quantities. The ability to study and decouple such effects that are otherwise unmeasurable and doing it without the need to build prototypes is a powerful tool in characterisation of detectors and detector systems.

2.3 NCrystal - Simulation of neutron interactions in crystalline materials

NCrystal [61, 75] is a novel open source software package for modeling thermal neutron transport in crystalline materials. It consists of a data library and associated tools which enables calculations for Monte Carlo simulations. It can be used together with McStas and Geant4, to enhance their capabilities of the correct treatment of neutron transport in typical components of neutron instruments, including beam filters, monochromators, analysers, samples and detectors. Physics modelled by NCrystal includes both coherent elastic (Bragg diffraction) and incoherent or inelastic (phonon) scattering. It treats all valid Bragg diffractions on each reflection plane explicitly and is able to use various models for inelastic scattering on phonons. Its data library already contains the most popular crystals and the results are validated against the EXFOR database and existing crystallographic software.

NCrystal focuses initially on scattering in single-crystals or polycrystalline materials and powders. Most single crystalline materials are appropriately modelled with crystallites orientated around some reference orientation with a Gaussian distribution that has a standard deviation of the mosaicity of the crystal. There are, however, single crystalline materials with crystallite distributions so different from Gaussian that this approximation does not hold. One of these materials is pyrolytic graphite, that

is widely used as a monochromator and analyser in neutron instruments. This is precisely the case for BIFROST, where 369 highly-oriented pyrolytic graphite analyser blades are used altogether in the nine Q-channels. Graphite has a layered structure, made up of graphene sheets in which carbon atoms are arranged in a hexagonal lattice. In highly-oriented pyrolytic graphite the crystallite axes orthogonal to the graphene sheets are distributed along a preferred direction, suitable for description with a Gaussian mosaicity distribution, but the orientation around this axis is completely random, resulting in powder-like features in neutron scattering. Recent developments enabled NCrystal to handle materials with this kind of structure by using a specialised model for layered crystals.

Demonstrating some of the NCrystal pyrolytic graphite properties, the components of total cross-sections and a distribution of randomly sampled scatter angles are depicted in Figure 2.3 for powder sample, not the layered crystal distribution.

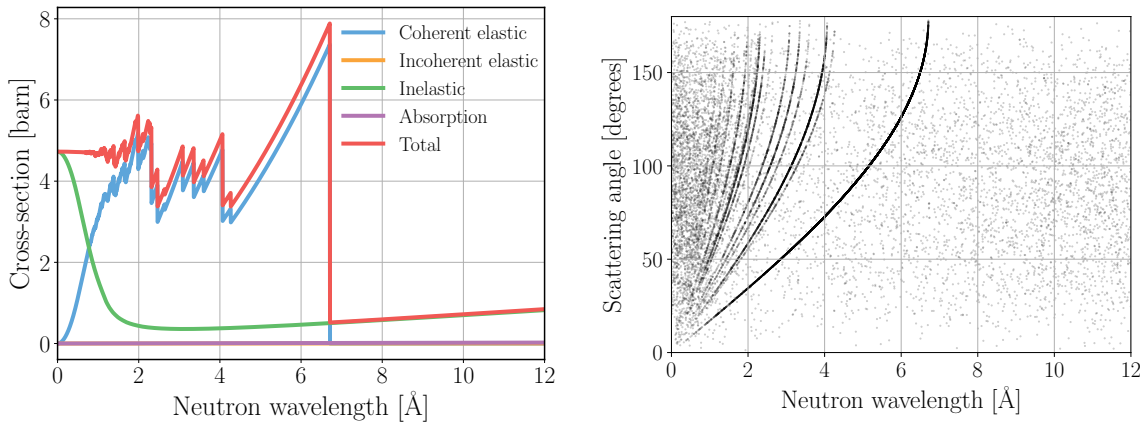

Figure 2.3: Components of the total interaction cross-section (left) and two-dimensional scatter-plot (right) for NCrystal pyrolytic graphite powder.

Up until the latest version (v1.0.0), NCrystal treats absorption with the simple model of absorption cross-sections being inversely proportional to the neutron velocity. The absorption cross-section for a particular neutron velocity is calculated by scaling the value given at the reference velocity of 2200 m/s. This applies for NCrystal materials used in McStas simulations, but not for those in Geant4 simulations. Geant4 models secondary particles produced in absorption, therefore the NCrystal plugin does not interfere with the Geant4 absorption physics at all. As an example, the minor differences in absorption cross-section for pyrolytic graphite is shown in Figure 2.4.

Using NCrystal in McStas and in Geant4 within the ESS Detector Group Framework is rather straightforward. In the former the “NCrystal sample” McStas component has to be used, while in the latter the material of a certain volume has to be

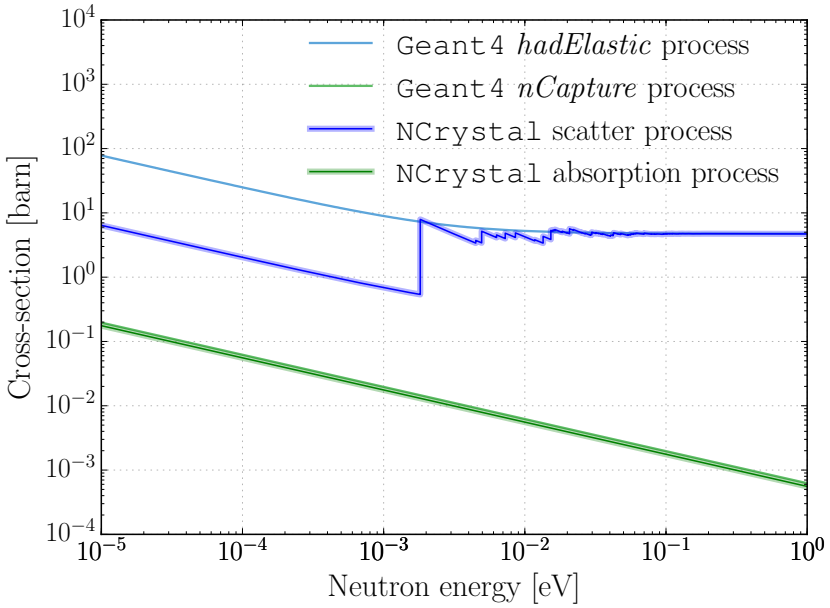

Figure 2.4: Comparison of neutron interaction cross-sections of pyrolytic graphite powder in Geant4 and NCrystal. Lines are barely distinguishable for Geant4 neutron capture and NCrystal absorption cross-sections, the former being higher in the whole energy range depicted.

defined as an NCrystal material. In both cases a uniform material configuration syntax can be used to define parameters like temperature or mosaicity and orientations in case of single crystals. An example is presented below.

```
C_sg194_pyrolytic_graphite.ncmat;temp=293.15;mos=60arcmin;
dir1=@crys_hkl:0,0,2@lab:0,1,0;dir2=@crys_hkl:0,2,0@lab:0,0,1;
```

In this example the aforementioned pyrolytic graphite material is chosen – by the name of a crystallographic data-file as the first parameter – with the temperature of 293.15 K and a mosaicity of 60 arcmin. The orientation of the crystal is not dependent of the physical shape of the component or volume. In the example it is given by specifying that the normal of the (h,k,l)=(0,0,2) plane should point along the y-axis in the laboratory system, and the normal of the (h,k,l)=(0,2,0) plane should point along the z-axis.

2.4 MCPL - Exchanging data between simulation tools

Monte Carlo Particle List (MCPL) [76, 77] is a binary file format dedicated for storage and interchange of particles between various Monte Carlo simulation applications, like McStas, Geant4, McXtrace [78], PHITS [79] and MCNP [80]. An MCPL file can

contain a list of particles – not just neutrons – and every necessary information about them, which makes it suitable for input and output format for simulation tools which have the appropriate plugins or converters.

The MCPL code distribution includes a command-line tool to access and manipulate files (e.g. merging files or extract information from them), and programming interfaces for C/C++ and python so that users can implement plugins and converters for further applications.

From McStas MCPL can be used by adding "MCPL_input" or "MCPL_output" components at relevant points in the instrument file. In Geant4 using the ESS Detector Group Framework the same can be achieved with the particle generator from the "G4MCPLPlugins.MCPLGen" module and the "–mcpl" user flag defining output of simulations.

2.5 Connecting tools

As mentioned in the introduction of this chapter, there is no single software that can be used to simulate a neutron scattering instrument from the beginning all the way to the end. Still, one of the aims of this work is to carry out such end to end simulations. The way around the problem is to connect tools and do a chain of simulations, using each of them where they are the most capable.

The simulation the of instruments in this work begins with the aforementioned ESS butterfly moderator source ("ESS_butterfly") McStas component, that relies on the MCNPX calculations of the ESS moderator performance [12, 13]. A full simulation chain could technically include earlier processes leading to the production of neutrons, starting with the ion source and the proton accelerator. Simulation of these processes are done [81], however they are independent of the instruments themselves, and all relevant information are incorporated in the neutron moderator spectrum given by the MCNPX calculations.

For the simulations of the beam transport and conditioning system, the McStas model of LoKI and BIFROST – introduced in Sections 2.1.1 and 2.1.2 – are used. In case of BIFROST the simulation of neutron transport ends at the end of the last guide section, but for LoKI the McStas simulation also includes the scattering on the sample. In both cases an "MCPL_output" component is added to the end of the instrument file to export neutron data in MCPL format.

These MCPL files are then used as neutron sources for the subsequent Geant4 simulation of the scattering characterisation system of both instruments. For LoKI

this means the simulation of the detection process in the rear detector bank, that consist of 5 overlapping layers of BCS detector tubes. For BIFROST the simulation arrangement includes the sample and all 9 Q-channels of the detector tank. In the latter case, however the focus is on the incident detector rates so the simulation of the detectors and the detection process is out of the scope. On the other hand, a McStas model of a reduced BIFROST geometry containing the sample and a single Q-channel is also implemented to allow comparison of the two simulations software. The schematic figures of the simulation scheme for both instruments are depicted in Figure 2.5.

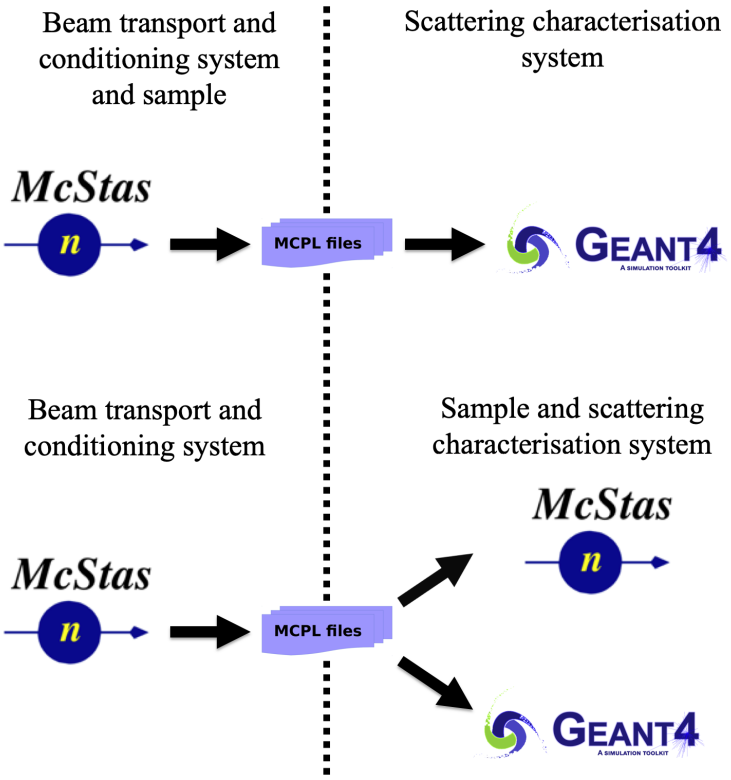

Figure 2.5: Outline of simulation scheme for the LoKI (at top) and BIFROST (at bottom) instruments.

For the simulation of neutron transport in crystalline materials, NCrystal is used in both McStas and Geant4. The simulation models implemented for the scattering characterisation systems are introduced in details in the following chapters.

For the sake of completeness, it worth mentioning that in the current work the simulated detection process in Geant4 does not include the charge collection in the detectors. Complete simulation of gaseous detectors, including spatial charge effects can be carried out by interfacing Geant4 with other simulation tools like Garfield++ and Degrad, as demonstrated in [82, 83], however it is out of scope for this thesis.

Another possibility to extend the scope would be the connection of the simulations

to the Mantid [84] software, that is used for reduction and analysis of measured data. This connection could facilitate implementation of corrections and calibration routines. In fact, for the LoKI instrument this work has already been started spawned from the results presented here, and will be mentioned in Section 9.1.

All results of simulations have systematic and statistical uncertainties. Unlike systematic uncertainties which are present mainly due to imperfect modeling of the system and inherent biases in this model, statistical uncertainties can be reduced by increasing the number of simulated particles. Throughout this work where the uncertainty is not significant, it is not indicated. Sources of systematic uncertainties, like the effect of the parts of the instruments not included in the simulations models are considered and not expected to change the conclusions.

2.6 Rate definitions

With the combination of the McStas and Geant4 it is possible on one hand to take into account the correlations of neutron properties, like ToF, energy, spatial and momentum vectors, and on the other hand to reliably evaluate the detector performance. Although the simulation of each neutron is independent, by handling the ToF information it is possible to define the instantaneous rates as well as the time-averaged ones.

At a pulsed source the highest instantaneous (peak) rate could be more than an order of magnitude higher than the time-averaged one. It is thus important for the qualification of a detector technology for a specific application and impacts the readout electronics design. The peak rates also dictate the system design for data collection, aggregation and transfer but as the data are propagated further down the process chain, it is the time-averaged rates that become more relevant for data transfer and storage choices.

Another distinction in the current work is between incident and detection rate. The first would be the upper limit the detector would count, if it had a detection efficiency of 100%. As the detectors have efficiencies that depend on the neutron energy, the moment when the number of incident neutrons is highest is not necessarily the moment of the highest number of detected neutrons. A detector might be illuminated with a high flux but if it is not efficient at the respective neutron wavelengths, there is no concern for saturation. The peak incident rate and peak detection rate do not have to occur simultaneously.

The incident neutrons arrive at the detector with various ToF and energy values. As Geant4 continues to count time for the particles it propagates, the ToF distribution

will vary as a function of detector depth. This effect needs to be taken into account for the estimate of the instantaneous peak detection rates for those detectors that record depth information [10, 26, 85, 86].

The rate definitions used in this work are listed in [87] (page 14) as follows:

- **Global time-averaged incident/detection rate**: the total number of neutrons per second entering/recorded by the entire detector.
- **Local time-averaged incident/detection rate**: the total number of neutrons per second entering/recorded in a detector pixel, channel or unit.
- **Global peak incident/detection rate**: the highest instantaneous neutron incident/detection rate on the whole detector.
- **Local peak incident/detection rate**: the highest instantaneous neutron incident/detection rate on the brightest detector pixel, channel or unit.

Chapter 3

Detector rates for LoKI instrument

In order to design detectors with the appropriate rate capability and prevent performance compromises on this front, a detailed analysis of the instrument requirements and how they translate to detector requirements is vital. The work introduced in this chapter aims at acquiring a good understanding of the rates LoKI is going to achieve by looking at how the scattered neutrons on the sample are distributed in space and time. A realistic worst-case scenario is reproduced, based on which the detector requirements for rate capability are extracted. The main focus of this evaluation concerns the neutron scattering taking place within the forward solid angle after the sample, as this happens to be the primary area of interest for the SANS technique. This translates to a typical 1 m $\times$ 1 m detector area considered for the rate estimates of the scattering characterisation system.

In order to define the highest incident and detection rates, a Geant4 simulation model of the rear detector bank is developed. To generate neutrons for the simulations, the McStas model of the LoKI instrument introduced in Section 2.1.1 is used in case of three different instrument configurations. At the end of the McStas (v. 2.4.1) simulation of the neutron transport from the ESS source until after the scattering on the sample, the neutron data is saved in MCPL format. These MCPL files then serve as source for the Geant4 simulation of the neutron transport in the detector bank, including conversion and detection in the detectors.

In the following sections the instrument and sample settings used for the McStas simulations are presented, then the developed Geant4 simulation model of the detector bank is introduced, and finally the acquired incident and detected rates are demonstrated.

3.1 Instrument configurations

The chopper settings, collimation length and aperture sizes of a SANS instrument are experimentally configured depending on the sample and the type of measurement to be performed. For the rate estimates a few configurations are selected, aiming at maximising the neutron flux on the sample, in combination with a sample that strongly scatters within the forward solid angle. The accelerator power of the ESS butterfly moderator source component mentioned in Section 2.1.1 is set to 5 MW, so the deduced rates correspond to the maximum source power.

The instrument and sample settings used for the rate estimates are listed in Table 3.1. The chopper settings are reflected in the wavelength range, i.e. the λ_{min} and λ_{max} values allowed to reach the sample from the source. The same sample model is used for all instrument configurations. It is a diblock copolymer with a 4.84% scattering probability, an adequate choice for the study of the rear detector geometry. The sample size of 1 cm × 1 cm matches that of the sample aperture. In SANS it is typical

Config	Collimation length [m]	λ_{min} [Å]	λ_{max} [Å]	Source aperture [cm×cm]	Sample aperture [cm×cm]	Flux on sample [n/cm^2/s]	Beam spot size [cm]
1	3	3.0	11.5	3 × 3	1 × 1	1.00×10^9	8.4
2	5	3.0	11.5	2 × 2	1 × 1	2.02×10^8	4.4
3	8	3.0	10.0	2 × 2	1 × 1	8.24×10^7	3.0

Table 3.1: LoKI instrument configurations for the evaluation of rates. The same sample is used for all scenarios. The beam spot size represents the direct beam size on the detector and is defined by the collimation settings.

to match the collimation length to the sample–detector distance, in order to optimise the resolution capability of the instrument. For the current study though, this distance is fixed at 5 m, that is the closest position of the rear detector for the instrument, in order to maximise the rates.

The contributions to the number of neutrons reaching the detector can be broken down to the coherent and incoherent scattering components from the sample, the incoherent scattering from the solvent and the transmitted neutrons, as in Equation 3.1.

$$N = coh_{sample} + incoh_{sample} + incoh_{solvent} + transmission. \tag{3.1}$$

In the current study, only the coherent scattering from the sample is taken into account,

i.e. the actual signal the SANS technique is after. This provides a lower limit to the rate estimates for the scattering characterisation system.

Knowing the scattering fraction F(%) for a SANS sample model, it is possible to get an approximate analytical estimate for the time-averaged incident rates the rear detector is exposed to. The largest portion of the signal-related scattered neutrons is contained within the forward cone subtended by the rear detector, which usually has a polar angle coverage of up to a few degrees, depending on its distance from the sample. The diblock copolymer model mentioned before has a scattering fraction of about 4.8%. For instrument configuration 1 this translates to an upper limit of a global incident time-averaged signal rate of 4.8% $\times$ 10^9n/s/cm^2 flux $\times$ 1 cm^2 sample size = 4.8 $\times$ 10^7 n/s = 48 MHz. The incoherent contribution from the sample and the solvent have to be estimated in addition. If 10% of the incident beam is incoherently scattered in 4π, then the incident fraction within the solid angle subtended by the rear detector is 10% $\times$ 10^9n/s/cm^2 flux $\times$ 1 cm^2 sample size $\times$ 0.04 sr = 4 MHz. A global time-averaged rate of 52 MHz is to be expected as an upper incident rate limit for the high flux instrument configuration on the rear detector.

The resulting incident neutron ToF and wavelength distribution on a standard 1 m $\times$ 1 m area at 5 m after the sample is depicted in Figure 3.1 for all three configurations. For determining time-averaged and instantaneous rates it is always important to take into consideration the pulse structure of the ESS neutron beam with its 14 Hz repetition rate.

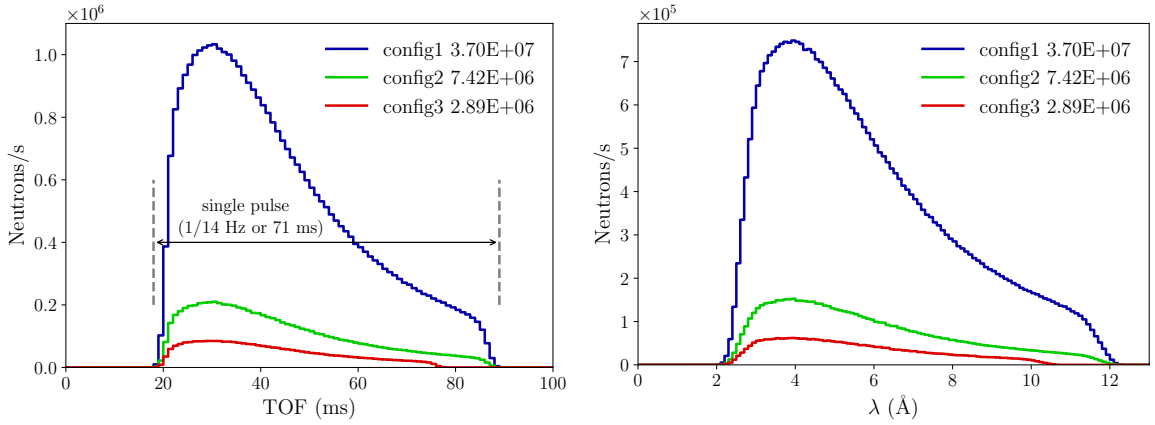

Figure 3.1: A typical neutron ToF and wavelength distribution 5 m after the sample for the three instrument configurations. The global incident rates per configuration appear in the legend in Hz for a standard 1 m $\times$ 1 m detector.

3.2 Geant4 model of the rear detector bank

The Geant4 geometry model implemented for this study is a generic 1 m × 1 m detector arrangement that consists of 5 consecutive detector panels with 40 tubes in each (see Figure 3.2). For higher uniformity in the conversion efficiency, the tubes are rotated by 20° around their cylindrical axes and a relative horizontal shift of 10.16 mm is applied for adjacent panels (see Figure 3.3) to avoid high differences in the path length in the B_4C converter layer [88].

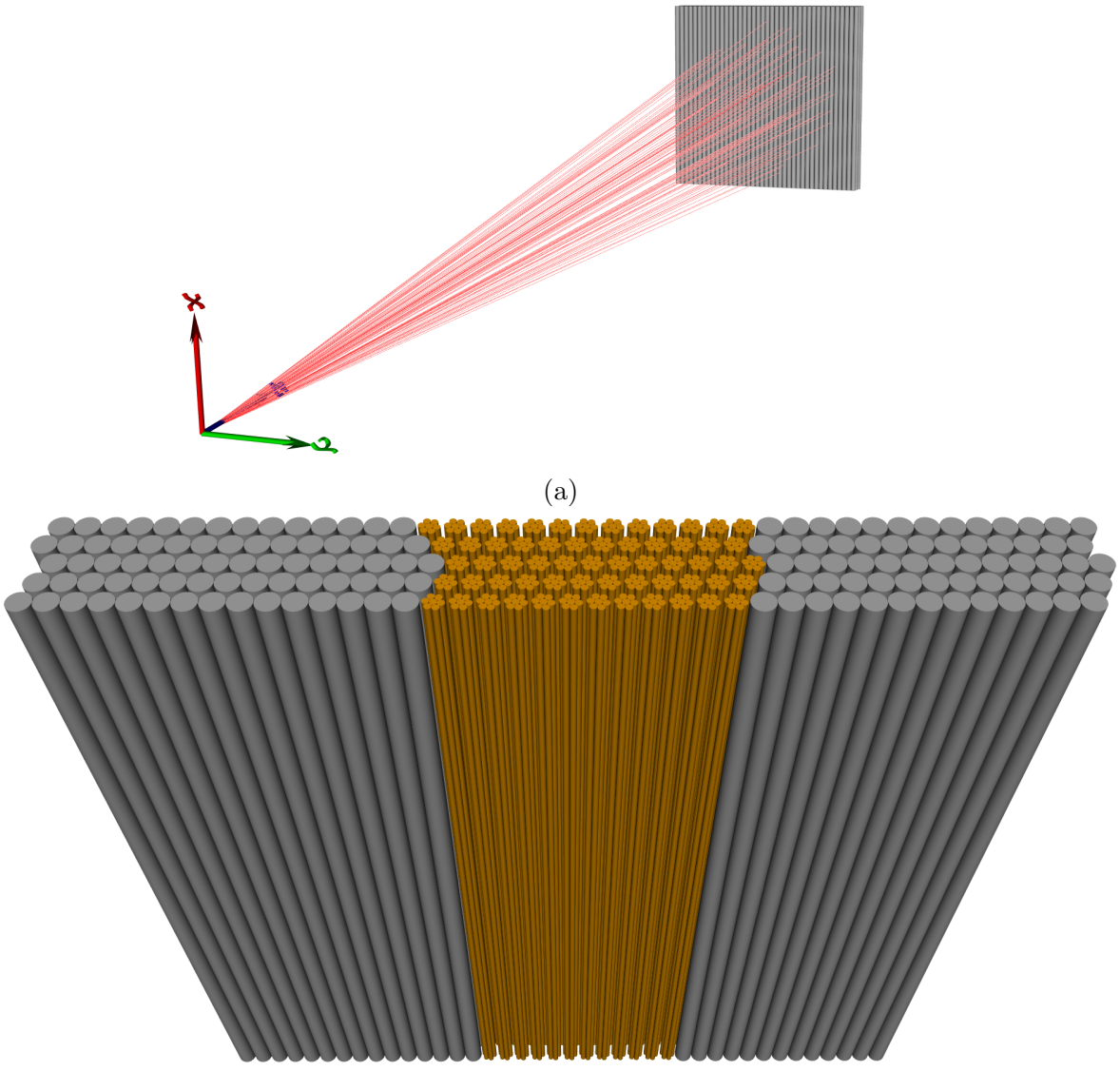

(a)

(b)

Figure 3.2: The simulation arrangement containing the neutron generator at the origin of the coordinate system and 5 panels (× 40 tubes/panel) of BCS tubes covering 1 m × 1 m. (a) the primary neutrons (in red) hit the detectors 5 m away from the source (sample) position and (b) enlarged view of the 5 consecutive BCS tube panels with straws exposed in the middle section for illustration. Each aluminium tube (grey) contains 7 copper straws (orange) arranged hexagonally.

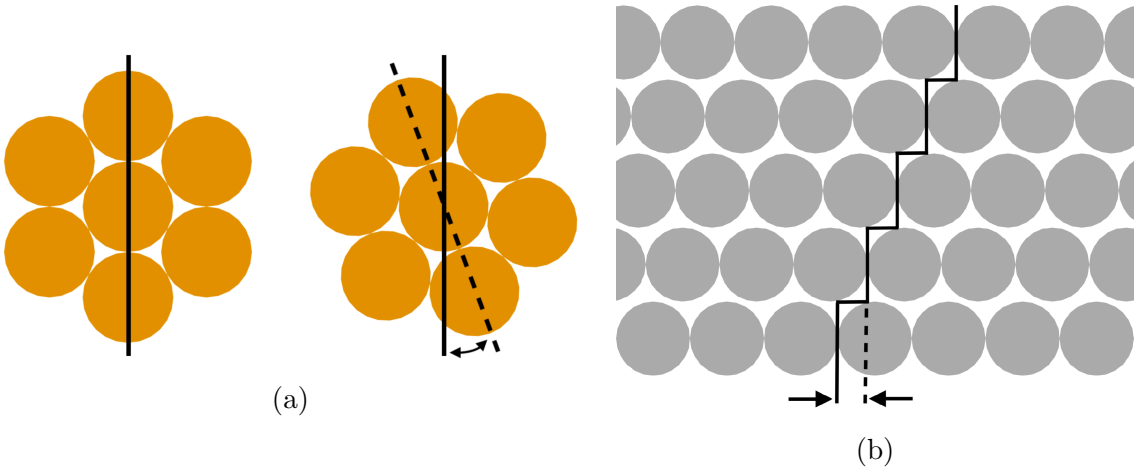

Figure 3.3: Rotation and translation of the detector tubes in order to increase the uniformity of the conversion efficiency for neutron entering the detector arrangement in different positions and angles. (a) a rotation of 20° around its cylindrical axis is applied for every detector tube and (b) a horizontal shift of 10.16 mm is used for adjacent panels.

The model of a single BCS detector consists of the aluminium tube that contains the 7 copper straws arranged hexagonally with 1 μm enriched B_4C layers on their inner surface. The void inside a tube is filled with the Ar/CO_2 mixture (90/10 by volume) at 0.7 atm. The exact parameters of the full scale model are listed in Table 3.2.

Tube diameter	25.4	[mm]
Tube thickness	0.94	[mm]
Straw diameter	7.5	[mm]
Straw thickness	25	[μm]
B_4C thickness	1	[μm]
Tube&straw length	1	[m]

Table 3.2: Geometry parameters in the model of the BCS detectors.

All materials are selected from the Geant4 database of NIST materials, except for Al and Cu. The latter are described with the use of the NCrystal library, as their crystalline structure is important for the correct treatment of their interaction with neutrons. The density of the NCrystal aluminium and copper are ρ_{Al}=2.70 g/cm^3 and ρ_{Cu}=8.93 g/cm^3 respectively. The Geant4 physics list used is QGSP_BIC_HP.

The model does not contain the anode wires in the straws and therefore neither the charge collection nor the readout are simulated. A detection event is recorded if the conversion products of a neutron deposit more energy in the counting gas than a preset threshold applied to mimic discrimination of the gamma background. In different studies of BCS detectors, different thresholds are reported, e.g. 30 keV [89], 73 keV [10]

and 200 keV [45]. Based on these values, in the simulations of this study an energy threshold of 120 keV is applied, which corresponds to an appropriate threshold for ^{10}B detectors to achieve sufficient γ/thermal neutron discrimination for neutron scattering applications [90–92]. The simulation of each neutron is completely independent so pile-up is not possible.

Due to the complex geometry three different definitions of incident neutrons are used in this section: incident for the entire detector; incident for a panel; and incident for a straw. A neutron is counted as incident for the entire detector only once, when it enters the wall material of a tube for the first time. On the contrary, a neutron can be counted more than once as incident for a panel but only if it is scattered back from another panel and enters a tube in the panel of interest again. Moreover, a neutron is counted as incident for a straw every time when it enters its copper layer from the outside.

3.3 Incident and detection rates

For instrument configuration 1 the incident neutron ToF and λ spectra per detector panel are depicted in Figure 3.4. This approach is important for detectors, which provide depth information, as every detector layer is exposed to a different neutron distribution, due to the hardening of the neutron spectrum, caused by the higher absorption cross-section of neutrons with higher wavelength and the thermalisation of the neutrons via scattering. This effect is clearly visible in the incident spectrum, and impacts the energy spectrum of the detected neutrons (see Figure 3.5a).

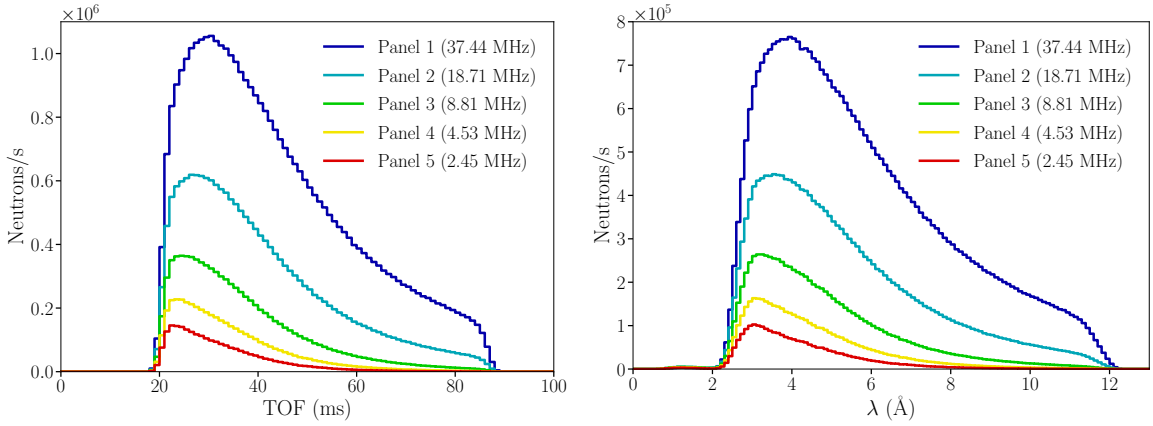

(a) (b)

Figure 3.4: Incident ToF (a) and λ (b) distributions per panel in depth for instrument configuration 1. The respective incident rates appear in the legends.

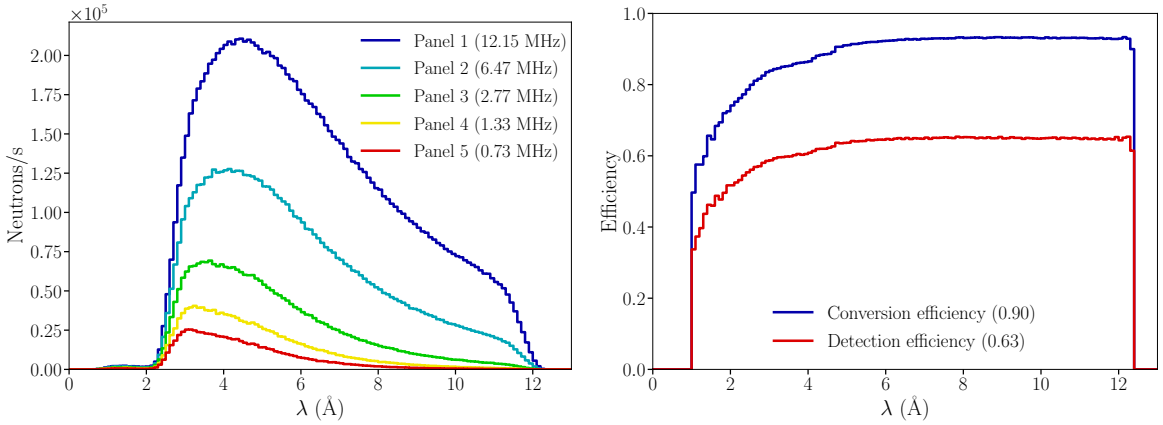

(a) (b)

Figure 3.5: (a) λ distribution of detected neutrons per panel. (b) λ dependent neutron conversion and detection efficiency for the entire detector and for instrument configuration 1. The conversion/detection efficiency is the ratio of the total number of converted/detected neutrons in all straws over the number of incident neutrons for the entire detector for a particular incident λ. The detection rates per panel and the global average conversion and detection efficiencies appear in the legends.

From the conversion and detection efficiency of the entire detector for different wavelengths, depicted in Figure 3.5b, it is concluded that the efficiency for lower wavelengths is lower – as expected – and the global detection efficiency is 63% with a detection to conversion ratio of 70%.

To get a deeper understanding about the detector system, the detection efficiency of each straw is shown in Figure 3.6. It is defined as the number of detected neutrons in each straw divided by the number of the respective incident neutrons. The efficiency of each straw is represented with a two-dimensional cross-sectional image of the detector geometry similar to Figure 3.2b. The efficiencies of the straws in the first panel indicate that there is a correlation between the scattering angle and the wavelength, originated from the scattering characteristics of the sample, and it is clear that the straws in the front or with clear sight to the sample have much higher efficiencies than the ones behind them. All straws are identical and so is their detection efficiency for a particular neutron wavelength, therefore the change of the detection efficiency in depth is the result of the hardening of the neutron spectrum.

Figure 3.7 depicts the time-averaged and peak incident rate for each straw represented the same way as the detection efficiency of the straws. The peak rates are extracted by counting neutrons only from a selected 1 ms ToF slice that results in the highest instantaneous rates, taking into account the pulse-repetition rate of 14 Hz. The tubes with the highest peak incident rates are localised in the centre of the panels because the highest incident rates occur when the relatively high energy neutrons are

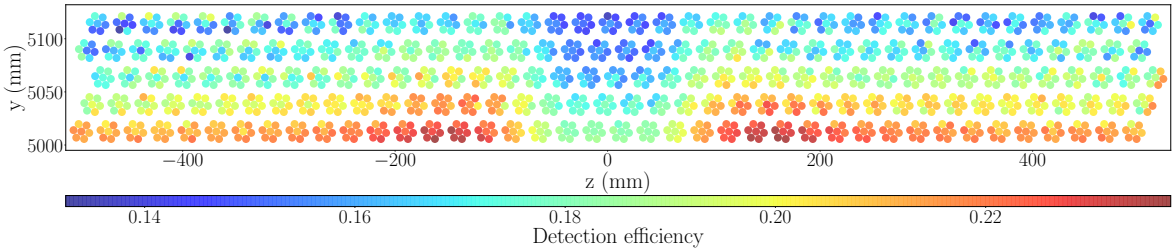

Figure 3.6: Detection efficiency per straw for instrument configuration 1.

scattered on the sample in small angles and most of them enter the same straws. Figure 3.8 gives an enlarged view of these straws and also shows the peak detected rates of the straws with the highest values.

The highest peak rates appear in the straws of the first panel in simulations with all three instrument configurations presented in Table 3.1. A summary of the estimated incident and detection rates for these configurations are presented in Table 3.3.

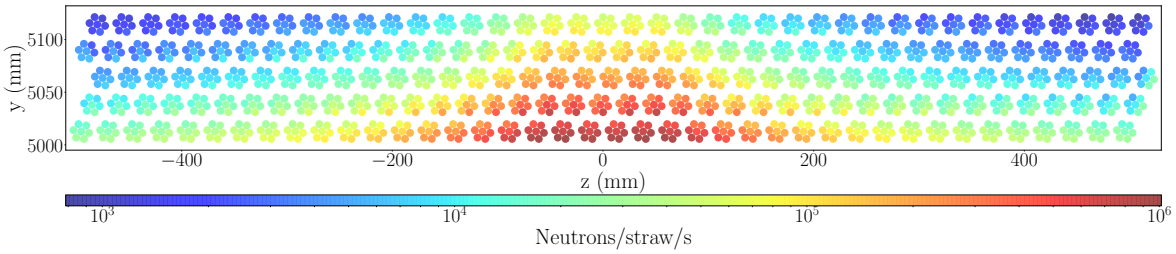

(a) Time-averaged incident rate for per BCS straw.

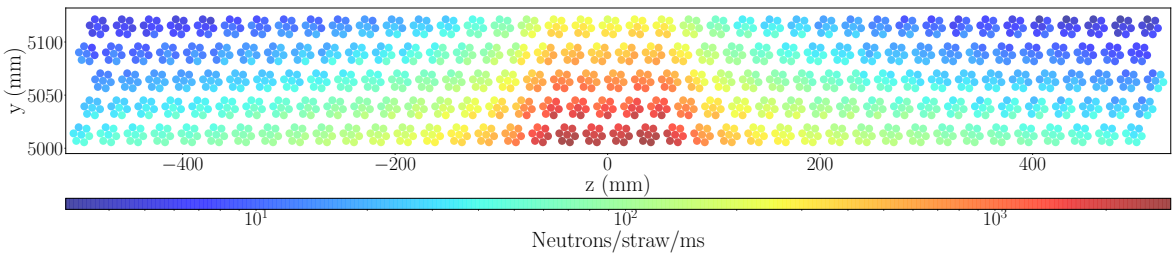

(b) Peak incident rate per BCS straw.

Figure 3.7: Time-averaged and peak incident rate per BCS straw for instrument configuration 1.

The BCS straws are expected to start saturating at 50–100 kHz. For instrument configuration 1 with the shortest instrument collimation, peak rates as high as 458 kHz for a single straw are derived. This implies that the operation of such a detector is subject to limitations.

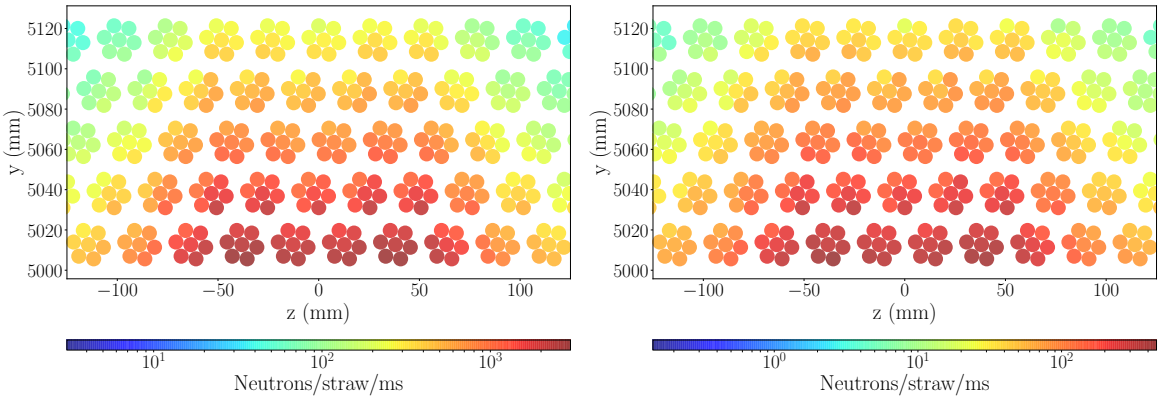

(a) (b)

Figure 3.8: Peak incident (a) and detection (b) rates for the central straws for instrument configuration 1.

Config	Global average **incident** rate	Global average **detection** rate	Local average **incident** rate/straw	Local average **detection** rate/straw
1	37.3 MHz	23.5 MHz	1.01 MHz	187 kHz
2	7.48 MHz	4.70 MHz	211 kHz	39.0 kHz
3	2.91 MHz	1.82 MHz	86.3 kHz	15.0 kHz
Config	Global peak **incident** rate	Global peak **detection** rate	Local peak **incident** rate/straw	Local peak **detection** rate/straw
1	74.3 MHz	64.2 MHz	2.99 MHz	458 kHz
2	15.1 MHz	13.1 MHz	651 kHz	100 kHz
3	6.11 MHz	5.29 MHz	283 kHz	47.0 kHz

Table 3.3: Summary table with global and local incident and detection rates for all three instrument configurations.

Chapter 4

Detector performance of the Boron-Coated Straws

As explained earlier there are various aspects of a detector that all have to fit instrument specific requirements in order to avoid becoming the bottleneck of the instrument's scientific performance. The detector development is inevitable, as upcoming research facilities and future instrument upgrades require new technologies to exceed the scientific capabilities of previous detectors. With new and stronger sources coming up it is important to fully exploit the high brilliance of a neutron pulse, that necessitates high rate capability and also high detection efficiency, that is in all cases one of the key performance parameters of a detector. This aspect of neutron detectors has come to focus with the replacement detector technologies. In those cases when the detection efficiency is low for a single detector it is natural idea to increase the efficiency by using multiple layers of them. On the other hand, this leads to an increased amount of material in the system that raises the problem of absorption in the structural materials and their activation by neutrons. Building several prototypes and to test them in multiple cases is expensive and some aspects are hard to or even impossible to measure. A simulation tool like Geant4 can shed a lot of light in these situations, especially for complex geometries like that of BCS.

In order to evaluate the use of the BCS technology – that was initially designed for homeland security – for neutron scattering experiments, a detailed simulation study is carried out using the Geant4 model introduced in Section 3.2. A generic arrangement of a point source at a 5 m distance from the centre of the geometry in vacuum is chosen. To make the results generally applicable, isotropic monochromatic conical beams are used with an opening angle of 10.6°, that ensures that the direct beam crosses all 5 panels to minimise edge effects.

In the following sections this simulation arrangement is used to investigate first the conversion and detection efficiency, then the absorption in the detector components.

In the final section the results of these simulations are used to estimate the activation of the materials in the detector.

4.1 Conversion and detection efficiency

The functional unit of a BCS detector is a single straw. The straw detection efficiency can be expressed in several valid ways. In this chapter the following definition is used:

- **Detection efficiency** is the number of neutrons detected in a straw divided by the number of incident neutrons in that straw from every direction. A neutron is counted as incident every time it enters the copper of the straw from the outside.

$$\epsilon = \frac{\#\text{ of detected neutrons in the straw}}{\#\text{ of incident neutrons in the straw}}. \tag{4.1}$$

The replacement of the number of detected neutrons with the number of converted neutrons in the numerator results in the respective conversion efficiencies.

Another relevant quantity is the detection to conversion ratio, that is the fraction of detected neutrons over converted ones. As described in Section 3.2, to get a detection event after a conversion, at least one of the conversion products has to leave the boron carbide layer and deposit enough energy in the counting gas to overcome the preset threshold. Detailed calculations of this exist [93–95]. As mentioned in Section 1.2.1 for BCS it is claimed that for 1 μm of B_4C, one of the two charged conversion products has a 78% probability to escape the converter and ionise the counting gas in the straw. This is the theoretical maximum for detection to conversion ratio, with no energy threshold. With the applied threshold of 120 keV, the simulated detection to conversion ratio is $\sim$70%, with very minor dependence of the wavelength of the converted neutrons, due to the small thickness of the B_4C layer. This value also gives an upper limit for the detection efficiency, as it is the product of the conversion efficiency and the detection to conversion ratio. The higher the threshold is, the lower the detection to conversion ratio and therefore the lower the detection efficiency will be. The optimal value depends on the gamma background of the measurement and ought to be chosen carefully. A common pulse-height spectra showing the energy deposited by the conversion products, and the energy threshold dependence of the detection to conversion ratio is presented in Appendix A.

The detection efficiency for each straw with monochromatic 0.6 Å, 3 Å and 11 Å neutrons is depicted in Figure 4.1. The efficiency of a single straw is quite low with an average of 3%, 12% and 31% respectively. This is why 7 of them are packed together

in a BCS tube and this is why employing even more overlapping straws in consecutive layers (panels) of detectors is necessary for most applications. The detection efficiency of the straws is quite uniform for a particular wavelength across all panels. This is because of the monoenergetic neutron sources used, but a previous simulations with polyenergetic neutrons in Section 3.3 demonstrated significant differences between the panels (see Figure 3.6), attributed to the hardening of the neutron spectra and the thermalisation of the neutrons via scattering. The slightly lower efficiencies in the last panels for 11 Å indicate that the thermalisation through scattering occurs indeed, and leads to neutrons with lower wavelength in the neutron spectrum and therefore lower average efficiency for the straws in the back, but also show that it is a minor effect compared to the hardening of the neutron spectra.

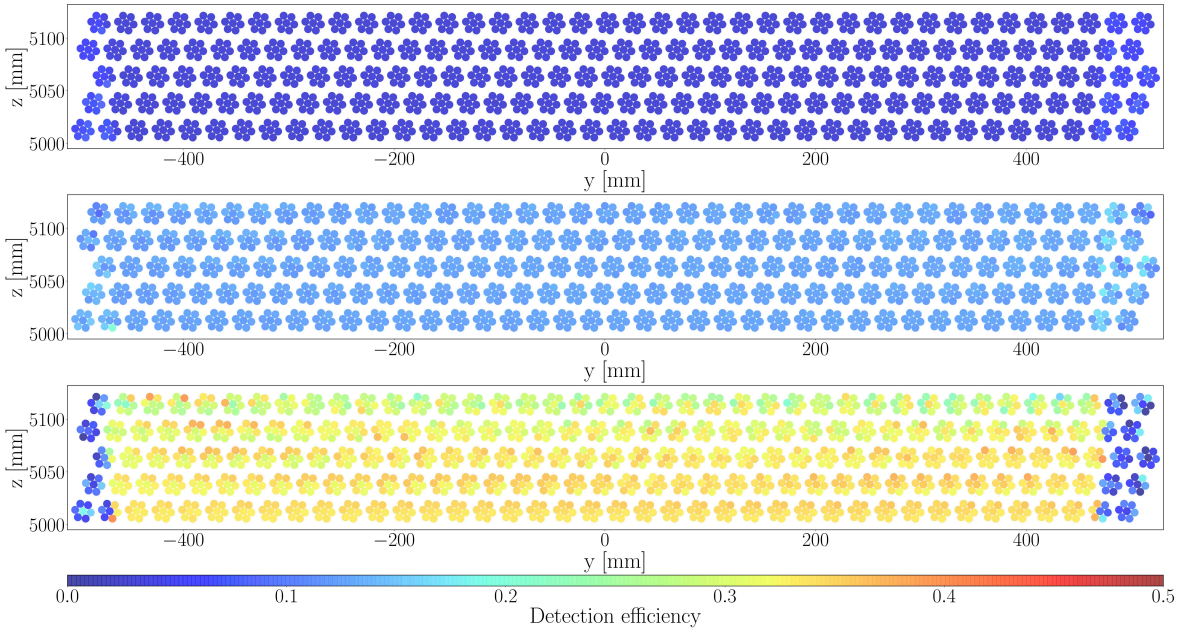

Figure 4.1: Detection efficiency of straws with monoenergetic incident neutrons. The results are visualised using the cross-section image of the 5 panel detector system. The colors represent the detection efficiency of the straws from simulations with three neutron wavelengths: 0.6 Å (top), 3 Å (middle) and 11 Å (bottom). The conical neutron source is placed at the origin, some of the straws at the edge of the panels are not illuminated directly to minimise edge effects.

Figure 4.2 depicts the contribution of each panel to the total number of detection events and the resulting global detection efficiency. For all wavelengths the first panel registers most of the detection events and the impact of the additional panel becomes lower and lower. This is more noticeable for high wavelengths where the efficiency saturates 4-5% below the maximum of 70% defined by the detection to conversion ratio. The detectors in the fifth panel contribute only a 0.21–4.27% to the global detection efficiency for the simulated neutron wavelengths. These results imply that

depending on the application and the optimum wavelength thereof, using 4 panels might be a more cost efficient solution.

The results presented are derived from simulations with all 5 panels in place. This means that efficiencies with fewer than 5 panels are somewhat overestimated because of the back-scattered neutrons from later panels, but the simulations with fewer panels showed that this effect means a <0.5% difference only.

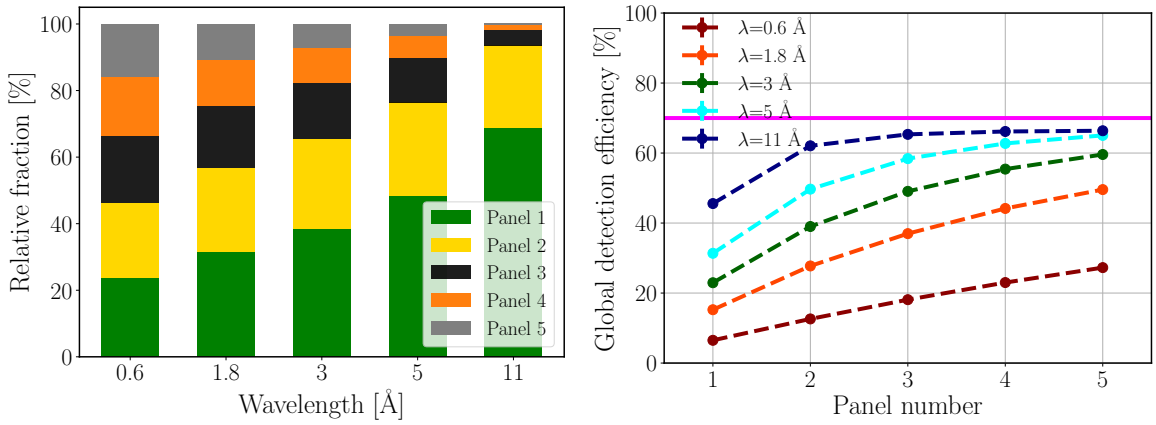

Figure 4.2: Contribution of each panel to the total number of detected neutrons (on the left) and the resulting global detection efficiency (on the right) for different wavelengths. The magenta line marks the highest possible global detection efficiency defined by the detection to conversion ratio.

It is worth mentioning that the thickness of the converter layer has an impact on the detection efficiency. As previously stated, the detection efficiency results from the convolution of the conversion efficiency and the detection to conversion ratio. The conversion efficiency could be increased by using a thicker conversion layer but that would lower the escape probability of the conversion products and consequently the detection to conversion ratio [10, 26, 93]. The cumulative effect of the converter layer thickness is wavelength dependent and not straightforward. The simulations show that for high wavelengths the global detection efficiency could be increased with lower B_4C thickness due to the increase of detection to conversion ratio but for lower wavelengths the decrease of the conversion efficiency overrules it and the detection efficiency decreases. In the other direction, the efficiency for low wavelengths can slightly benefit from thicker converter layers but for higher wavelengths where the conversion efficiency is already high, the lower detection to conversion ratio lowers the detection efficiency. In this study the commercial converter layer thickness of 1 μm is used. A more detailed investigation of converter thicknesses and efficiency optimisation is out of scope here.

4.2 Absorption in detector components

The previous section demonstrates that for achieving a higher detection efficiency it is necessary to use multiple panels of detectors. This does not only increase the number of conversion and detection events but as a consequence the undesired absorption in the non-converting materials of the detector, namely aluminium and copper also increases. However, it is not only these two materials that can absorb neutrons without leading to a detection but B_4C too. As mentioned before, not all conversion events result in a detection event because in some cases the conversion products do not exit the converter layer or they do not deposit sufficient energy in the detector gas to overcome the applied threshold. In addition, there is a rather small amount of neutron absorption in carbon and ^{11}B without conversion products to trigger a detection event. These two event classes together are hereinafter referred to as absorption in B_4C.

In a single Geant4 simulation it is possible to register the number of neutrons absorbed in aluminium, copper and B_4C separately and compare the effect of these materials. The latter could also be done with multiple simulations using different models with the materials out of focus replaced with vacuum to eliminate their effect on each other, but these effects change the results by <3% so the numbers using the model with all materials in place are presented. In Figure 4.3 the relative absorption is depicted for simulations with five different neutron wavelengths. The relative absorption in any material or materials is defined as the number of neutrons absorbed in that material over the number of incident neutrons for the entire detector system.

Most of the undesired absorption occurs in the converter layer. This is not surprising with 30% of the converted neutrons not triggering a detection event (70% detection to conversion ratio). The absorption in the copper is higher than in aluminium except for the highest wavelength (11 Å), but the difference is rather small in every case. This might be unexpected as the absorption cross-section of copper is approximately 16 times higher for these wavelengths (see Figure 4.4), but the total volume of aluminium is 17.6 times higher than that of copper, therefore the average path length of the neutrons in aluminium is much longer, an effect that compensates the cross-section difference.

It is possible to make a 'naive' analytical estimation of the absorption in a material using Equation 4.2:

$$\text{Relative absorption} = 1 - e^{-\Sigma_a \cdot l}, \tag{4.2}$$

where Σ_a is the macroscopic absorption cross-section given by Equation 4.3 and l is

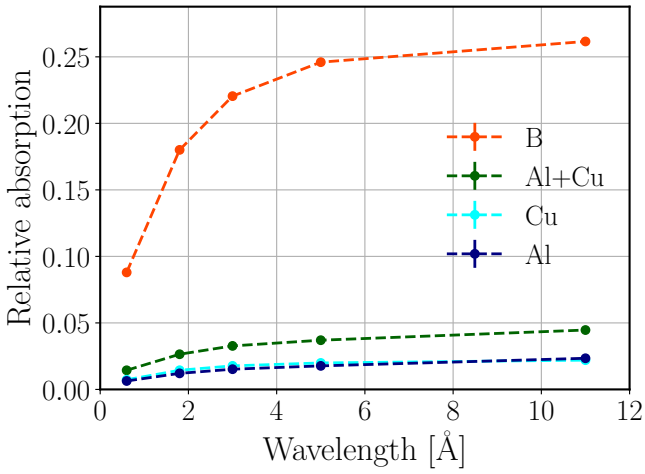

Figure 4.3: Relative absorption in the BCS detector materials as a function of incident neutron wavelength. 'B' (orange) represents the absorption in the B_4C layer not resulting in detection events. 'Cu' (cyan) and 'Al' (blue) are the relative absorption in copper and aluminium separately. 'Al+Cu' (green) is the sum of the latter two, giving the absorption in aluminium and copper together. The dashed lines only connect the markers.

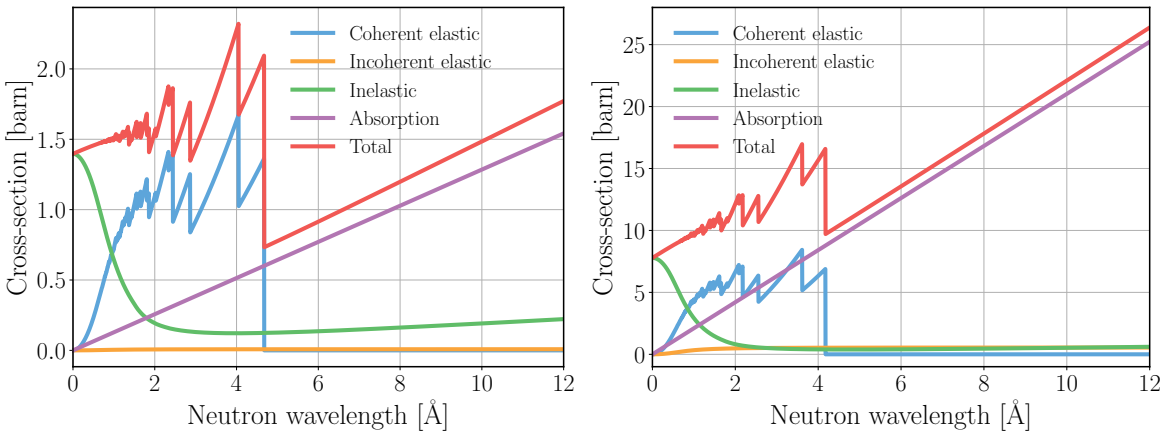

Figure 4.4: Cross-sections of aluminium (left) and copper (right) from the NCrystal library [75, 96].

the path length in a material.

$$\Sigma_a = \sigma_a \cdot \rho_A = \sigma_a \cdot \frac{\rho_m \cdot N_A}{M}, \tag{4.3}$$

where σ_a is the microscopic absorption cross-section, ρ_A is the atomic density, ρ_m is the mass density, M is the molar mass of the material and N_A is the Avogadro number.

For a specific neutron wavelength each parameter is known except the path length in the materials. One way to estimate the latter is to assume that a neutron stops halfway through the detector system after crossing an aluminium wall 2 times and a copper wall 6 times frontally in each panel. Using the wall thicknesses provided in Table 3.2 the results are l_{Al}=4.7 mm and l_{Cu}=0.375 mm. The path length of the neutrons

is, of course, not constant even for a specific wavelength, as presented in Figure 4.5. For aluminium, the beginning of the first peak in the histogram corresponds to the wall thickness of a tube, because that is the minimum distance in aluminium that a neutron has to pass to be absorbed in the converter layer of a straw. Due to the circular tube geometry and the conical beam, most of the neutrons do not enter the tube wall perpendicularly, so the neutrons absorbed in the first tube they enter can have a path length in aluminium longer than this minimum, that results in the first peak. The beginning of the second peak corresponds to three times the wall thickness of the tube, as the that is the minimum distance in aluminium for a neutron that is absorbed in the second tube it enters. The upcoming peaks are more and more blurred as the path length difference in different directions, and the number of scattered neutrons become more and more important. The last broad peak corresponds to the neutrons that pass through all panels without being absorbed and the rest of the histogram contains only scattered neutrons. Similar effects appear for copper because of the straws, but with more overlapping layers and complex geometry.

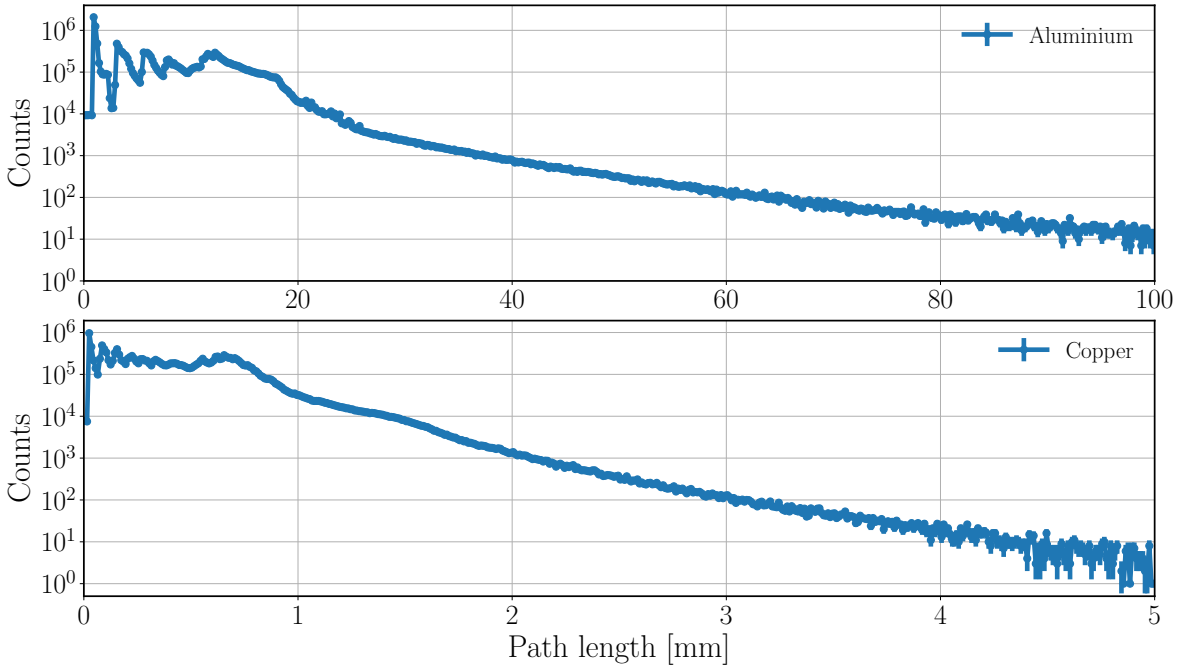

Figure 4.5: Neutron path length distribution in aluminium (top) and copper (bottom) from simulations with λ=1.8 Å for all neutrons crossing the detector regardless of whether they interact with its materials or not. The label 'Counts' means the number of neutrons with a total path length in aluminium or copper within the limits of a particular bin of the histogram.

With the average path length of the neutrons extracted from the simulations a more accurate estimate can be made proving the relevance of the formula in Equation 4.2 and supporting the results. The relative absorptions from the two estimation methods

and the results from simulation are presented in Table 4.1. The estimations using the average path lengths are in very good agreement with the simulations. All results are within 2.5%, except for the lowest wavelength but even there the difference is less than 13%. This shows how well such an easy formula describes the process of absorption in the detectors. The naive estimation also gives acceptable results, given that it is a rough estimation. Some numbers are off by a factor 3.3, but for medium wavelengths the difference is less than 70%. For wavelengths where the average path length is longer than the used fixed number, the results are underestimated, and the other way around, overestimated path lengths lead to overestimated absorptions. More accurate estimations could be made with more sophisticated formula but even in this state, both estimations support the simulation results.

λ [Å]	Rel. Abs.$_{naive}$ [%]		l_{AVG}[mm]		Rel. Abs.$_{est}$ [%]		Rel. Abs.$_{sim}$ [%]	
	Al	Cu	Al	Cu	Al	Cu	Al	Cu
0.6	0.23	0.40	11.90	0.66	0.57	0.71	0.65	0.79
1.8	0.65	1.19	8.43	0.45	1.17	1.44	1.20	1.44
3	1.13	2.00	6.38	0.33	1.52	1.78	1.51	1.76
5	1.85	3.30	4.44	0.22	1.75	1.97	1.76	1.98
11	4.02	7.11	2.69	0.11	2.32	2.19	2.30	2.15

Table 4.1: Estimated and simulated relative absorption in aluminium and copper. The naive estimations (left) are made with constant path lengths of l_{Al}=4.7 mm and l_{Cu}=0.375 mm for all wavelengths. The more accurate estimations (centre) are made with the average path lengths (l_{AVG}) from the simulations. The right column contains the relative absorption extracted from simulation alone.

Figure 4.6 shows the proportion of absorption in different materials, transmission and detection from simulations. As all neutrons enter the detector system, the proportion of detection events is by definition the global detection efficiency described in the previous section. The results indicate that for the lowest wavelengths 60-30 % of the neutrons leave the detector system even with 5 panels but for the highest wavelength this value drops below 0.5%. This high transmission number at lower and medium wavelengths emphasises the need for a shielding layer behind the panels. Proportion of absorption in aluminium and copper together is approximately 1.5% for low wavelengths and stays below 4.5% even for the highest wavelength. For the neutron wavelengths that are more relevant to neutron scattering techniques, the absorption of this scale is acceptable and justify the use of successive detection panels.

The obtained results correspond to pure unalloyed materials; alloyed materials and impurities may significantly increase the absorption due to the presence of isotopes with

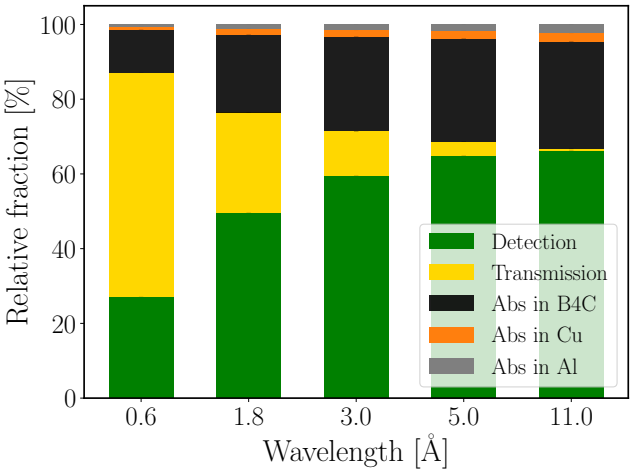

Figure 4.6: Proportion of absorption, transmission and detection from simulations with monoenergetic neutrons.

high absorption cross-section despite their low concentration. For example, the macroscopic absorption cross-section of Al5754 [97], an aluminium alloy typically used in nuclear science for mechanical structures, can be 18% higher than the pure aluminium mainly due to its manganese content.

4.3 Activation of the detector

Neutron absorption in the detector materials potentially has another negative effect besides lowering the detection efficiency, namely the neutron activation of these materials. Activation might interfere with the normal operation of the detectors in two ways. Firstly, the gamma rays and particles emitted by the excited nucleus and the decay products might form a background during measurements in addition to that of prompt gammas. Secondly, after the measurements, the radiation coming from the radioactive nuclei might not allow anyone to get close to the detectors (e.g.for maintenance) owing to the high gamma dose rate. The purpose of this section is both to determine whether the background from the activation is significant for the measurements, and to find out how much time one has to wait after the measurements to be safe to approach the detectors.

This is intended to be a generic study, therefore the activation is calculated for pure aluminium and copper instead of a specific alloy. The activation of the previously mentioned aluminium alloy Al5754 is already investigated in [98]. In that work it is also concluded that the activation of the Ar/CO_2 is a minor effect compared to the

same of the aluminium-housing, and the beta radiation is negligible both in terms of background and radiation protection, so these aspects are not addressed here.

At spallation sources the detectors are irradiated in pulses, but as the pulses and repetition times are much shorter than activation and decay times of the relevant isotopes, therefore a constant average flux with the same integral can be used to determine activation. The calculations are performed for a constant flux of 10^9 n/cm^2/s on a 1 cm^3 cubic sample, assuming 5% of neutrons are scattered toward the detectors. These numbers represent a conservative estimate of the worst case scenario for an intended SANS application investigated in Chapter 3 but the results to be presented scale linear with the flux, making it is easy to adopt them to any other particular application. This assumption gives an incident flux of $5 \cdot 10^3$ n/cm^2/s for the 1 m^2 detector system, that means a neutron intensity of $5 \cdot 10^7$ n/s. Using this number as source intensity for the previously introduced simulation arrangement, the intensity of neutron absorption in each material can be calculated for different monoenergetic beams using the relative absorption results from Table 4.1. The results of these monoenergetic beams covering the most relevant wavelength range can be used to give estimation for a particular neutron spectrum by choosing the most representative wavelength or by corresponding segmentation using the upper wavelength for each range. The estimation presented here is done for 3 Å neutrons, with 1.51% and 1.76% of neutrons absorbed in aluminium and copper, respectively. From the neutron absorption intensity, the activation of an isotope is calculated for the irradiation duration t_{irr} with Equation 4.4,

$$a(t_{irr}) = I_a \cdot (1 - \exp(-\lambda \cdot t_{irr})) \tag{4.4}$$

where I_a is the neutron absorption intensity and λ is the decay constant of the regarded isotope. Pure aluminium contains only the ^{27}Al isotope, but copper has two natural isotopes – ^{63}Cu and ^{65}Cu, so the absorption intensity is shared between them with respect to the their natural abundance and absorption cross-section. Neutron activation of the activation products (secondary activation) is neglected due to the low probability of the multiple neutron capture by the same nucleus. The irradiation time for the calculations is 10^6 s (≈11.5 days), that will be approximately an operation cycle for ESS.

The activity of an isotope after irradiation and cooling time t_c is given by Equation 4.5,

$$a(t_c) = a_0 \cdot \exp(-\lambda \cdot t_c) \tag{4.5}$$

where a_0 is the activity reached by the end of the irradiation.

In order to express the results in activity concentration, the total activity of the isotopes are normalised with the total volume of the respective material. The vol-

ume of aluminium and copper for the five detector panels are V_{Al}=14447 cm^3 and V_{Cu}=822 cm^3. The activity concentration of the isotopes of interest during irradiation and cooling are presented in Figure 4.7.

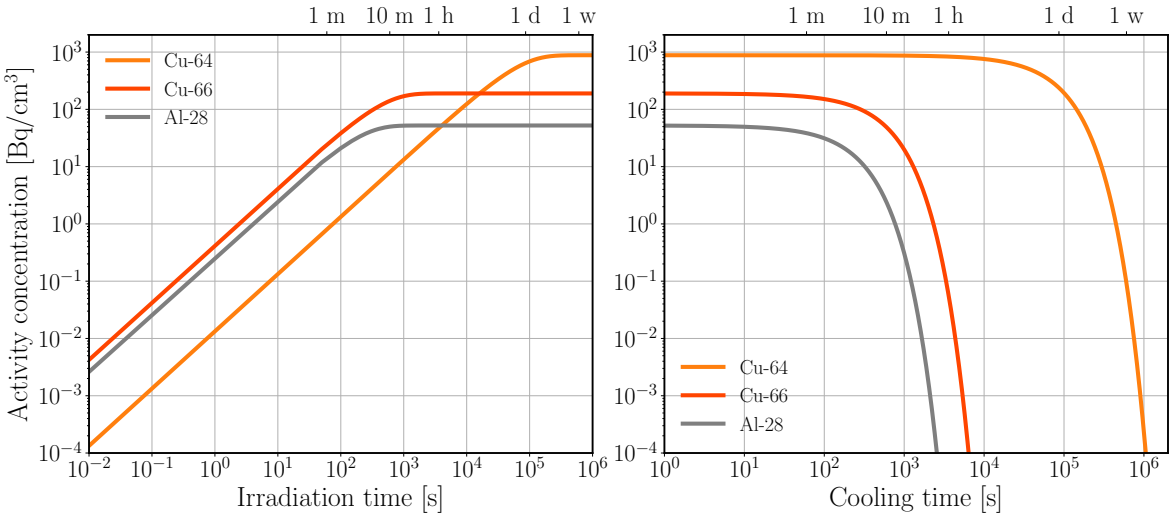

Figure 4.7: Activity concentration of the produced radionuclei during 10^6 s of irradiation with 3 Å neutrons and during the cooling period.

The results show that the activity concentration of the produced radionuclei saturates by the end of irradiation time. These end values are used to calculate the decay gamma emission of these radionuclei from a unit volume per second. In this study the gamma efficiency is approximated conservatively with 10^{-7} [10, 91] for all photon energies. Due to the constant gamma efficiency, only the total number of photons per decay has to be determined regardless of the photon energies. In order to do that, the yields of the possible decay gamma lines presented in Table 4.2 are summed, resulting in a gamma yield of $\gamma_{d,Al-28}$=1.0, $\gamma^*_{d,Cu-64}$=4.73·10^{-2}, $\gamma_{d,Cu-66}$=9.22·10^{-2} photons per decay. In addition to decay gammas, ^{64}Cu emits a positron in 17.40% of the decays, that will produce 2 photons of 511 keV by annihilation. These photons dominate the total gamma yield of ^{64}Cu, that is $\gamma_{d,Cu-64}$=0.353. The x-rays from decay and the bremsstrahlung of the emitted electrons are neglected due to their low energy compared to a reasonable pulse height threshold. With the saturation activity concentration values of A_{Al-28}=52.3 Bq, A_{Cu-64}=881 Bq and A_{Cu-66}=190 Bq, the gamma intensities are $I_{d,Al-28}$=52.3 s^{-1}, $I_{d,Cu-64}$=331 s^{-1} and $I_{d,Cu-66}$=17.5 s^{-1} for a unit volume. For the total volume of aluminium and copper, the gamma intensity is $I_{\gamma_{Al}}$=7.55·10^5 s^{-1} and $I_{\gamma_{Cu}}$=2.70·10^5 s^{-1}. The total decay gamma intensity for the whole detector system is I_{γ_d}=1.025·10^6 s^{-1}.

The prompt gamma intensity (I_{γ_p}) for aluminium and copper is calculated as the

Isotope	E [keV]	Yield [%]	Flux to dose $[\frac{\mu Sv/h}{\gamma/cm^2s}]$
Al-28	1778.969	100	0.02473
Cu-64	1345.84	0.473	0.02028
Cu-64*	511	34.8	0.00907
Cu-66	833.537	0.220	0.01387
Cu-66	1039.231	9	0.01666
Cu-66	1333.120	0.0037	0.02013

Table 4.2: Decay gamma lines of the activated isotopes with their production yield per decay [99] and the flux to dose conversion factor corresponding to the photon energy [100]. The 511 keV photons of Cu-64 are the results of the annihilation of the emitted positrons.

product of the neutron absorption intensity and the total prompt gamma yield per absorption (γ_p) for each material (see Equation 4.6).

$$I_{\gamma_p} = I_a \cdot \gamma_p = I_a \cdot \frac{\sum_i \sigma_{\gamma_i}}{\sigma_a} \tag{4.6}$$

The number of prompt gammas per absorption is estimated as the ratio of the sum of the gamma line specific cross-sections (σ_{γ_i}) and the absorption cross-section (σ_a) [101]. Due to the gamma cascades, this ratio is not unity, the resulting yields are $\gamma_{p,Al}$=1.978 and $\gamma_{p,Cu}$=2.665. The prompt gamma intensities are I_{Al}=1.493·10^6 s^{-1}, I_{Cu}=2.345·10^6 s^{-1} and the total prompt gamma intensity is I_{γ_p}=3.839·10^6 s^{-1}.

The total prompt and decay gamma intensity of aluminium and copper is I_γ=4.864·10^6 s^{-1}. This intensity is so low that it is overruled by the intensity of photons from the conversion process. In about 94% of the neutron conversions in ^{10}B, a 0.48 MeV gamma is emitted [59]. Using the relative absorption ratio of B_4C for 3 Å neutrons from the absorption section, neglecting the neutron absorption of carbon and ^{11}B, 25.31% of the incident neutrons are converted. This translates to a gamma intensity of I_{γ_B}=1.190·10^7 s^{-1} from the converter layer. As this is the key source of photons, the total gamma intensity of the detector system for the observed neutron flux is on the order of 10^7 for all relevant wavelengths. With a gamma efficiency of the BCS detectors on the order of 10^{-7}, the gamma background coming from the detector itself is negligible compared to the detected neutron intensity on the order of 10^7 n/s.

In terms of dose rate after the irradiation, the detector system can be approximated as a surface source of 100×100 cm^2, emitting photons with the source intensity and energy corresponding to the decay gamma intensity and energy of the activated isotopes. The resulting fluxes at the end of the irradiation time are Φ_{Al}=37.75 $cm^{-2}s^{-1}$, Φ_{Cu-64}=12.78 $cm^{-2}s^{-1}$, Φ_{Cu-66}=0.72 $cm^{-2}s^{-1}$. The fluxes are dominated by the

1778.969 keV, 511 keV and 1039.231 keV energy photons, respectively, so the fluxes are turned into dose rate with the corresponding flux to dose rate conversion factors presented in Table 4.2. Resulting dose rates are $\dot{D}_{Al}$=0.934 μSvh^{-1}, $\dot{D}_{Cu-64}$=0.116 μSvh^{-1} and $\dot{D}_{Cu-66}$=0.012 μSvh^{-1} with the total value of $\dot{D}$=1.062 μSvh^{-1}. The dose rate after certain cooling time can be calculated in the same way and the results can be scaled for similar detector setups.

As already mentioned, the obtained results correspond to pure unalloyed materials; alloyed materials and impurities may significantly increase the activity and dose rate due to isotopes with high cross-section or long half-life. This investigation assumed cold neutrons and single neutron activation, but for fast neutrons other reaction, like ^{63}Cu(n,α)^{60}Co or ^{63}Cu(n,p)^{63}Ni must be taken into consideration.

Chapter 5

Scattering effects in the Boron-Coated Straws detectors

In Section 4.1 it is demonstrated that for most applications successive layers (panels) of BCS detectors are needed to achieve acceptable detection efficiency. There are drawback of the presence of more detector tubes and therefore more material in the detector system. The increase of undesired absorption in the non-converting materials of the detector and the resulting activation is already discussed in Sections 4.2 and 4.3. There is, however another side effect of the added detector material budget: an increase in the scattering of neutrons inside the detector system. In contrast to absorption, scattering can degrade the detector performance by producing false signal or intrinsic background, which in turn can impact the signal-to-background ratio. The latter is a driving requirement in particular for inelastic neutron instruments and has to be carefully considered in the detector design process.

In order to examine the effects of neutron scattering inside the detector system, the Geant4 model introduced in Section 3.2 is used with the same isotropic monochromatic neutron beams as in Chapter 4. With this simulation arrangement the impact of scattering is analysed and quantified on several quantities relevant for different neutron scattering techniques. The study includes the separation of different material's effect on scattering and the effect of different numbers of detector panels and different neutrons wavelengths. The tools and quantification methods implemented for the study are also used to investigated the usability of a polyethylene "afterburner" block placed behind 5 panels of detectors to enhance the detection efficiency by reducing the transmission.

In the following sections first the quantities of interest are introduced, then the qualitative and quantitative analysis of the scattering effects on these quantities is presented for several simulation parameters, and finally in the last section the potential of such simulation tools is demonstrated through the investigation of the usability of the polyethylene "afterburner" block.

5.1 Quantities of interest

The definition of signal and background depends on the detector application, as different quantities might be relevant for the respective measurement technique. Moreover, there are different ways to quantify scattering in a detector, each giving a different but still valid insight. A series of studies have already quantified the effect for the Multi-Blade and the Multi-Grid detectors [85, 102, 103]. In the study that follows, rather than only look at the SANS application initially foreseen for BCS; all quantities of interest are looked at, so that the results may be considered in the context of all techniques, i.e. reflectometry, diffraction and spectroscopy.

The following raw (in boldface font) and derived quantities are of interest for the scattering study:

- **X**: position along the straws (along the wire).
- **Y**: position perpendicular to the straws.
- **ToF**: neutron time of flight from the source until the detection.
- Θ: polar angle calculated from the source and the detection event X and Y positions.
- Φ: azimuthal angle calculated from the source and the detection event X and Y positions.
- λ: neutron wavelength calculated from the distance between the source and the detection event position (SDD) and the ToF, using Equation 5.1 as

$$\lambda = \frac{h}{m \cdot v} = \frac{h}{m} \cdot \frac{ToF}{SDD}, \tag{5.1}$$

  where h is the Planck constant, m is the neutron mass and v the velocity.
- E: neutron energy calculated from λ.
- Q: scattering vector calculated from Θ and λ, using Equation 5.2 (SANS definition):

$$Q = \frac{4\pi}{\lambda} \sin\left(\frac{\Theta}{2}\right). \tag{5.2}$$

The detection events' two coordinates perpendicular to the straw are defined by the virtual position of the wire in the centre of the straw. In order to get the third,

longitudinal coordinate, first the weighted average of the deposited energy by the conversion products is determined, then a Gaussian distribution with that mean value is sampled. The full width at half maximum (FWHM) for this smearing is set to 0.6 cm based on experimental results [45, 88]. Although the longitudinal resolution for a tube detector depends on the position along its length (higher in the centre than closer to the ends [46]), and is very much a function of the analogue quality and signal treatment in the electronic readout, this study assumes uniform resolution.

Scattering, elastic and inelastic, leads to a change in the detection coordinates and subsequently in all derived quantities in almost every case. To quantify this change, the ideal values of these quantities must be defined for each neutron. These values correspond to a non-scattered neutron generated with the same initial parameters. Without scattering, the neutron λ and direction (Θ and Φ) remain unaltered. The ideal values of these parameters are easy to define. Q is derived from Θ and λ so its ideal value is also straightforward to estimate. For the remaining quantities an ideal detection point and time have to be defined. This could be done in many ways but for this study it is defined as the position extrapolated from the source's position and the neutron's initial Θ and Φ to the Z plane of the actual detection event, as demonstrated in Figure 5.1. From the ideal detection coordinates the ideal X, Y and ToF values are calculated. The difference of the simulated and ideal quantities are referred to hereinafter as δX ($=\delta X_{sim}$-δX_{ideal}), δY, $\delta\Theta$ and so on.

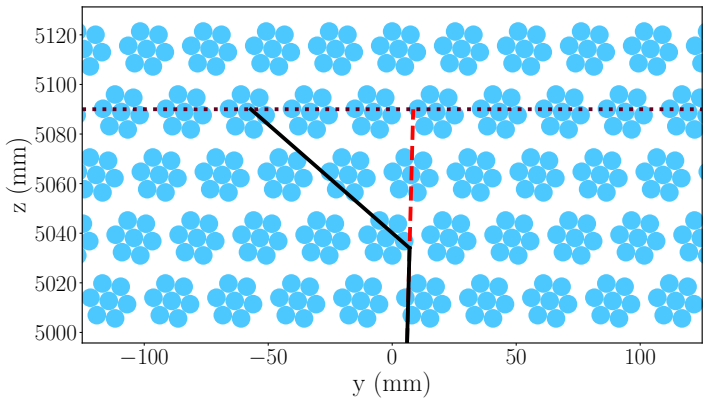

Figure 5.1: Demonstration of the ideal detection point for a scattered neutron. The black line represents the track of a neutron that is scattered in the second panel before being converted and detected in the fourth panel. The red dashed line shows the track of the ideal, non scattered neutron, that is the continuation of the simulated neutron's initial direction until the Z plane of its detection point, indicated with the dotted line.

Due to the statistical behavior of the detection process, and discrete Y and Z detection coordinates defined by the anode wires, the δ quantities are not zero even for

the non-scattered neutrons. Therefore, in order to decide what is signal and what is background, an upper and a lower limit are selected for all quantities. The detection events with a δ value within the limits are counted as signal for the respective quantity.

Figure 5.2 demonstrates the process of finding the signal limits for δX. A Gaussian

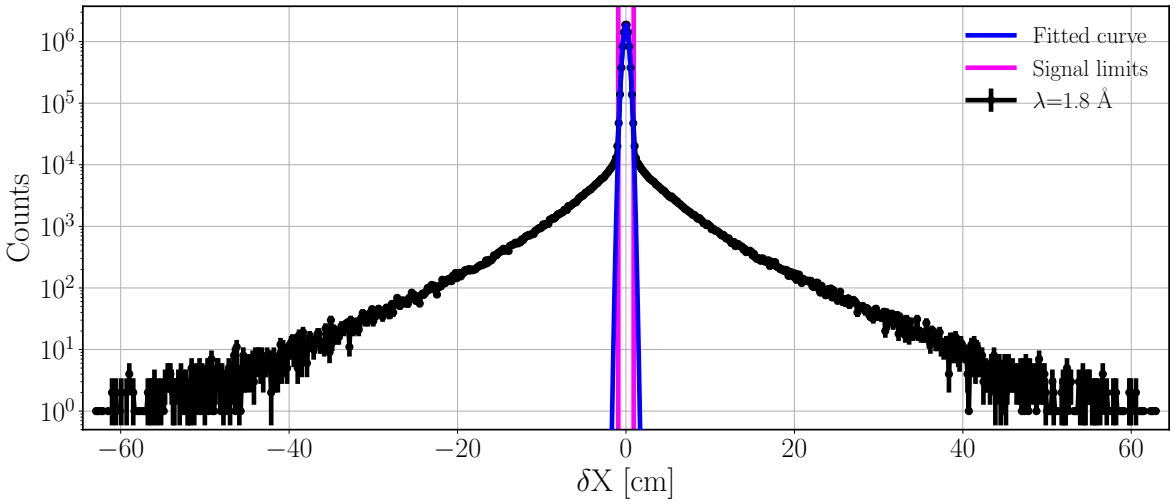

Figure 5.2: Finding the limits for signal and background separation for δX using the results from simulation with 1.8 Å monoenergetic beam. The Gaussian function (blue) is fitted on the data (black) with the 3σ limits appearing in red.

function is fitted to the δ distribution, and the limits are defined as the mean value $\pm 3\sigma$. The same method cannot be applied to δY, as Figure 5.3 shows clearly that a Gaussian fit is not appropriate. The shape in the centre is the result of using the position of the wire in the centre of the straw instead of the exact coordinates of the detection event. The maximum difference in Y caused by using the wire coordinate is the outer radius of the converter layer. The peak corresponds to this difference so all neutrons which follow a straight line until their conversion are contained in it. This means that the straightforward limit for the separation of signal and background is the outer radius of the converter layer, which is the same as the inner radius of the straw.

δToF is the difference of the simulated ToF and the ideal ToF. The former is the time until the neutron reaches its conversion point from the source plus the time until the conversion products deposit enough energy to overcome the applied detection threshold. The ToF of the conversion products is negligible compared to the ToF of the neutrons for any relevant distance because they have a much higher velocity due to their initial kinetic energy, so the simulated ToF is practically the ToF of the neutrons until the conversion point. The ideal ToF is calculated from the initial wavelength and the distance between the source and the ideal detection point. For a non-scattered neutron the wavelength, and therefore the velocity does not change, so δToF comes

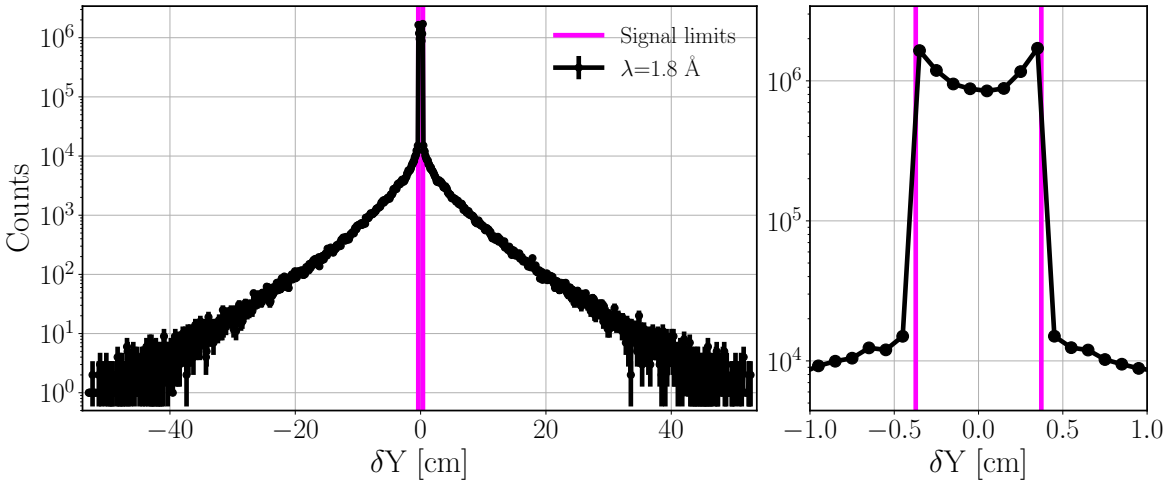

Figure 5.3: Finding the limits for signal and background separation for δY with a 1.8 Å monoenergetic beam. The limits given by the straw inner radius are ±3.725 mm. The figure on the right shows an enlarged view of the centre part of the figure on the left. The lines are only joining the points.

from the different distances from the source to the conversion point and to the ideal detection point. This distance is related to the ion range, that appears to agree with the radius of the straws. Therefore, the δToF limits to separate signal and background are calculated from the ToF difference caused by this spatial difference, that depends on the neutron velocity so different limits are defined for the wavelengths of interest.

The effect of the discrete Y and Z detection coordinates also appears for λ. The ideal λ is calculated from the ToF and the source to detection point distance (SDD) according to Equation 5.1, but for the simulated λ, the distance between the source and the detection event wire coordinates (SWD) is used. The maximum difference between source to detection point distance and source to detection event's wire coordinates distance is the inner radius of the straw. The resulting $\Delta\lambda$ difference for a non-scattered neutron is calculated using Equation 5.3

$$\Delta\lambda = \lambda_{sim} - \lambda_{ideal} = \frac{h}{m} \cdot \frac{ToF}{SWD} - \frac{h}{m} \cdot \frac{ToF}{SDD}. \tag{5.3}$$

$\Delta\lambda$ depends on the SDD and the corresponding ToF. The highest difference, that gives good limits for the signal and background separation appears for the shortest SDD, that is 5 m. The ToF and therefore the $\delta\lambda$ limits depend on the initial velocity of the neutrons, so different limits are defined for the 5 wavelengths of interest. Neutron energy is calculated directly from λ, so the signal and background separation for $\delta\lambda$ is valid for δE, and therefore not repeated. The limits for $\delta\Theta$, $\delta\Phi$ and δQ are defined the same way as for δX, by fitting a Gaussian function. The δQ limits are wavelength dependent, so they are defined for each wavelength of interest.

For all quantities where the limits are defined by the parameters of the fitted Gaussian function, the mean is at least 3 orders of magnitude lower than the standard deviation, so for simplicity zero is used instead. This means that the range for any δ quantity, within which a detection event is considered as signal is $\pm$ the corresponding limit. The width of all signal ranges are presented in Table 5.1 and Table 5.2. The figures showing the limits visually, similarly as for δX (Figure 5.2) and δY (Figures 5.3), are placed in Appendix B (see Figure B.1–B.5). The separation of signal and background using the limits is applied on the raw data instead of the histograms, to avoid possible distortions caused by the arbitrary binning choices.

Quantity	Width of signal range
δX [cm]	1.75
δY [cm]	0.75
$\delta\Theta$ [degree]	0.21
$\delta\Phi$ [degree]	3.25

Table 5.1: The width of the ranges within which detection events are considered as signal for quantities with limits independent of the neutron wavelength. The limits are $\pm$ half of the width presented in this table.

Quantity	Width of signal ranges for different wavelengths				
	0.6 Å	1.8 Å	3 Å	5 Å	11 Å
δToF [μs]	0.57	1.70	2.83	4.71	10.63
$\delta\lambda$ [Å]	$4.5{\cdot}10^{-4}$	$1.34{\cdot}10^{-3}$	$2.24{\cdot}10^{-3}$	$3.73{\cdot}10^{-3}$	$8.20{\cdot}10^{-3}$
δQ [1/Å]	$1.95{\cdot}10^{-2}$	$6.3{\cdot}10^{-3}$	$3.8{\cdot}10^{-3}$	$2.2{\cdot}10^{-3}$	$1.0{\cdot}10^{-3}$

Table 5.2: The width of the ranges within which detection events are considered as signal for quantities with wavelength dependent limits. The limits are $\pm$ half of the width presented in this table.

5.2 Impact of scattering

5.2.1 Spatial resolution

The FWHM of the δX distribution is 0.67 cm, which is a convolution of the detection coordinate approximation with the weighted average of the deposited energy by the conversion products and the applied smearing with a FWHM of 0.6 cm. Small local scatterings could also cause the broadening of the peak. In order to evaluate this effect,

the δX distribution is shown in Figure 5.4 consecutively estimated with the neutron conversion coordinates, the approximated detection coordinates and finally with the application of position smearing on top of the latter. The results demonstrate that the broadening of the peak because of scattering inside the detector is negligible compared to the other processes of the detection. This means that scattering inside the detector does not affect the spatial resolution of the detector.

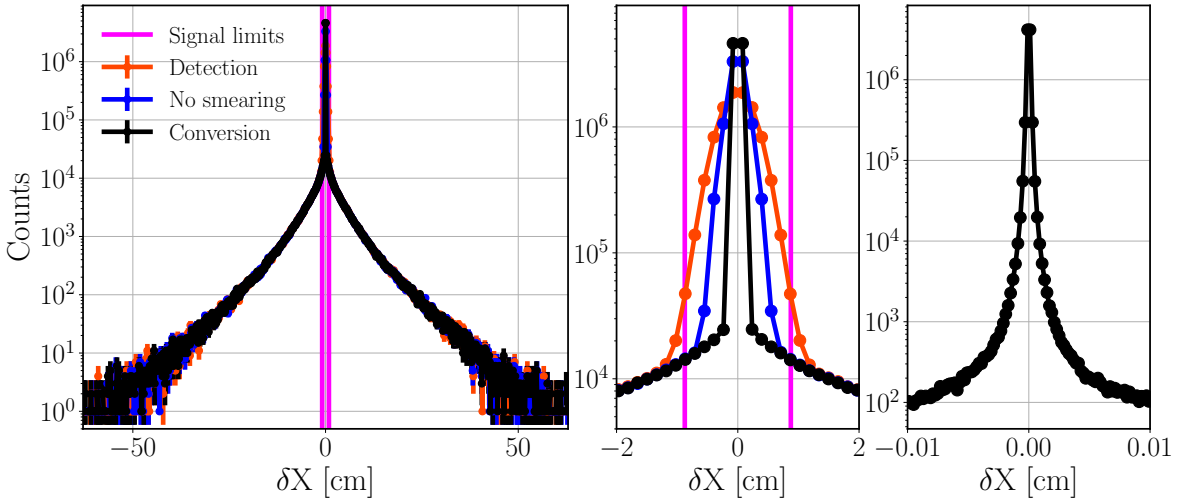

Figure 5.4: Decomposition of the peak broadening effects for λ=1.8 Å. δX is shown for the neutron conversion coordinates (black), for the approximated detection coordinates (blue) and for the approximated detection coordinates with the application of position smearing (red). The figure on the right shows only δX for the conversion point in the centremost range with finer binning to reveal the shape of its peak. The lines are only joining the points.

5.2.2 Panels and material budget

Figure 5.5 depicts $\delta\Theta$ for a different number of detector panels for 1.8 Å neutrons. It can be seen that the overall fraction of scattered background increases with the number of panels. The increase of the scattered background with every additional panel has two components. First, there are scattered neutrons detected in the downstream panels. Second, there are neutrons backscattered from the downstream panels that are detected upstream.

In order to distinguish the scattering effects of the different materials, simulations are performed with 4 different detector models derived from the original one by leaving out some of the materials. All of the models included the Ar/CO_2 gas and the B_4C layer as they are indispensable for the detection. One of the models had nothing more in it, and two others included either the copper straws or the aluminium tubes. The last one was the original model with both aluminium and copper in place.

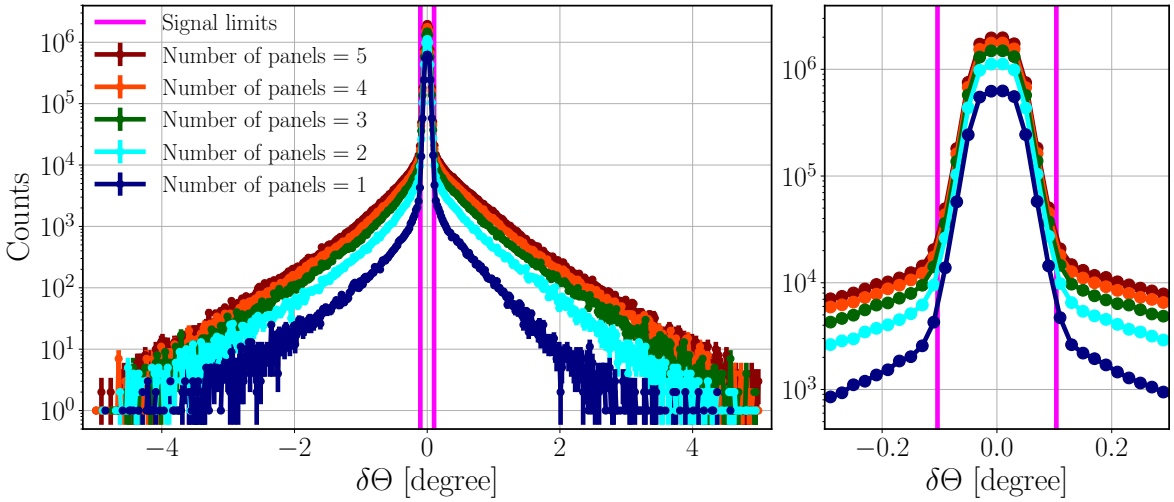

Figure 5.5: $\delta\Theta$ for different number of panels from simulations with λ=1.8 Å. The signal limits are defined from simulation with 5 panels. The figure on the right shows an enlarged view of the centre part of the figure on the left. The lines are only joining the points.

Figure 5.6 depicts $\delta\Theta$ for the different detector models with 1.8 Å neutrons. Though the quantitative approach to determine the amount of relative scattering is presented in Section 5.2.4, it is already visually clear that the original model that contains all materials produces the highest scattered background. From the simulations with either aluminium or copper left out, it is clear that aluminium is the main source of the scattering. Similarly to absorption, the scattering cross-section of copper is generally much higher (approximately 5 times higher for 1.8 Å), but in this case the difference is not high enough to compensate the presence of 17.6 times more aluminium.

For the rest of the quantities the scattered background shows similar trends as a function of number of panels and detector materials, therefore only their wavelength dependence is presented using the original model of 5 detector panels with all materials in place.

5.2.3 Neutron wavelength

Figure 5.7 depicts δX for various monoenergetic neutron beams. For all wavelengths there is a peak inside the signal range and tails on both sides outside the limits, so it is visually easy to separate the signal and the scattered background. The first and most notable thing is that for higher wavelengths the background gets lower. This result is not as evident as it might seem, because in some regions the total scattering cross-section of aluminium and copper increases, and with the higher conversion and detection efficiency due to the also increased absorption cross-section of the B_4C, more and more of the scattered neutrons are detected. On the other hand, the increased

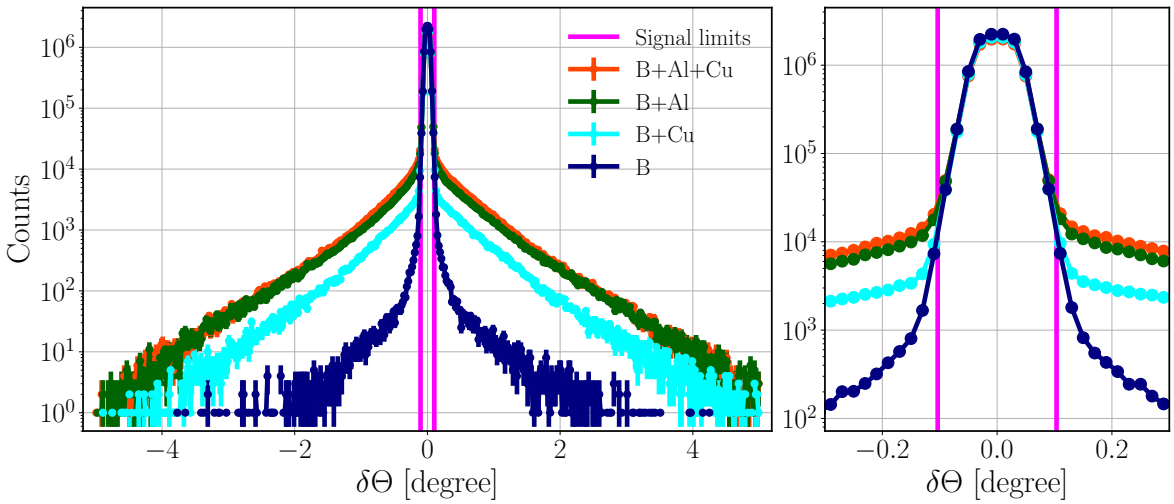

Figure 5.6: $\delta\Theta$ for different detector models from simulations with λ=1.8 Å. The model labeled with 'B' contains only Ar/CO_2 gas and the B_4C converter layer. The models 'B+Cu' and 'B+Al' contain either the copper straws or the aluminium tubes. 'B+Al+Cu' represents the original model with all materials in place. The signal limits are defined from simulation with the original model. The figure on the right shows an enlarged view of the centre part of the figure on the left. The lines are only joining the points.

absorption in the converter layers reduces the average path length of the neutrons in aluminium and copper, and therefore the amount of scattering. The results show the latter effect is stronger. The significant drop in the background between 3 Å and 5 Å is the result of the Bragg cut-off that is at 4.174 Å for copper and 4.676 Å for aluminium (see Figure 4.4). Above these wavelengths, there is no Bragg scattering in the materials, only incoherent, and coherent inelastic scattering. Figures 5.8–5.10 demonstrate the same effects for δY, $\delta\Theta$ and $\delta\Phi$. Even though $\delta\Phi$ shows non-gaussian shape, the signal defined by the limits from fitting Gaussian function is in good accordance with signal from other quantities.

The simulated λ is not necessarily equal to the physical wavelength of the detected neutron. It is a measured λ that is calculated from ToF with Equation 5.1, hence $\delta\lambda$ and δToF are closely connected. Scattering inside the detector can change the ToF in two ways: by changing the direction and the wavelength of the neutron, in case of inelastic scattering. Both effects have a complex impact on ToF, leading to either increase or decrease thereof. A change in the direction can greatly increase the path length of a neutron inside the detector but it can also decrease it in case the next converter layer is closer in the new direction. Thermalisation through scattering generally leads the neutrons toward thermal neutron wavelength but for the wavelength range of interest between 0.6–11 Å this can mean both increase and decrease. With increased wavelength the neutrons travel slower inside the detector, which could result in higher ToF. On

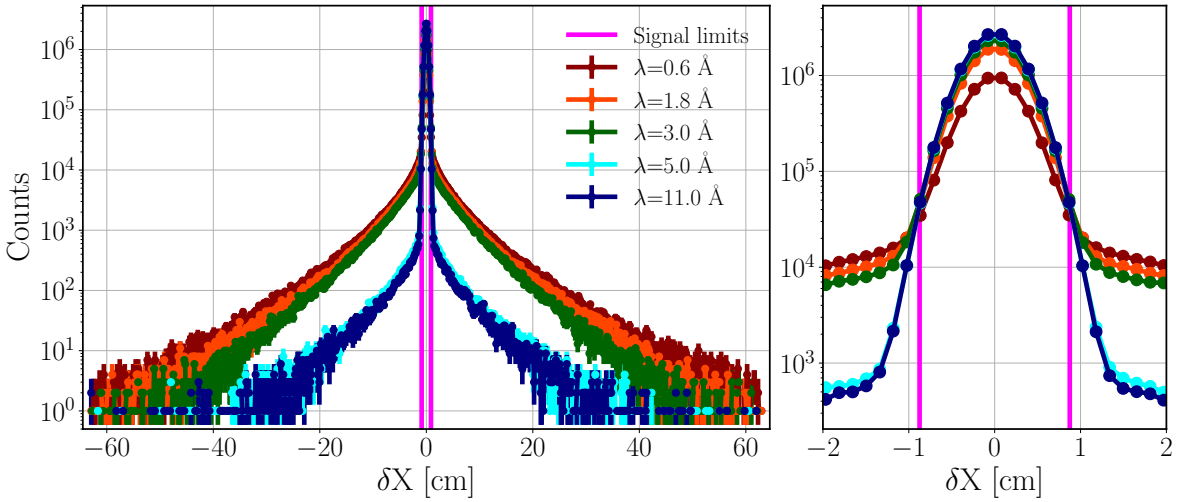

Figure 5.7: δX for different neutron wavelengths. The signal limits are defined based on results from simulation with λ=1.8 Å. The figure on the right shows an enlarged view of the centre part of the figure on the left. The lines are only joining the points.

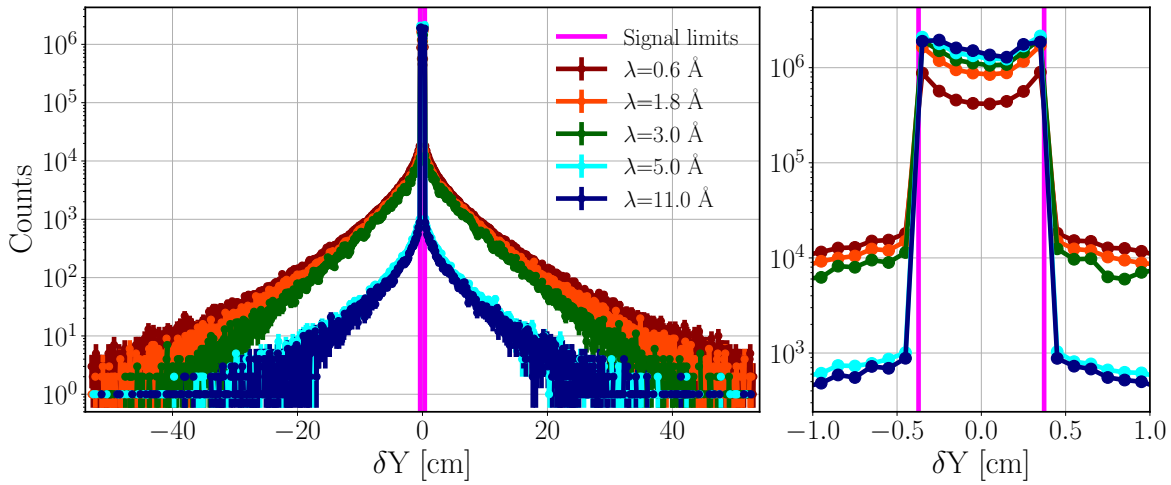

Figure 5.8: δY for different neutron wavelengths. The signal limits are defined as the inner radius of the copper straws. The figure on the right shows an enlarged view of the centre part of the figure on the left. The lines are only joining the points.

the other hand, higher wavelength also implies a higher absorption cross-section and therefore possibly a shorter path length, and the other way around. The cumulative effect is shown in Figures 5.11 and 5.12. For shorter wavelengths clearly the positive δ values are dominant. This means that for these neutrons ToF generally increases due to scattering and so does the resulting λ. Going for longer initial wavelengths, the negative side becomes more and more significant. This proves that shorter measured ToF and λ as a result of scattering can be just as important as longer.

The change in the measured λ due to scattering inside the detector can be ex-

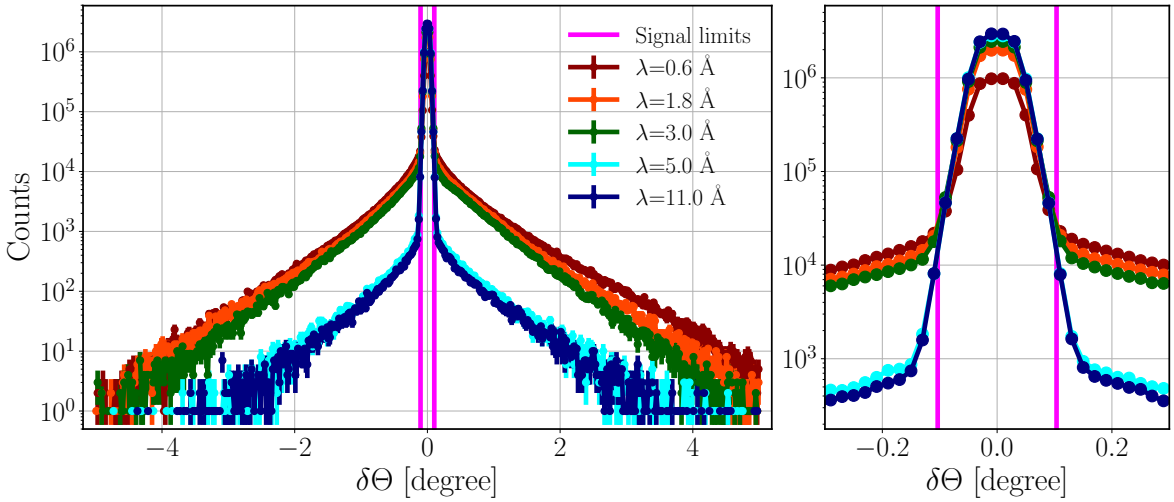

Figure 5.9: $\delta\Theta$ for different neutron wavelengths. The range of signal is indicated with pink vertical lines. The signal limits are defined form simulation with λ=1.8 Å. The figure on the right shows an enlarged view of the centre part of the figure on the left. The lines are only joining the points.

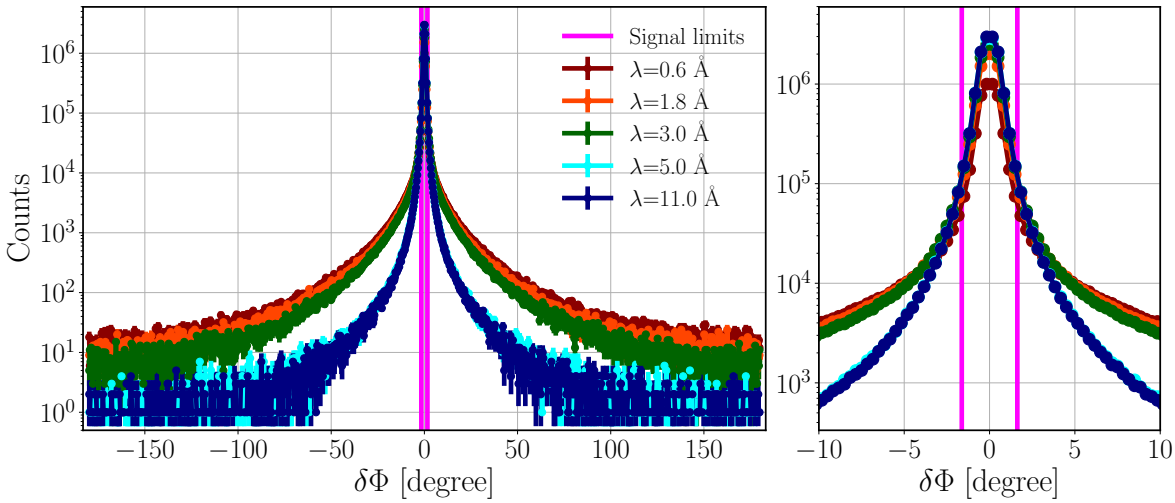

Figure 5.10: $\delta\Phi$ for different neutron wavelengths. The signal limits are defined based on results from simulation with λ=1.8 Å. The figure on the right shows an enlarged view of the centre part of the figure on the left. The lines are only joining the points.

pressed in terms of change in the measured neutron energy, that can be important when observing energy transfer in real samples. Figure 5.13 depicts the change in the measured energy for different wavelengths. The scale of δE depends on the initial λ, so different ranges are highlighted in the subplots to provide information about the relevant wavelengths.

Q is derived from Θ and λ (see Equation 5.2) so δQ depends on all phenomena mentioned earlier in connection with these quantities. The results are depicted in Figure 5.14. The wavelength dependency of both the signal and the background is

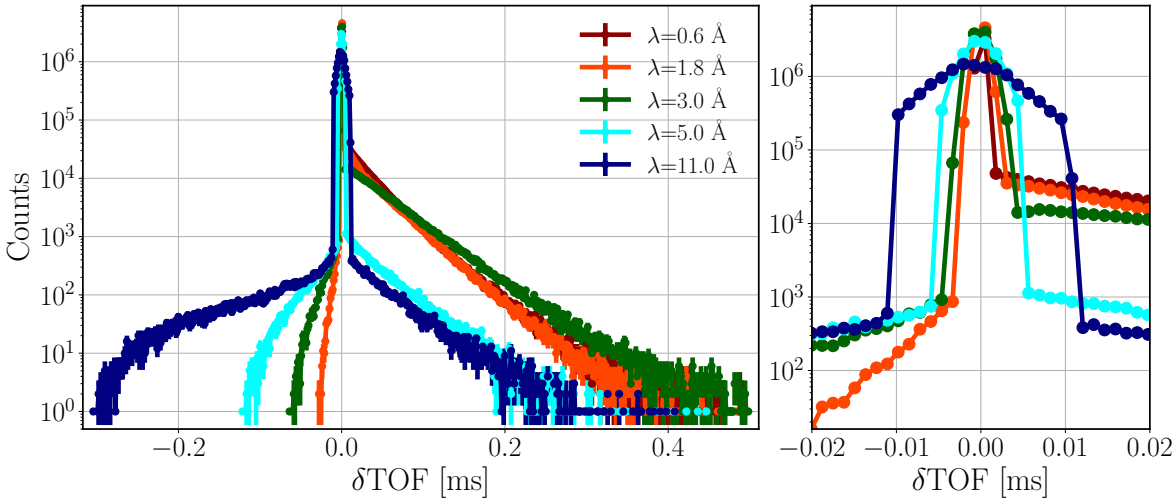

Figure 5.11: δToF for different neutron wavelengths. The limits are wavelength dependent and not shown. The figure on the right shows an enlarged view of the centre part of the figure on the left. The lines are only joining the points.

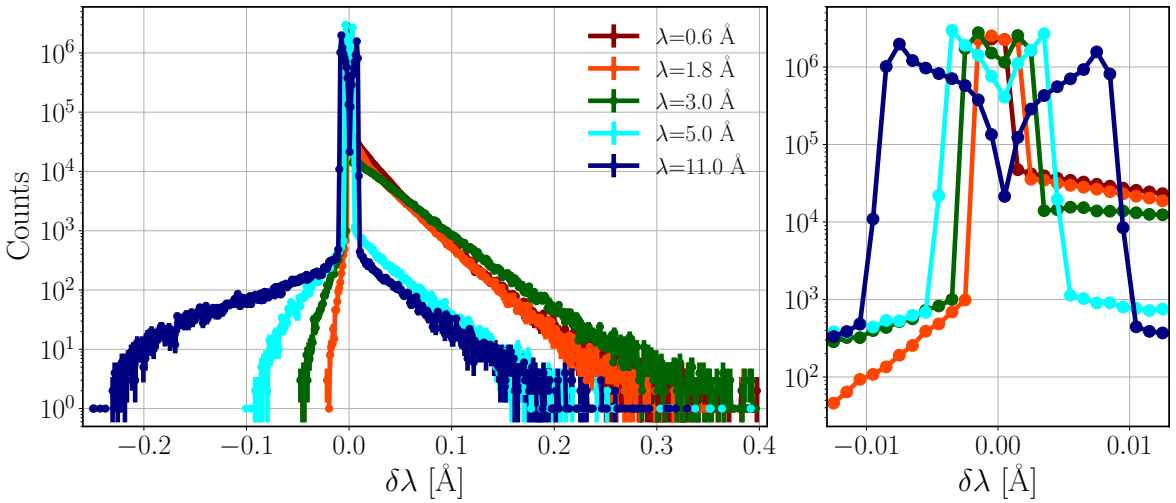

Figure 5.12: $\delta\lambda$ for different neutron wavelengths. The limits are strongly wavelength dependent and not shown. The figure on the right shows an enlarged view of the centre part of the figure on the left. The lines are only joining the points.

visible. Simulations with low λ values give higher scattered background and broader signal peaks.

5.2.4 Fractional scattering

Signal and background relation can be characterised by several quantities. A common way to express it in neutron scattering is the peak-to-tail ratio, that can be visually extracted from the presented figures. However, this ratio does not quantitatively reflect the total amount of signal or background and in addition it is sensitive to the histogram

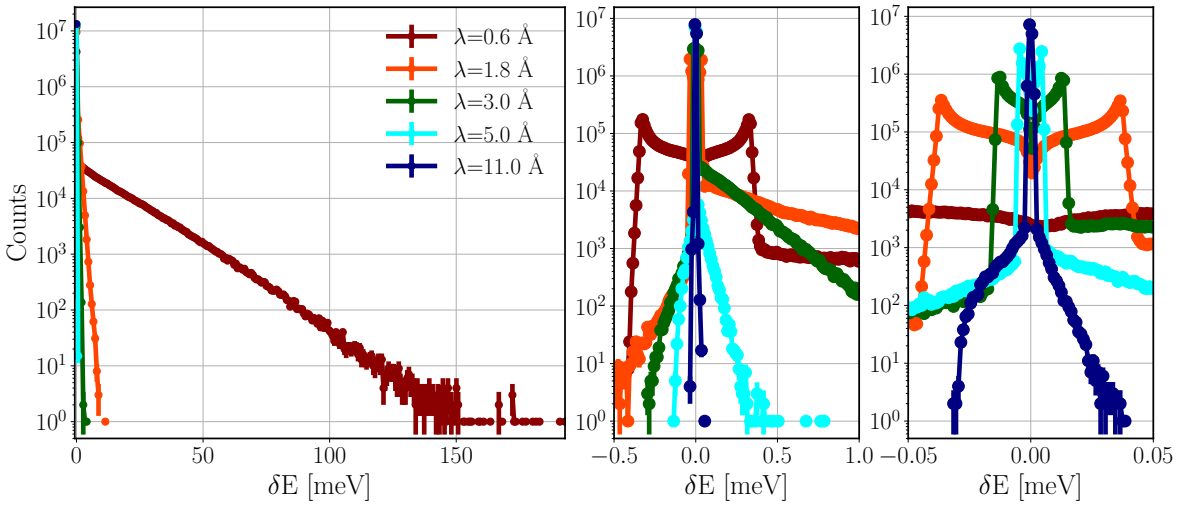

Figure 5.13: Change in measured neutron energy for different initial wavelengths. The three figures emphasise different ranges, with different binning. The lines are only joining the points.

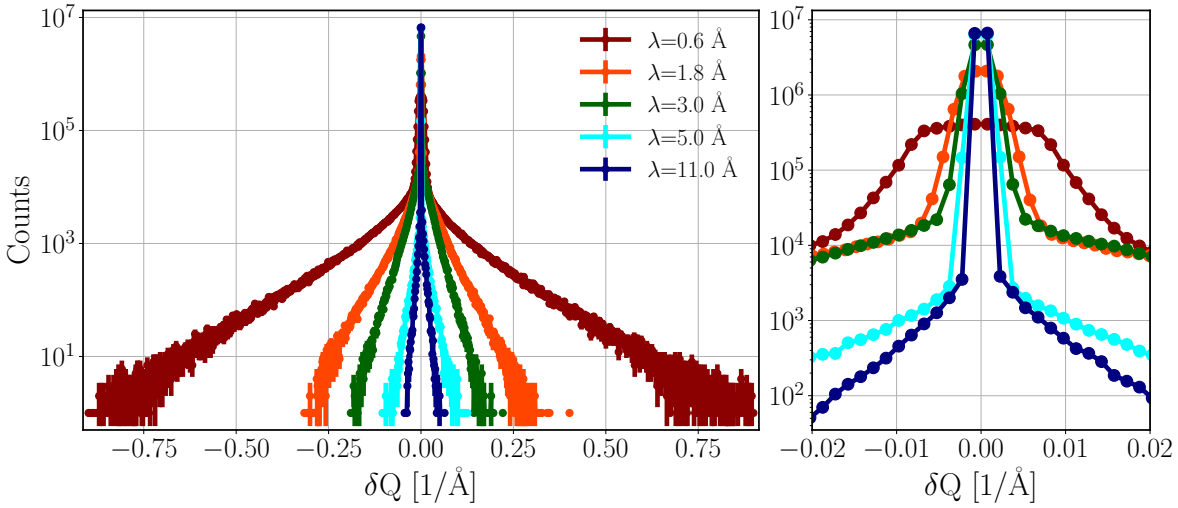

Figure 5.14: δQ for different neutron wavelengths. The limits are wavelength dependent and not shown. The figure on the right shows an enlarged view of the centre part of the figure on the left. The lines are only joining the points.

binning. Instead, a different figure of merit is used that provides fractional scattering in terms of integrals, as defined by Equation 5.4:

$$\text{Fractional Scattering} = \frac{B}{S+B} \tag{5.4}$$

where S and B denote the number of detected neutrons considered as signal and background respectively. Although the shape of signal and background varies for the observed δ quantities, Figure 5.15 demonstrates that the integrals of the previously defined signal ranges are similar within less than a 3% range. This means that any of the δ quantities and the signal limits thereof lead to essentially the same fractional

scattering values. The following results are acquired using $\delta\Theta$ for signal-background separation.

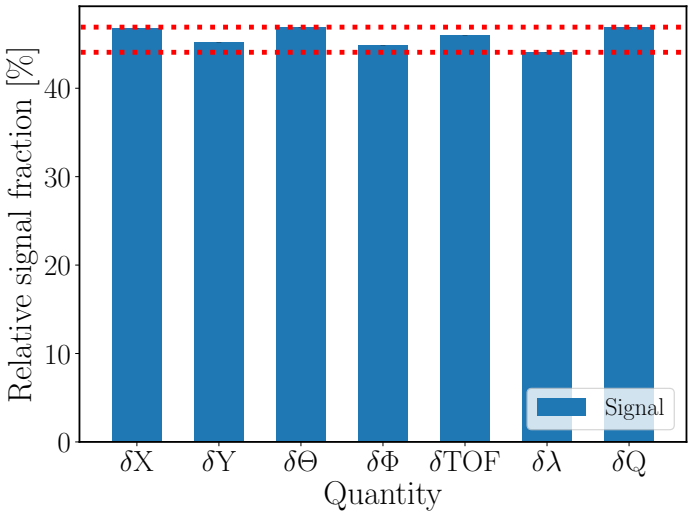

Figure 5.15: The portion of neutrons considered as signal of the total number of neutrons, based on the limits for different δ quantities from simulation with 1.8 Å neutrons. The dotted lines in red indicate the minimum and maximum value.

Figure 5.16 depicts the fractional scattering for 3 wavelengths for a different number of panels, as the latter are added one-by-one to the geometry. It was shown before that additional panels not only increase the signal, but the scattered background as well as, via the detection of more scattered neutrons and the back-scattering of neutrons to upstream panels. This result shows that the ratio of signal-to-background degrades with the additional panels, because the fractional scattering increases monotonously. This is more notable for low wavelengths, where the differences are higher, but the tendency is the same for 11.0 Å. For the same number of panels, fractional scattering is always higher for neutrons with shorter initial λ.

Figure 5.17 demonstrates the fractional scattering for different wavelengths with 5 panels of detectors, using the 4 models with reduced materials, mentioned earlier in this section. Additional materials increase the fractional scattering for all λ and in agreement with previous results, aluminium has a higher impact on scattering than copper, which manifests itself in higher fractional scattering values too. It can be seen that scattering is a very important background effect to be minimized below the Bragg cut-off. Figure 5.18 presents similar information to Figure 4.6 with two changes. First, the absorption in different materials is merged in a single color (purple). Second, the detection is separated into signal and background using $\delta\Theta$ limits once again.

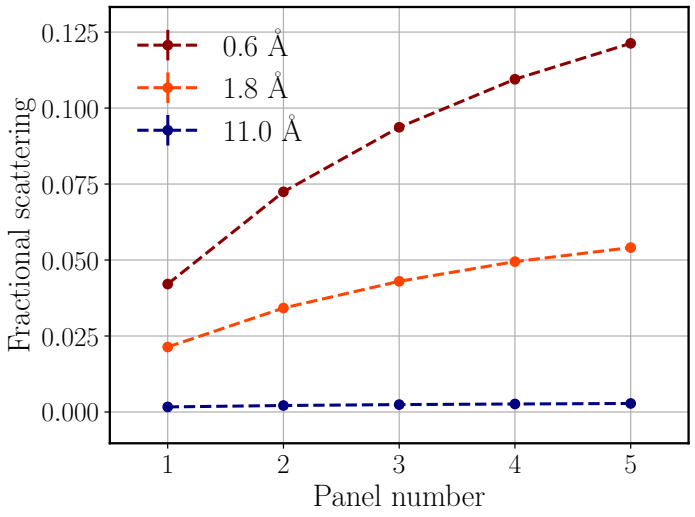

Figure 5.16: The change of the fractional scattering for different number of detector panels with different neutron wavelengths.

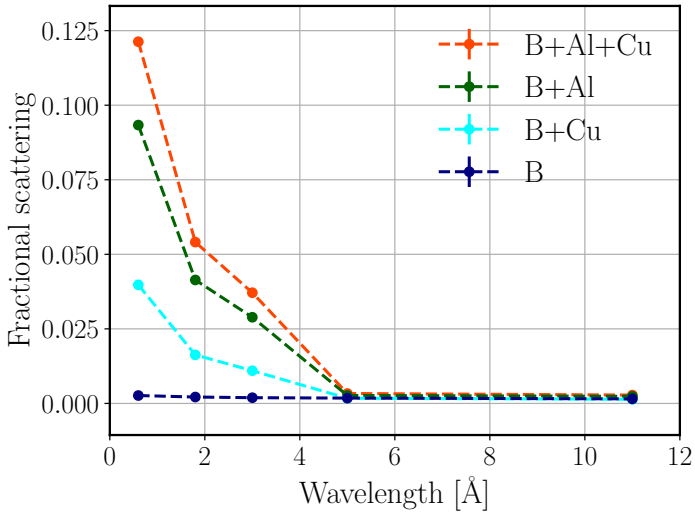

Figure 5.17: The effect of the detector material components on the fractional scattering based on $\delta\theta$ for different neutron wavelengths between 0.6–11 Å. 'B' (dark blue) represents the geometry where only gas and converter are in place. 'B+Cu' (cyan) has enabled copper in the straw volumes. 'B+Al' (green) has enabled aluminium in the tube volumes. Finally 'B+Al+Cu' (orange) has all materials in place.

5.3 Polyethylene "afterburner" block behind the detector

As previously demonstrated, for short wavelengths such as 0.6–1.8 Å respectively 60–27% of the neutrons can escape even 5 panels of detectors without being absorbed in any of the materials. The detector performance could be possibly improved by

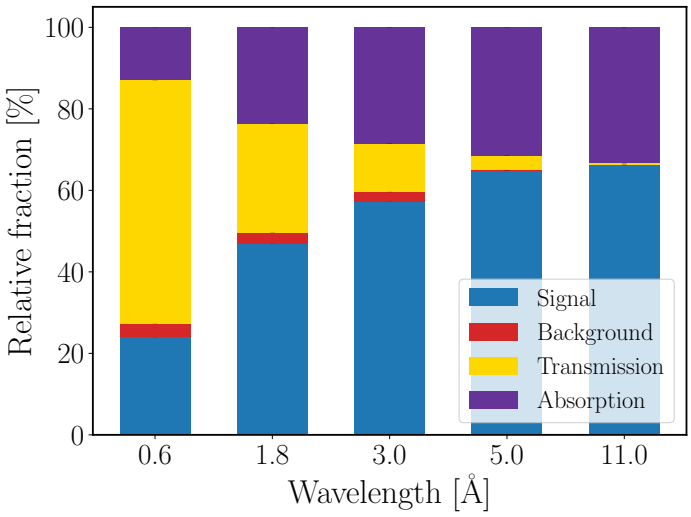

Figure 5.18: Proportion of absorption, transmission and detection with the separation of signal and background from simulations with monoenergetic neutrons.

applying additional panels of detectors but that might not be the most cost-efficient solution, taking into account that there is little to gain for longer wavelengths. However, there is a cheap and easy option to increase detection efficiency by placing a strongly scattering material at the backside of the detectors [104]. The principle is to back-scatter any transmitted neutron forcing it to enter the detectors again, giving it a further opportunity for conversion and detection. In the study cited above it was shown that the detection efficiencies can be enhanced by applying a single layer of polyethylene (PE) behind the detectors. It is emphasised, however, that as a side effect the scattering in the back-scatterer layer has a negative impact on the resolution of the detector so the combined effect should be carefully examined.

The definition of signal and background from the previous section offers a practical way to decide whether this technique is advantageous or not for the BCS detector. To investigate this, a PE layer is placed closely behind the fifth panel of detectors as illustrated in Figure 5.19. The Geant4 physics list used for these simulation is ESS_QGSP_BIC_HP_TS [104].

The highest gain from the back-scattering of transmitted neutrons is achieved for low wavelengths. Figure 5.20 demonstrates the impact of the additional PE layer on $\delta\Theta$ for the lowest observed wavelength, λ=0.6 Å. This result shows a significantly increased background with a slightly increased signal.

Figure 5.21 demonstrates that the PE layer has a different effect on the different δ quantities. The signal defined by the limits for $\delta\Theta$ is 6.3% higher than for $\delta\lambda$. This

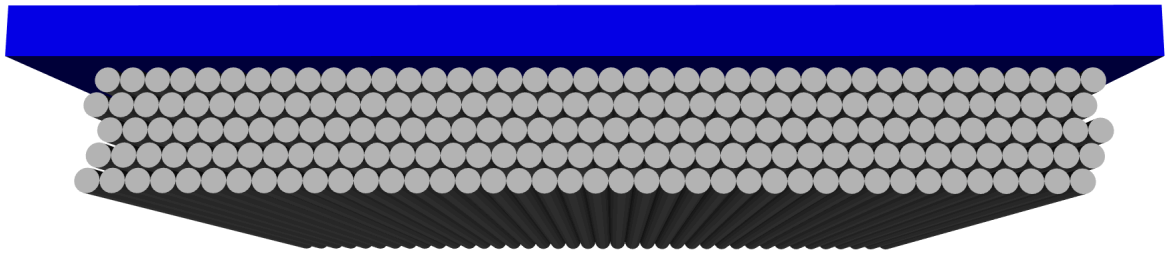

Figure 5.19: A layer of PE (blue) is placed behind the 5 panels of BCS detector tubes (silver). The thickness of the PE layer is 50 mm.

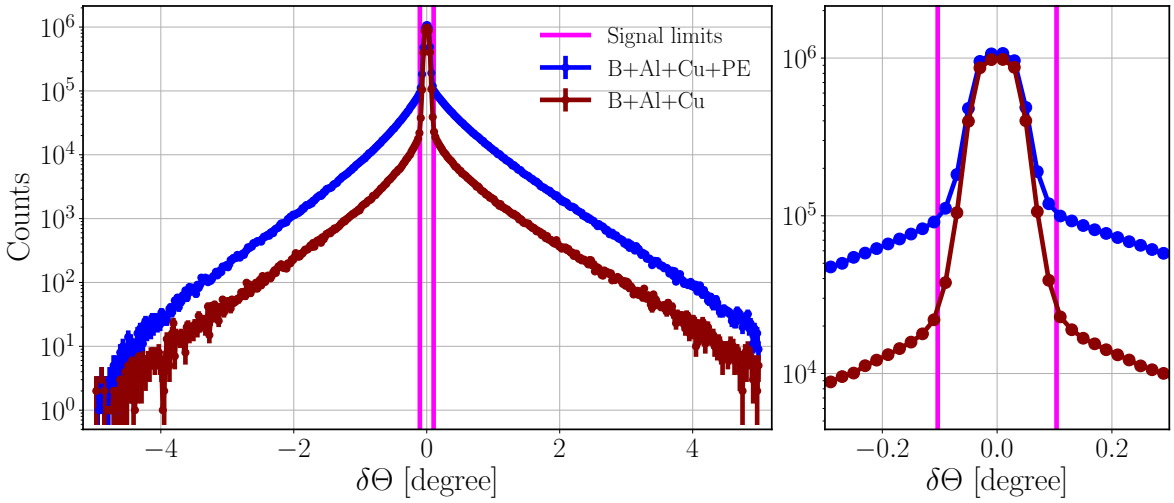

Figure 5.20: $\delta\Theta$ with and without the PE layer from simulations with λ=0.6 Å. The signal limits are the same as defined in the previous section. The figure on the right shows an enlarged view of the centre part of the figure on the left. The lines are only joining the points.

difference is more than double of any previously experienced. This implies that the fractional scattering depends much more on the signal definition.

The focus here is on the case with the highest gain, so the fractional scattering results presented in Figure 5.21 are calculated with the highest signal from $\delta\Theta$. Even with this favourable definition, the ratio of the scattered background appears to be higher with the back-scattering layer than without it. For the highest wavelength there is no difference but going to lower λ where the PE should help, the fractional scattering becomes significantly worse.

This is in agreement with what can be derived from Figure 5.22 showing the effects of PE from various aspects. For higher wavelengths, where the transmission is negligible, there is practically no change but for lower wavelengths the significant drop in the transmission leads to increase in all other areas. Due to the longer path length in copper and aluminium there is more absorption in these materials, nevertheless it remains a minor effect. The vast majority of the back-scattered and not transmitted

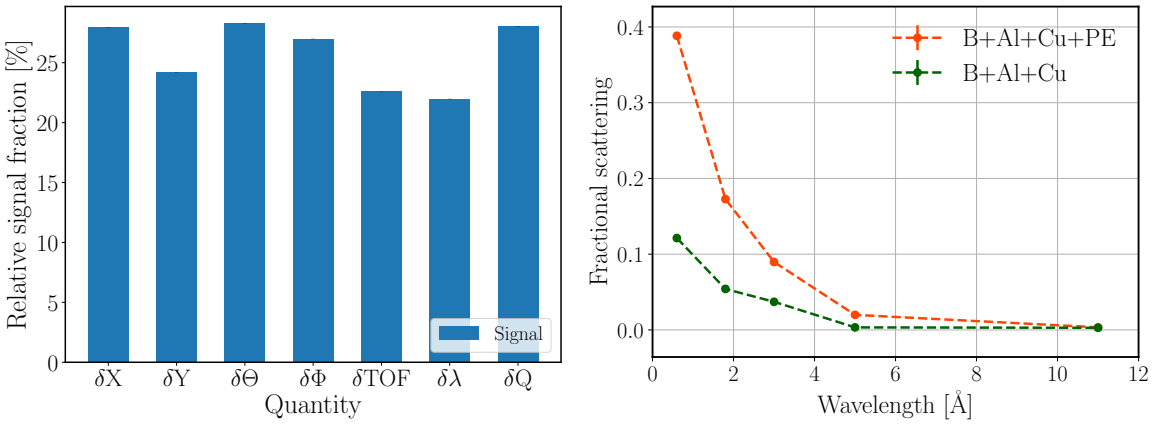

Figure 5.21: The portion of neutrons considered as signal of the total number of neutrons based on the limits for different δ quantities from simulation with λ=0.6 Å (left) and the fractional scattering using signal from $\delta\Theta$ for different wavelengths (right).

neutrons are absorbed in the converter layer with the usual detected/not detected ratio. This means that the detection efficiency is effectively enhanced by the PE layer. On the other hand the separation of detection events into signal and background shows that the additionally detected neutrons mostly increase the background, not the signal. Where most gain is expected, for λ=0.6 Å, the 4.3% increase in the ratio of the signal is followed by a 14.6% increase in the background. This implies that the only application where a PE afterburner may be beneficial is homeland security, where position resolution is not a concern. These results re-emphasise that it is vital to ensure that whilst polyethylene or other hydrogen containing materials are ubiquitous in neutron shielding, next to the detector, the shielding material must have no albedo effect from scattering of thermal neutrons.

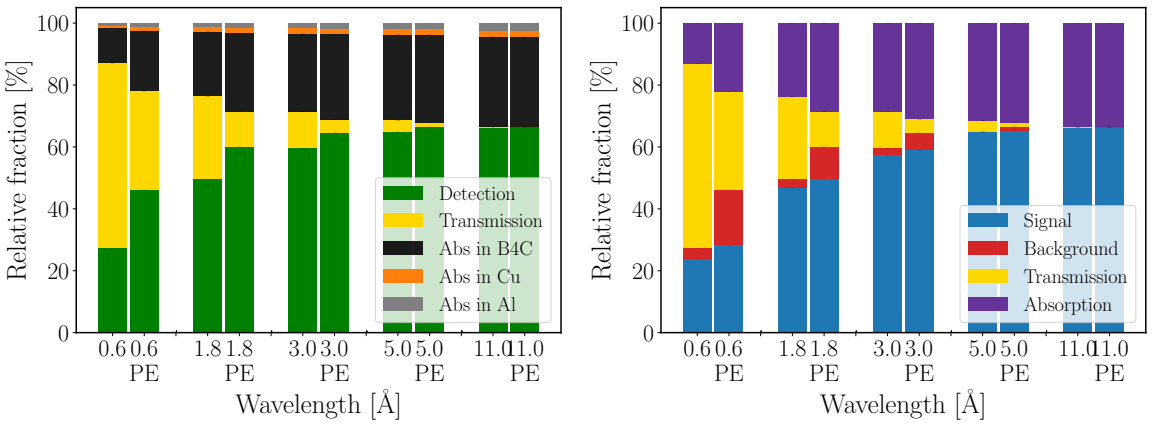

Figure 5.22: Comparison of proportion of absorption, transmission and detection with and without the PE layer from simulations with monoenergetic neutrons. On the left the absorption is separated for different materials, on the right the detection is separated into signal and background.

Chapter 6

Full simulation of BIFROST from source to detectors

In order to study a neutron scattering instrument ahead of being built, a full simulation model can be implemented and used in various representative cases. Building a reliable simulation model and implementing data analysis tools are key parts in this process. Each part of the model has to be detailed and precise enough to allow investigation of different properties, but focused and simplified to facilitate identification and decoupling of cumulative effects. The work introduced in this section aims at extending the pre-existing model of the BIFROST instrument to carry out full simulation of the instrument from to the neutron source to the detectors, and to develop a methodology to acquire time-averaged and peak incident detector rates for this instrument.

As mentioned in Section 2.5, the simulation of the BIFROST instrument is divided into two parts. First, the simulation of the 162 m long beam transport and conditioning system until the end of the last guide section is done using the McStas model of the instrument introduced in Section 2.1.2. Then, the simulation of the sample and scattering characterisation system is carried out using the Geant4 model implemented for this study, containing all nine Q-channels and 5 energy channels in each. The transition between the two simulations is facilitated by the MCPL tool.

In the following sections first the Geant4 simulation model of scattering characterisation system implemented for this study is introduced, then full simulation of the BIFROST instrument is demonstrated using a standard calibration sample, presenting the acquired time-averaged and peak incident detector rates.

6.1 Geant4 model of the scattering characterisation system

The Geant4 simulation model of the sample and scattering characterisation system, depicted in Figure 6.1a, contains a crystalline sample, a single Q-channel including all five analyser arcs, and empty volumes at several places to monitor ToF, energy and position distribution of neutrons, in order to examine the change of the neutron beam.

For both the crystalline sample and analysers, NCrystal materials are used. The analyser arcs consist of 7–9 blades using the pyrolytic graphite material with the layered crystal model, described in more detail in Section 2.3. The correct position and tilt angle of the blades is crucial for the instrument. The blades are modelled as rectangular boxes with the crystal planes oriented along the axes to have Bragg-scattering condition (see Equation 1.4) on the (h,k,l) = (0,0,2) plane for neutrons with energies 2.7 meV, 3.2 meV, 3.8 meV, 4.4 meV and 5.0 meV for the respective analyser arcs, and scatter them to the corresponding detectors.

Simulation of the detection process is out of scope for this work, therefore the detector triplets are not explicitly included in the model. They are instead replaced with empty volumes with dimensions exceeding that of the tubes. During the analysis neutrons entering these – occasionally overlapping – volumes are tested against certain conditions to select neutrons which would hit the real detectors.

As demonstrated in Figure 6.1b, all 9 Q-channels are implemented in the model, in accordance with the "triple stagger" geometry described in Section 1.3. There is, however an option (parameter) to use only a single Q-channel to reduce simulation time in studies where effects are localised inside one channel.

The sample–analyser distances in all Q-channels of the model correspond to the real geometrical parameters. The analyser–detector distances, however, are the same as the sample–analyser distances in all Q-channels, meaning that the slight asymmetry of the non-symmetrical Q-channels described in Section 1.3 are neglected. This is a less than 7.5% difference in the analyser–detector distances, that do not affects simulations where a single symmetrical Q-channel is modelled.

The simulation model does not contain the sample environment, the filtering system and cross-talk shielding. Although the cross-talk shielding between energy- and Q-channels is not explicitly included in current version the model, it is mimicked by certain conditions applied at the data analysis level. This means that neutrons cannot skip parts of the model, and they can reach a particular detector tube only by scattering

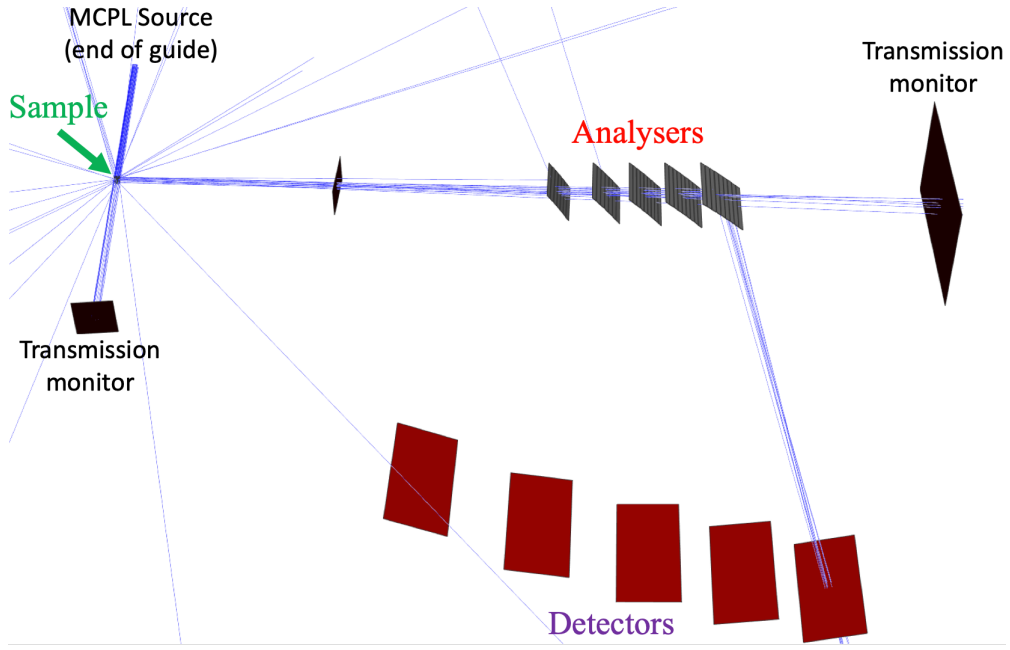

(a)

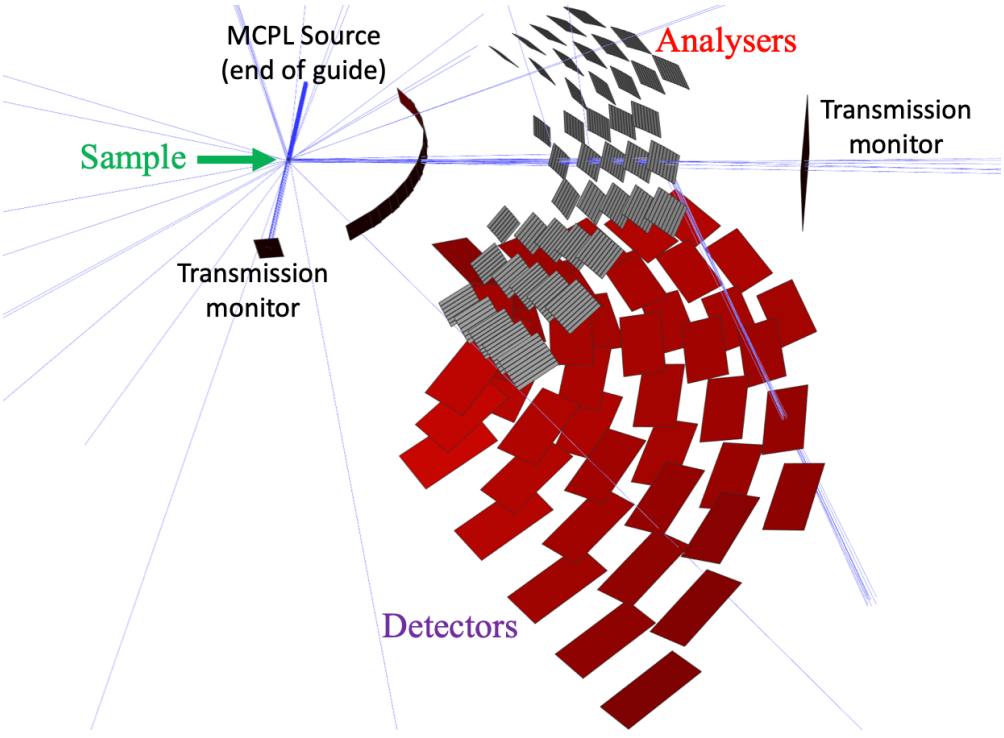

(b)

Figure 6.1: Geant4 model of the sample and scattering characterisation system including one Q-channel (a) or all Q-channels (b). The blue lines indicate simulated neutron paths.

in one of the corresponding analyser blades. This is practically equivalent to an ideal cross-talk shielding absorbing all stray neutrons.

The case is similar for the filtering system, that is also replaced by a condition in the data analysis after the simulation. All neutrons with an energy higher than 7 meV are

excluded when they pass through the "monitoring" empty volume between the sample and the first set of analysers. As mentioned is Section 1.3, the transmission of beryllium drops sharply around 5 meV, that is in fact the highest of the five final energies selected by the analysers. Simulation of effects of this transition in the transmission is out of the scope, and using ideal transmission in the 0–7 meV energy region keeps the rate estimates conservative. The absence of the radial collimator of the filtering system or any substitutional condition on the divergence is also part of the conservative approach.

The Geant4 physics list used is QGSP_BIC_HP_EMZ that uses high precision models and cross-sections for neutron energies lower than 20 MeV, and allows the correct treatment of thermal and cold neutrons when combined with NCrystal.

6.2 Simulation with calibration sample

In order to demonstrate the use of the full simulation model of BIFROST and also to validate it, simulation with a common calibration sample is carried out.

The McStas (v. 2.5) simulation of the first part of the instrument until the end of the last guide section is done with parameters that results in the highest incident rate on the sample. This means accelerator source power of 5 MW and pulse-shaping chopper opening time of 5 ms, that technically results in fully open pulse-shaping chopper. The lowest energy in the selected wavelength band is set to 2.7 meV. The MCPL file produced with this simulation is then used as a neutron source for the Geant4 simulation of the sample and the scattering characterisation system including all nine Q-channels.

The sample selected for this simulation is vanadium, that is assumed to be an incoherent elastic scatterer which scatters isotropically and therefore it is used to calibrate the incident neutron intensity and the detector efficiencies in neutron spectrometers [105]. The instrument is designed to facilitate measurements on small samples, but dimensions up to 1.5 cm are possible, therefore a solid (not hollow) cylindrical sample with the diameter and height of 1.5 cm is used to increase rates and by that promote better statistics. The rotation of the nine Q-channels is arbitrarily selected in a way to have $2\Theta = 90°$ scattering angle for the central Q-channel, as depicted in Figure 6.2.

The time-averaged energy spectra of the neutron beam at the sample and different positions of the central Q-channel are demonstrated in Figure 6.3. The time-averaged neutron intensities acquired by the integration of these energy spectra are presented in Table 6.1.

The transmission through the sample is only 23% with no peaks missing from the

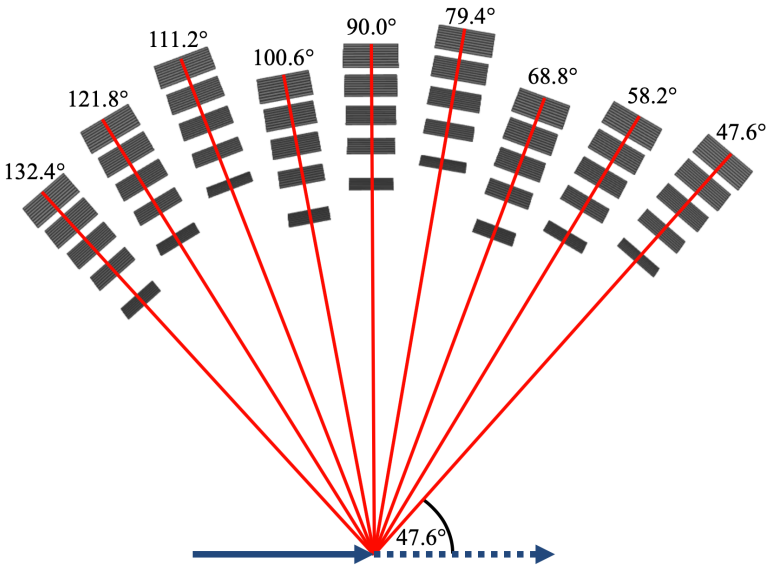

Figure 6.2: Top view schematic figure of the scattering characterisation system model with all nine Q-channels. The red lines and corresponding angles indicate the scattering angle for the centre of each Q-channel.

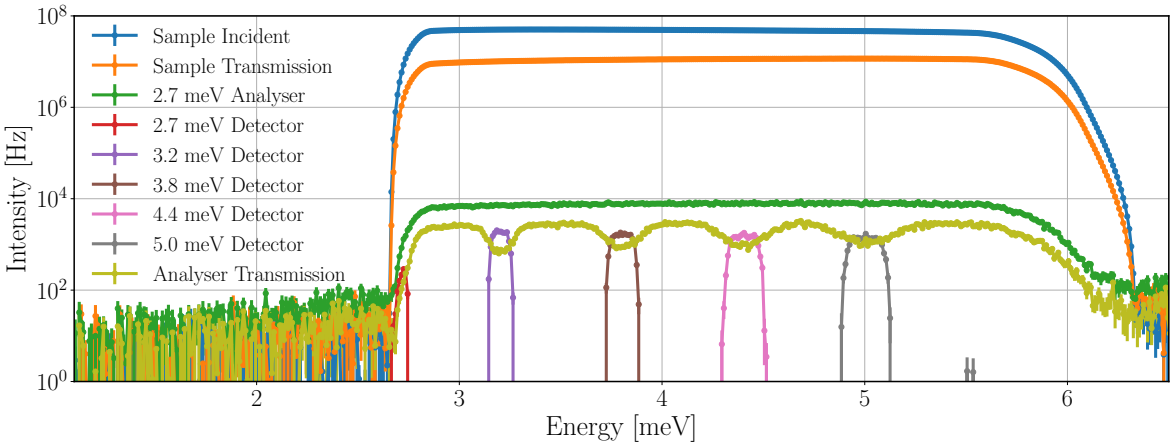

Figure 6.3: Time-averaged neutron energy spectra at the sample and in the central Q-channel with a vanadium sample in Geant4 simulation. Incident beam on sample (in blue), beam transmitted through the sample (in orange), beam on the set of analysers for 2.7 meV neutrons (in green), neutrons hitting the detector triplets for energies 2.7–5.0 meV (in red–grey), beam transmitted through all sets of analysers (in mustard). The lines are only joining the points.

spectrum, as expected from a large sample scattering mainly incoherently. The wide spectrum of the 2.7 meV analysers shows that the neutrons of the full energy range of the incident neutrons on the sample are scattered toward the central Q-channel mostly elastically but signs of inelastic scattering appear on both ends of the spectrum. Despite the wider energy range, a logarithmic scale is needed as the integrated intensity is more than 3 orders of magnitude lower than that of the sample.

The spectrum of the beam transmitted through all five analyser arcs, that also

Position	Intensity [Hz]
Sample Incident	$1.45{\cdot}10^{10}$
Sample Transmission	$3.36{\cdot}10^{9}$
2.7 meV Analyser	$2.55{\cdot}10^{6}$
2.7 meV Detector	$1.6{\pm}0.3{\cdot}10^{3}$
3.2 meV Detector	$1.7{\pm}0.1{\cdot}10^{4}$
3.8 meV Detector	$2.1{\pm}0.1{\cdot}10^{4}$
4.4 meV Detector	$2.4{\pm}0.1{\cdot}10^{4}$
5.0 meV Detector	$2.6{\pm}0.2{\cdot}10^{4}$
Analyser Transmission	$7.20{\cdot}10^{5}$

Table 6.1: Time-averaged neutron intensities at the sample and in the central Q-channel with a vanadium sample in Geant4 simulation.

includes neutrons that avoid the analysers, clearly shows neutrons missing because they are selected by the analysers. These neutrons appear in the spectra of the detectors, that also show that peaks are narrower for lower energies as a result of the better energy resolution of the analysers for lower energies. The incident intensity on the 2.7 meV detectors is much lower than in other detectors due the energy range selected by the bandwidth chopper. The resulting time-averaged incident rates are higher for higher energies, with the maximum of 26±2 kHz for the 5.0 meV detector triplet.

The time-averaged incident neutron rates of all detector triplets in all Q-channels are presented in Table 6.2. The trends in the results demonstrate the combination of

Q-channel	Scattering angle [°]	2.7 meV [kHz]	3.2 meV [kHz]	3.8 meV [kHz]	4.4 meV [kHz]	5.0 meV [kHz]
1	132.4	2.8±0.3	23±1	28±1	30±2	31±2
2	121.8	2.2±0.3	20±1	23±1	27±2	30±2
3	111.2	1.9±0.3	18±1	21±1	24±1	25±1
4	100.6	2.3±0.3	21±1	25±1	28±2	30±2
5	90.0	1.6±0.3	17±1	21±1	24±1	26±2
6	79.4	1.4±0.2	15±1	18±1	21±1	22±2
7	68.8	2.0±0.2	18±1	22±1	25±2	26±1
8	58.2	1.4±0.2	15±1	19±1	22±1	23±1
9	47.6	1.1±0.2	13±1	16±1	19±1	21±1

Table 6.2: Time-averaged neutron intensities of the five detector triplets in all nine Q-channels with a vanadium sample.

three effects. In each Q-channel the detector triplets for higher energies experience higher incident rates due to the wider energy ranges selected by the analysers, as shown for the central Q-channel in Figure 6.3. The second effect has roots in the "triple stagger" geometry and the asymmetry of the Q-channels. The sample–analyser distances in Q-channels 1, 4, 7 are shorter, and in channels 3, 6, 9 are longer than distances in channels 2, 5, 8. The shorter distances increase the rates visibly because neutrons are not collimated and therefore their spread at longer distances becomes important. This effect on the rates is somewhat blurred by the third effect caused by the anisotropy of the scattered neutron intensity from a vanadium sample. For the observed energies the scattering cross-section of vanadium is slightly higher for higher scattering angles [106], and more importantly, the neutron path length through the solid cylindrical sample is generally higher for neutrons scattered in lower angles, therefore the absorption is higher for these neutrons. These two effects result in generally higher rates for Q-channels positioned for higher scattering angles, but due to the asymmetry of the adjacent Q-channels, it is most apparent when comparing Q-channels of the same symmetry, like 2, 5, 8.

As mentioned in Section 1.3, the analysers scatter neutrons with slightly different energies in different directions, in accordance with the Bragg-condition in Equation 1.4. As a result of this vertical spread, the three detectors of the triplet record slightly different regions of energy, in accordance with the prismatic analyser concept, as demonstrated in Figure 6.4.

For all triplets the energy ranges of the detector tubes are in accordance with the expected values based on the BIFROST instrument design. The spectrum of all triplets – except the one for 2.7 meV – shows that the intensity is similar in all three tubes, that justifies the instrument design choice of 60 arcmin analyser mosaicity. The increasing intensity in the tubes of the 2.7 meV detector triplet is the result of the energy range selected by the bandwidth chopper.

Using the energy spectrum in Figure 6.4 the simulated energy resolution of the secondary spectrometer is derived by fitting Gaussian function to the peaks and defining the resolution as the full width at half maximum (FWHM). The same is done for the spectrum of the detector triplets to acquire the energy resolution of the triplets. The results are presented in Table 6.3 side-by-side with the reference values from the preliminary design [107].

The simulated and reference values show good agreement. The simulated results are generally slightly higher for both the tubes and the detector triples, as expected due to the higher sample size and detector tube spacing. The larger sample increases

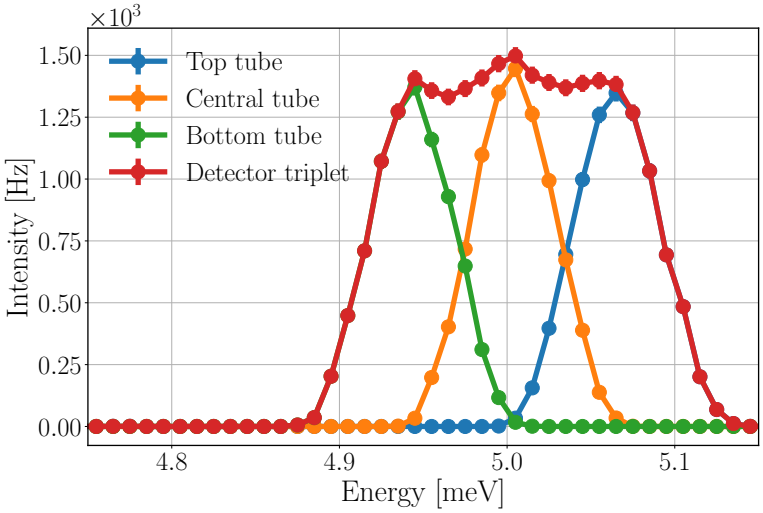

(a) 5.0 meV detector triplet.

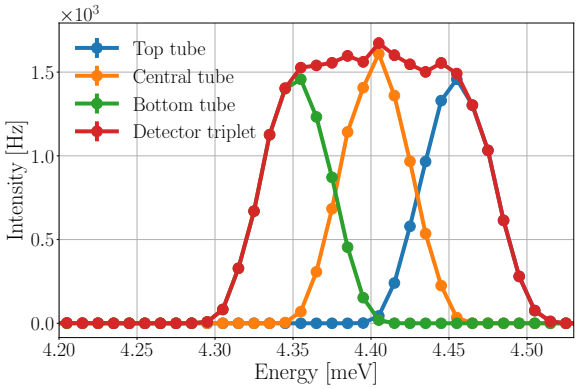

(b) 4.4 meV detector triplet.

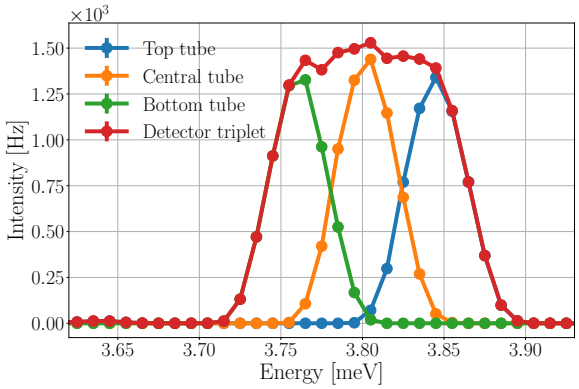

(c) 3.8 meV detector triplet.

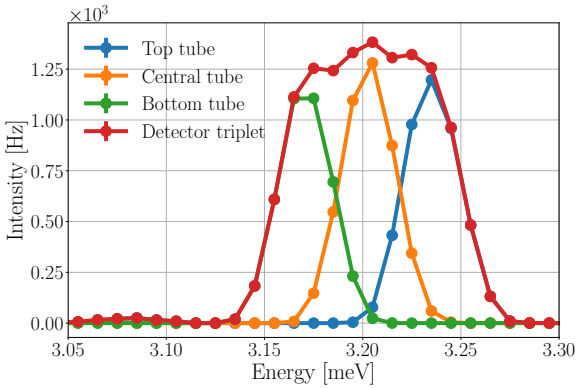

(d) 3.2 meV detector triplet.

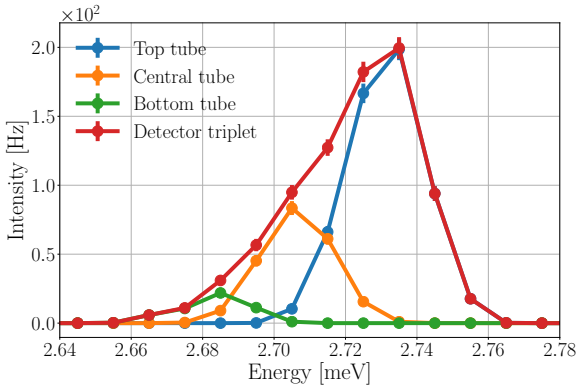

(e) 2.7 meV detector triplet.

Figure 6.4: Energy spectrum of neutrons at all five detector triplets, with vanadium sample. The lines are only joining the points.

the resolution of each tube, as the mosaicity of the analysers allows neutron to be selected from a wider angle range. The higher distance between the tubes increases the resolution of the triplets, by widening the energy range accepted by the triplet, as the tubes on the sides probes energies more distant from the central energy. For the

Energy [meV]	Simulated ΔE tube [μeV]	Reference ΔE tube [μeV]	Simulated ΔE triplet [μeV]	Reference ΔE triplet [μeV]
5.0	58±1	57–58	154±1	154–155
4.4	50±1	48–49	129±1	130–131
3.8	41±1	39–40	106±1	105–106
3.2	32±1	30	81±1	80
2.7	24±2	22.5-23	–	59.7–60.3

Table 6.3: Simulated and reference energy resolution (ΔE) of single detector tubes and detector triplets for all energies. The reference values correspond to 5 mm sample height and 0.2 mm detector tube spacing. The simulation values correspond to 15 mm sample height and 2.3 mm detector tube spacing.

2.7 meV triplet the simulated resolution is not acquired due to the uneven incident spectra.

Given that BIFROST is a ToF instrument at a spallation neutron source, the incident detector rate naturally has a pulsed time structure. The ToF distribution of a single pulse on the 5 meV detectors is depicted in Figure 6.5.

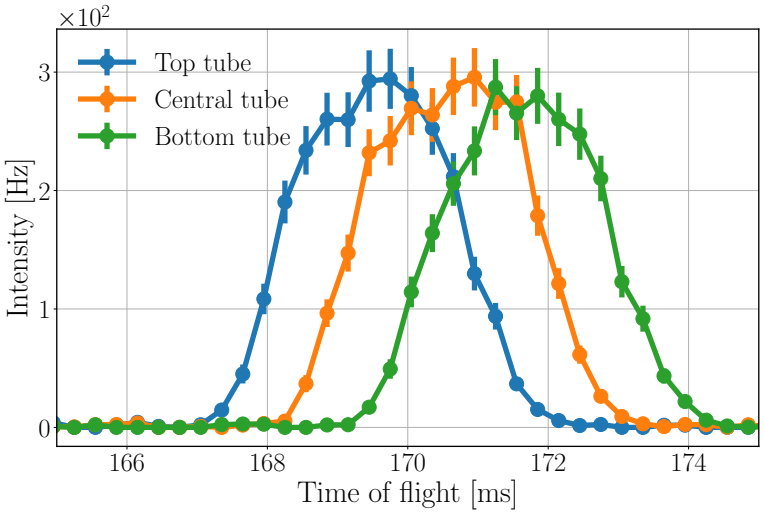

Figure 6.5: ToF spectrum of neutrons at the 5 meV detector triplet, with vanadium sample. The lines are only joining the points.

By taking into account only those neutrons which arrive to the detectors at the peak of their ToF distribution in a short time range of 0.3 ms, peak incident rates can be derived. Due to the distinct energy range and therefore different ToF spectra of the tubes, the highest peak incident rate occurs at different times for each tube of a triplet. For a single detector tube the highest incident rates are found for the central 5.0 meV detector with a time-averaged of 9±1 kHz and peak intensity of 0.21±0.02 MHz.

Chapter 7

Incident detector rates for coherent elastic peak at BIFROST

Determination of anticipated detector rates for an instrument is a key part of defining requirements for the detectors to be used. It can prevent the detector rate capability from becoming the bottleneck of experiments or a source of performance degradation. This is particularly the case for BIFROST where the scattering characterisation system is designed to detect weak inelastic signals from small samples, but the exceptionally high intensity on the sample carries the danger of extreme rates in case of coherent elastic (Bragg) peaks. For this reason, simulations are performed to determine the highest time-averaged and peak incident rates for the detector tubes.

To acquire the highest possible detector rates, the simulation tools and methods described and used in Chapter 6 are used with the worst-case instrument configurations and samples. To cross-validate the results, a McStas model of a single Q-channel is implemented. This model is used with the same configurations and samples as the Geant4 model. The results are compared as well as the two simulations tools.

In the following section first the worst-case instrument and sample configurations are considered, then the McStas model of the BIFROST scattering characterisation system introduced. After that, the results of simulations with two different single crystal samples are presented in the last two sections.

7.1 Considerations of worst-case conditions

The worst-case incident rate for a single detector tube occurs when a strong Bragg peak from a single crystal sample gets reflected to it. To get such elastic scattering on the sample, Bragg's law (see Equation 1.4) must apply. To get neutrons scattered on the sample onto the detectors, their energy has to match one of the energies selected by the analyser arcs. Based on the ESS source neutron energy spectra, the guide transmission and the energy resolution of the analysers, the highest incident rates are expected for the 5.0 meV (4.045 Å) detector triplet, as it is demonstrated in Section 6.2. This sets the requirement of the lattice parameter being larger than 4.045/2 Å, according to Equation 7.1, derived from Equation 1.4.

$$d_{hkl} \geq \frac{\lambda}{2}. \tag{7.1}$$

Any single crystal with lattice parameter larger than 4.045/2 Å could be used to Bragg scatter neutrons with 5.0 meV energy in scattering angle (2Θ) defined by the Bragg's law. Technically BIFROST has a 2Θ coverage of 90° (in two tank settings) but only in the 2Θ range of 7°–135°, so the lattice parameter has to be large enough (33.13 Å and 2.19 Å respectively for 2Θ=7° and 2Θ=135°) to have scattering angle in that region.

To get the strongest Bragg peak from a single crystal, the material of the analysers, pyrolytic graphite has to be used that fulfils these criteria with d_{002}=3.3555 Å lattice parameter and the corresponding 2Θ=74.134° scattering angle. That would be the truly worst-case sample, but to get results from a less unrealistic sample with large enough lattice parameter and strong Bragg peak, simulations are also done using an yttrium oxide (Y_2O_3) single crystal with lattice parameter of d_{2-2-2}=3.0724 Å and corresponding scattering angle of $2\Theta = 82.338°$.

Further sample parameters that potentially influence the rates are the sizes and mosaicity. The instrument is designed to facilitate measurements on small samples, but dimensions up to 1.5 cm are possible, therefore cylindrical samples with the diameter and height of 1.5 cm are used in the simulations. The sample mosaicity resulting in the highest rate can depend on the divergence of the incident beam on the sample, however, as a rule of thumb the highest rates are expected when the mosaicity of the sample matches that of the analysers, so the sample mosaicity is set to 60 arcmin. It is shown later in Section 8.1 that this is a good assumption, and within the 60±20 arcmin sample mosaicity range it has a less than a 10% effect on the incident detector rates.

Regarding the instrument settings, the aim is to have the highest possible rate of

neutrons with the chosen energy on the sample. This is achieved with the maximum accelerator source power of 5 MW and fully open pulse-shaping chopper setting with opening time of 5 ms. The lowest energy in the selected wavelength band is set to 2.7 meV that guarantees to have 5.0 meV neutrons in the range.

Study of the effect of sample mosaicity, sample size, and pulse-shaping chopper opening time on the incident detector rates that justifies the chosen parameters is presented in Chapter 8.

In order to realise the simulations in both Geant4 and McStas, the samples are oriented to fulfil the Bragg law criteria for the incoming 5 meV neutrons on the selected scattering planes, and the single Q-channel modelled is rotated according to the resulting scattering angle. In BIFROST the whole scattering characterisation system can be rotated around the sample, so having a Bragg peak from the sample in the exact direction of a single Q-channel is perfectly realistic.

The simulations with the parameters described above is done in two steps. First, the neutron transport from the source to the end of the beam transport and conditioning system is done with the McStas model introduced in Section 2.1.2, saving neutron data at the end in an MCPL file. This file is then used as the source term for the simulation of the sample and scattering characterisation system, with both the Geant4 model from Section 6.1 and the McStas model introduced in the next section. McStas version 2.5 is used for the simulations.

7.2 McStas model of the scattering characterisation system

The McStas model of the sample and scattering characterisation system, depicted in Figure 7.1, is essentially identical to the Geant4 model with a single Q-channel option, containing a crystalline sample, one Q-channel including all five analyser arcs, and McStas monitor components at several places probing ToF, energy and position distribution of neutrons, in order to examine the change of the neutron beam. The analyser arcs consist of 7–9 blades using the "NCrystal_sample" component with pyrolytic graphite material, described in more detail in Section 2.3. NCrystal is also used for all crystalline samples throughout this study. The simulation model does not contain the sample environment, eight out of the nine Q-channels, the filtering system, cross-talk shielding and the detectors.

Using a reduced geometry and excluding any model of the sample environment is intentional, aiming to get a conservative estimate in terms of the highest detector

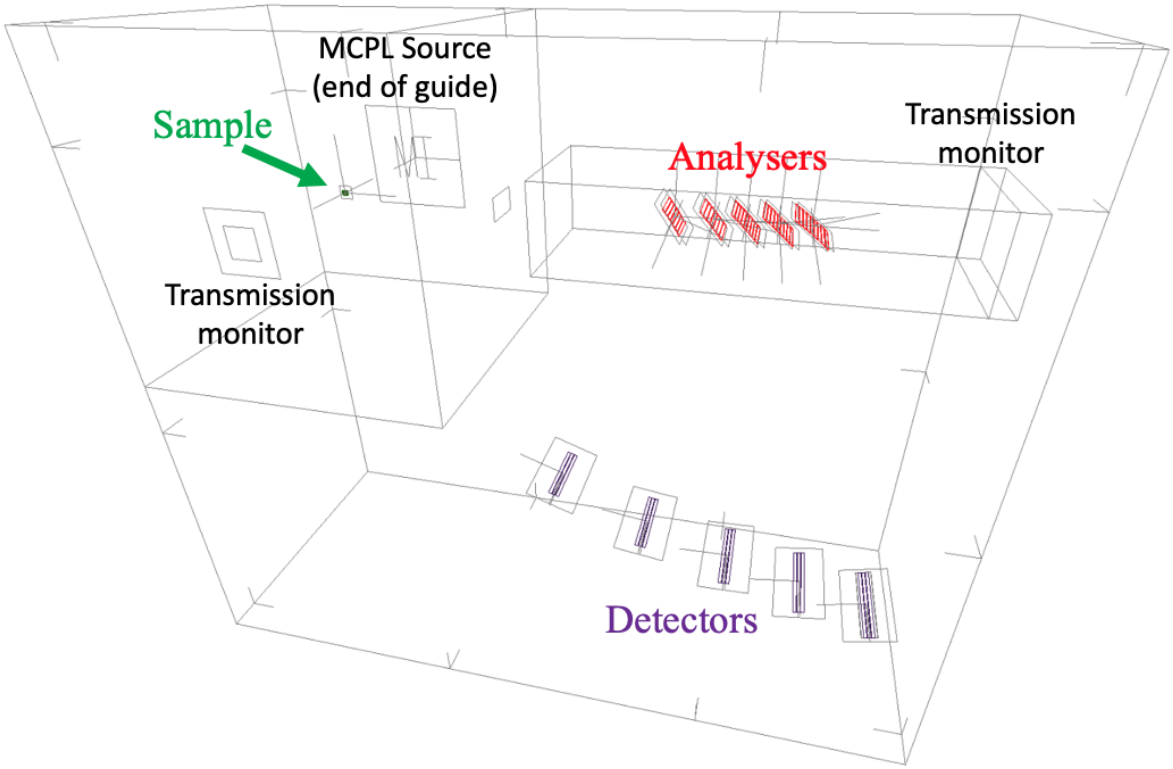

Figure 7.1: McStas model of the sample and scattering characterisation system.

rates, but implementing only one Q-channel is the result of a limitation coming from the linearity of the McStas simulation process described in Section 2.1.

The technique of grouping components together is used within the Q-channel, to handle the five sets (arcs) of analyser blades, all of which divide the beam into the partition that is scattered towards the detectors and the partition that is propagated towards the next set of analysers (or the beam stop behind the last set). In order to allow neutrons to proceed without interaction with a set of analyser blades – due to transmission or simply avoiding them all – an extra virtual component is added to each group, that mimics an interaction without changing the neutron state, and thereby prevents neutrons to be removed from the simulation. Neutrons still have to follow the order of the groups, so back-scattering or multiple scattering among blades of the same arc is still not possible in the simulations.

The intent is to determine the incident detector rates, therefore the simulation of the detection process is out of scope. Detectors are modelled with McStas monitor components, and a neutron is counted as incident for a detector tube if it crosses the plane at the centre of the detectors within the outline of that particular tube. The sample–analyser distance is equal to the analyser–detector distance, meaning that symmetrical Q-channels are modelled.

Allowing the neutrons selected by a set of analysers to reach the detectors (monitor

components) while another part of neutrons has to be propagated in completely different direction toward the next set of analysers, is by default not possible in McStas. This problem is solved by further grouping of components. For each monitor component probing different properties of neutrons at the detector position, an extra monitor component is added in the direction of the next set of analysers. This way the neutrons can reach a member of the component group downstream in the component file in both direction. Only those neutrons are removed from the simulation which do not reach either the monitor component for detectors or the monitor components that covers the whole solid angle leading to the next set of analysers.

Although the cross-talk shielding between energy- and Q-channels is not explicitly included in the model, as a consequence of the above McStas neutron propagation process, a neutron can reach a particular detector tube only by scattering in one of the corresponding analyser blades. This is practically equivalent to the conditions applied in the data analysis process for the Geant4 simulations, and also results in an ideal cross-talk shielding absorbing all stray neutrons. The case is similar for the filtering system, that is replaced by a monitor component, that transmits all neutrons below 7 meV energy and none above.

As this section demonstrates, using McStas to model such complex system as the analyser–detector system of BIFROST in detail is not straightforward and is subject to certain limitations.

7.3 Pyrolytic graphite sample

Figure 7.2 depicts the time-averaged energy spectra of neutrons at the sample and different parts of the scattering characterisation system from the McStas and Geant4 simulations using a pyrolytic graphite single crystal sample. Due to the large mosaicity of the sample, neutrons of a broad energy range – centred around 5.0 meV – are scattered toward the single Q-channel, reaching the 2.7 meV analysers and therefore missing from the sample transmission spectrum. The transmission through the sample is 80%, 57% higher than it is with vanadium, but still there is no need for logarithmic scale as neutrons scattered on the sample are concentrated on the analysers.

The change of the spectrum between the 2.7 meV and 5.0 meV analysers is caused by the spread of neutrons, and absorption in the analysers. The neutrons selected by the 5.0 meV analysers are scattered towards the corresponding detector triplet, and are therefore absent from the analyser transmission spectrum.

The time-averaged neutron intensities acquired by the integration of the energy

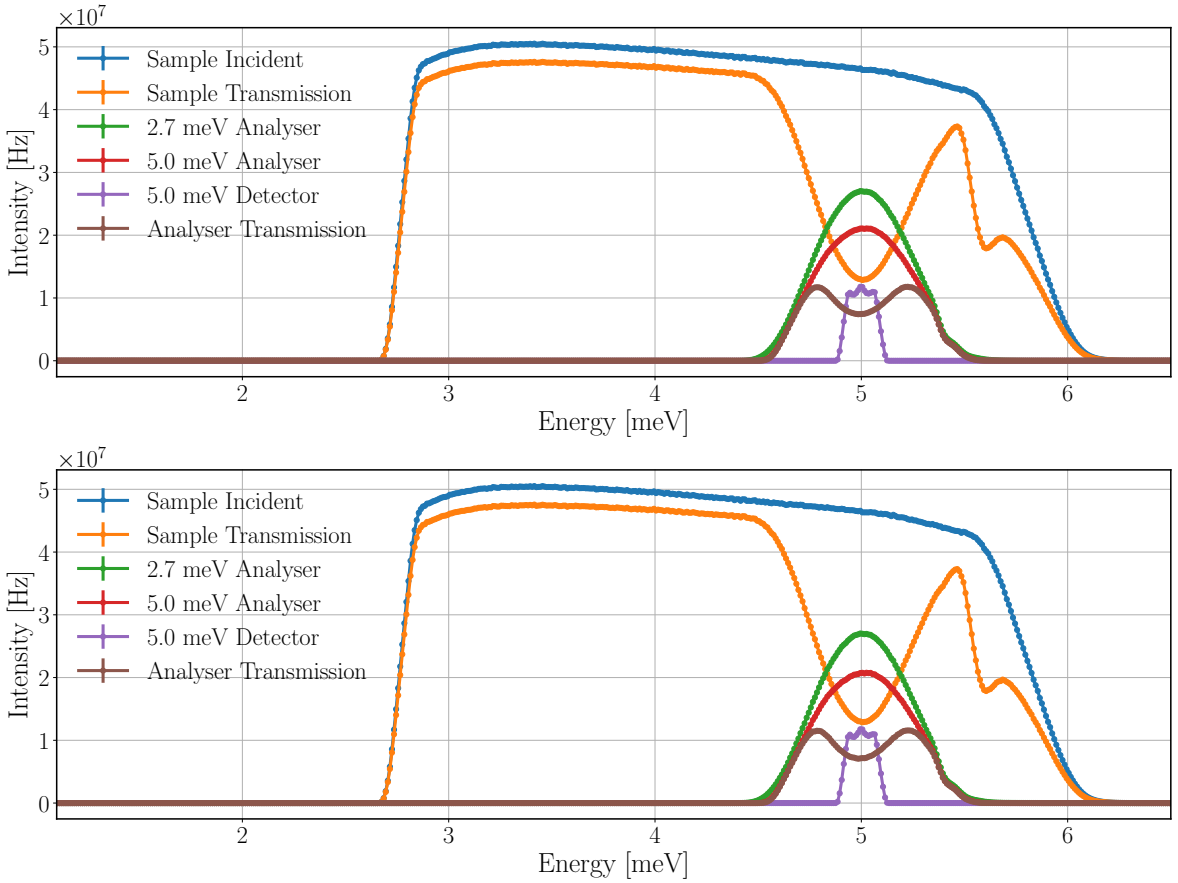

Figure 7.2: Time-averaged neutron energy spectra at the sample and the scattering characterisation system with pyrolytic graphite single crystal sample in McStas (top) and Geant4 (bottom) simulation. Incident beam on sample (in blue), beam transmitted through the sample (in orange), beam on the set of analysers for 2.7 meV neutrons (in green), beam on the set of analysers for 5.0 meV neutrons (in red), neutrons hitting the detector triplet for 5.0 meV (in purple), beam transmitted through all sets of analysers (in brown). The lines are only joining the points.

spectra are shown in Table 7.1. The results of the McStas and Geant4 simulations agree with only minor differences.

The structure of the incident energy spectrum of the detector triplet is the result of summing the spectra of all three detectors, as depicted in Figure 7.3.

The different energy ranges probed by the detector tubes of a triplet as a result of the slightly different scattering angle of neutrons on the analysers with coarse mosaicity is apparent as is for vanadium sample. In this case, however it is not only the analysers, that spread the beam energy selectively, but the sample too. The sample spreads the neutron beam horizontally, by scattering neutrons with lower energies in larger, and neutrons with higher energies in smaller angle than the scattering angle given by the Bragg formula (Equation 1.4). The combined effect of the horizontal spread on the

Position	McStas [Hz]	Geant4 [Hz]
Sample Incident	$1.45{\cdot}10^{10}$	$1.45{\cdot}10^{10}$
Sample Transmission	$1.16{\cdot}10^{10}$	$1.16{\cdot}10^{10}$
2.7 meV Analyser	$1.50{\cdot}10^{9}$	$1.50{\cdot}10^{9}$
5.0 meV Analyser	$1.20{\cdot}10^{9}$	$1.19{\cdot}10^{9}$
5.0 meV Detector	$1.98{\cdot}10^{8}$	$1.98{\cdot}10^{8}$
Analyser Transmission	$7.47{\cdot}10^{8}$	$7.31{\cdot}10^{8}$

Table 7.1: Time-averaged neutron intensities at the sample and different parts of the scattering characterisation system with pyrolytic graphite single crystal sample with McStas and Geant4.

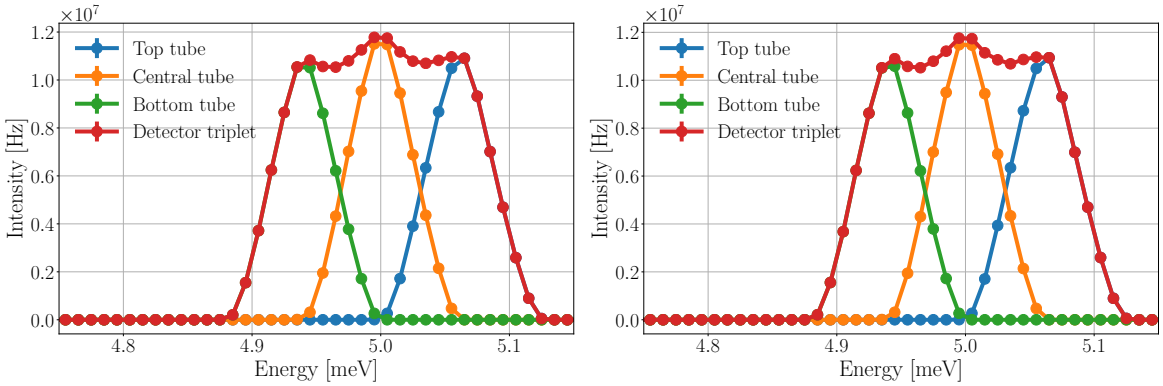

Figure 7.3: Time-averaged incident neutron energy spectra of the 5 meV detector tubes in McStas (left) and Geant4 (right) simulations, with pyrolytic graphite sample. The lines are only joining the points.

sample and vertical spread on the analysers is visible in Figure 7.4, showing a diagonal shape in the time-averaged neutron intensities in the plane over the detector tubes.

Integrating the incident neutron intensities in Figure 7.4 over the areas of the tubes gives the time-averaged incident rates for the tubes, presented in Table 7.2. The results show that the time-averaged incident rate for a single detector tube can be almost as high as 70 MHz.

Detector tube	McStas [Hz]	Geant4 [Hz]
Top	$6.69{\cdot}10^{7}$	$6.70{\cdot}10^{7}$
Central	$6.95{\cdot}10^{7}$	$6.93{\cdot}10^{7}$
Bottom	$6.20{\cdot}10^{7}$	$6.20{\cdot}10^{7}$

Table 7.2: Time-averaged incident neutron rates of the 5 meV detector tubes in McStas and Geant4 simulations, with pyrolytic graphite sample.

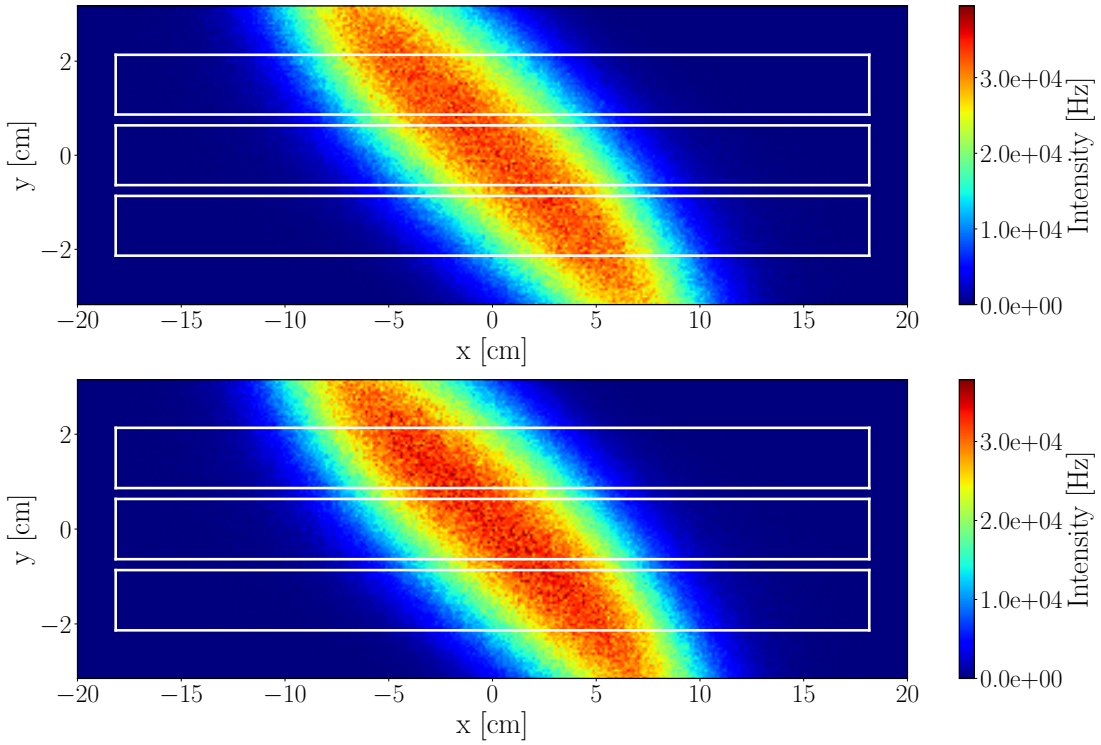

Figure 7.4: Time-averaged neutron intensities in the plane of the 5 meV detector tubes in McStas (at top) and Geant4 (at bottom) simulations, with pyrolytic graphite sample. The white lines indicate the outlines of the detector tubes.

In order to acquire the peak rate of the detector tube, the time structure of the elastic peak is depicted in Figure 7.5 for the 5 meV detectors.

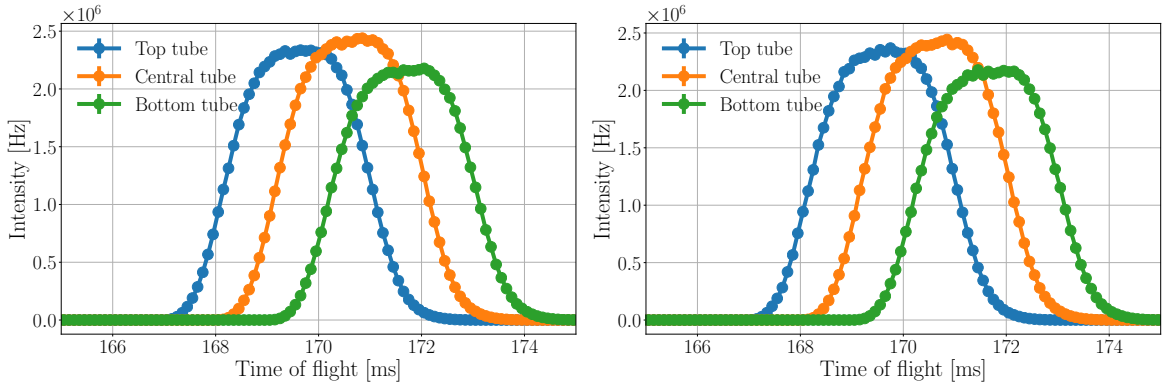

Figure 7.5: ToF spectrum of neutrons at the 5 meV detector triplet in McStas (left) and Geant4 (right) simulations, with pyrolytic graphite sample. The lines are only joining the points.

By taking into account only those neutrons which arrive to the detectors at the peak of their ToF distribution in a short time range of 0.1 ms (see Figure 7.6), the integration over the areas of the detector tubes gives the peak incident rates, as presented in Table 7.3. The peak rate of course occurs at different times for each tube of the triplet.

The results demonstrate that the peak incident rate on a single detector tube can be as high as 1.7 GHz.

It can be also concluded that all results of the McStas and Geant4 simulations are visually indistinguishable.

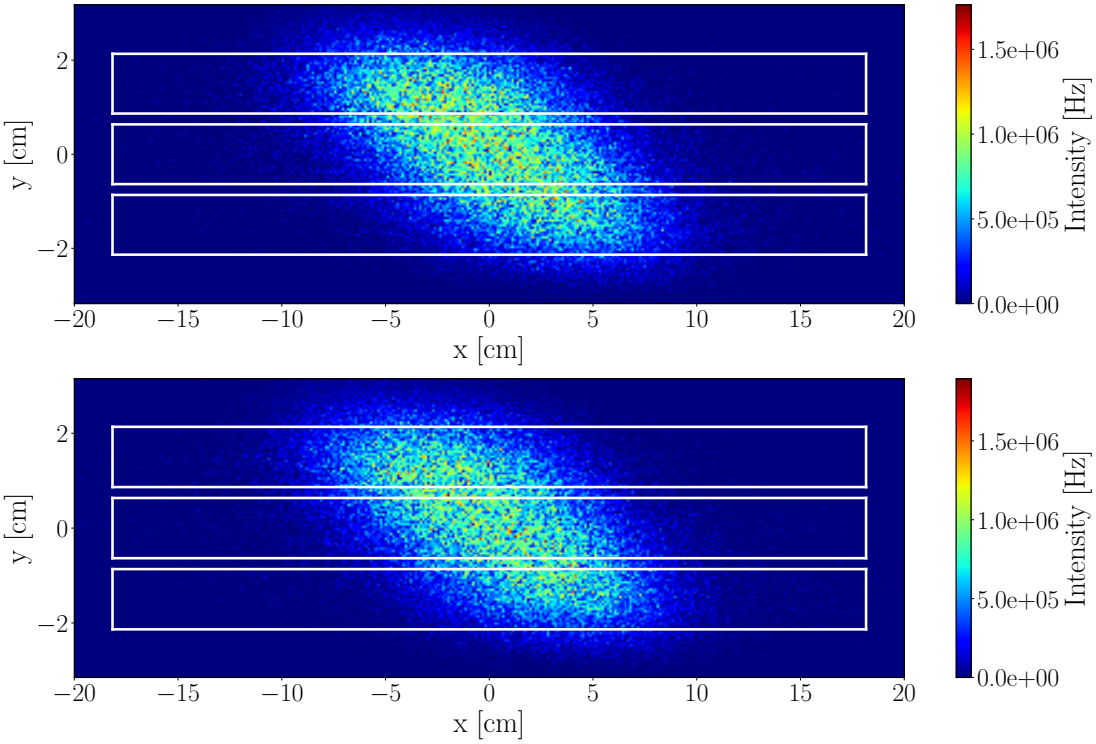

Figure 7.6: Neutron intensities in the plane of the 5 meV detector tubes at the peak of the ToF spectrum of the central tube in McStas (top) and Geant4 (bottom) simulations, with pyrolytic graphite sample. The white lines indicate the outlines of the detector tubes.

Detector tube	McStas [Hz]	Geant4 [Hz]
Top	$1.67{\cdot}10^9$	$1.69{\cdot}10^9$
Central	$1.74{\cdot}10^9$	$1.75{\cdot}10^9$
Bottom	$1.56{\cdot}10^9$	$1.56{\cdot}10^9$

Table 7.3: Peak incident rate of the 5 meV detector tubes in McStas and Geant4 simulations, with pyrolytic graphite sample.

7.4 Yttrium oxide sample

To give an impression on how the rates change with a different single crystal that is not the worst-case sample but also has a strong Bragg peak, the same simulation and analysis process is repeated using an Y_2O_3 sample.

Figure 7.7 demonstrates the change of the time-averaged neutron energy spectrum along the neutrons path at the sample in the scattering characterisation system. The time-averaged neutron intensities acquired by the integration of the energy spectra are shown in Table 7.4.

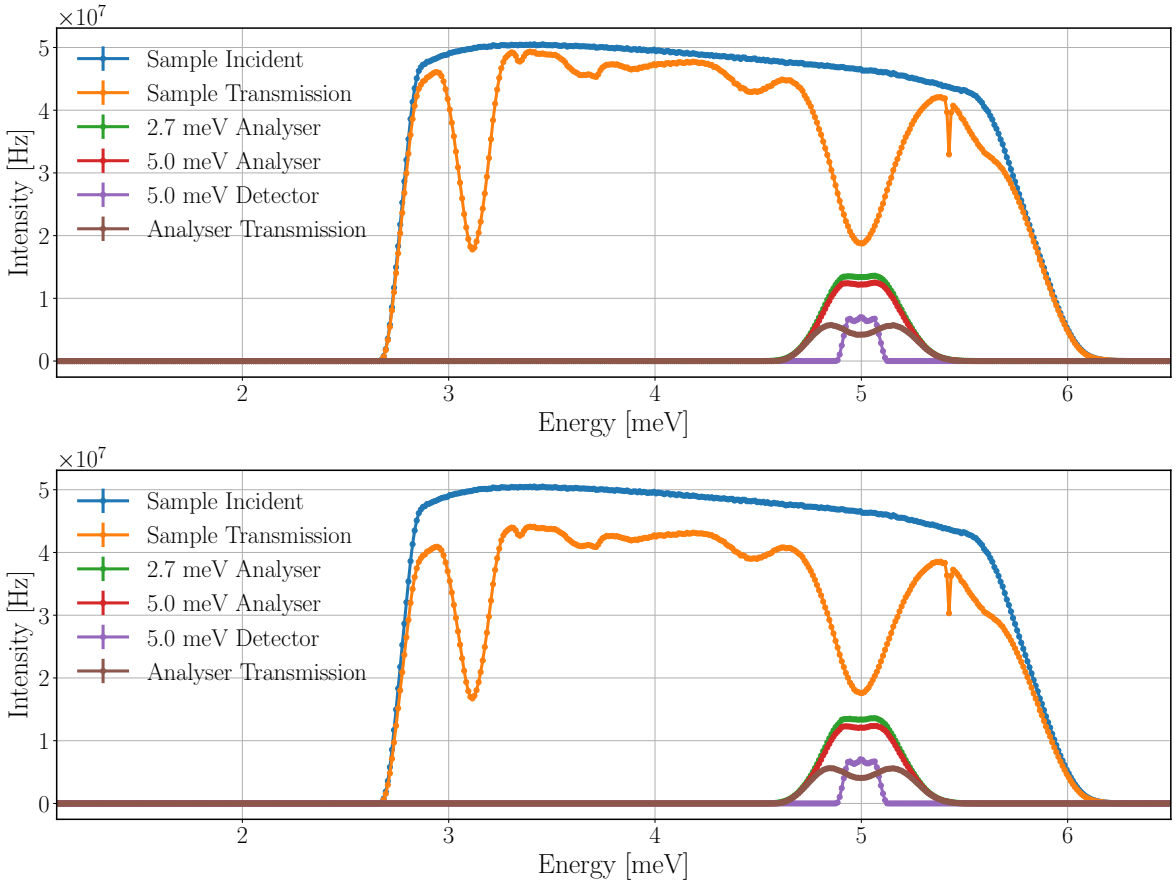

Figure 7.7: Time-averaged neutron energy spectra at the sample and the scattering characterisation system with an Y_2O_3 single crystal sample in McStas (top) and Geant4 (bottom) simulation. Incident beam on sample (in blue), beam transmitted through the sample (in orange), beam on the set of analysers for 2.7 meV neutrons (in green), beam on the set of analysers for 5.0 meV neutrons (in red), neutrons hitting the detector triplet for 5.0 meV (in purple), beam transmitted through all sets of analysers (in brown). The lines are only joining the points.

The results of the McStas and Geant4 simulations agree with only minor differences, with the only exception being the transmission spectrum of the sample. The transmission of the sample is 10% higher in McStas, with the same lower intensity bands apparent in the spectrum caused by several crystal planes where the Bragg-criterion is fulfiled for different neutron energies – including the hkl=-2-2-2 plane for 5.0 meV. The source of the discrepancy is the absorption process in the sample, as different absorption cross-sections are used in the two simulation tools, as described earlier in Section 2.3.

The transmission through the sample in Geant4 is 77%, that is 3% lower than that of the pyrolytic graphite despite the weaker Bragg peak for the 5.0 meV neutrons, due to the higher absorption and presence of additional strong Bragg peaks.

Position	McStas [Hz]	Geant4 [Hz]
Sample Incident	$1.45{\cdot}10^{10}$	$1.45{\cdot}10^{10}$
Sample Transmission	$1.24{\cdot}10^{10}$	$1.12{\cdot}10^{10}$
2.7 meV Analyser	$6.01{\cdot}10^{8}$	$6.00{\cdot}10^{8}$
5.0 meV Analyser	$5.52{\cdot}10^{8}$	$5.48{\cdot}10^{8}$
5.0 meV Detector	$1.21{\cdot}10^{8}$	$1.21{\cdot}10^{8}$
Analyser Transmission	$2.96{\cdot}10^{8}$	$2.91{\cdot}10^{8}$

Table 7.4: Time-averaged neutron intensities at the sample and different parts of the scattering characterisation system with an Y_2O_3 single crystal sample in McStas and Geant4 simulation.

The spectrum of the 2.7 meV analyser arc shows that despite the presence of multiple Bragg peaks, it is only the 5.0 meV neutrons that are scattered toward the Q-channel on the hkl=-2-2-2 plane. There are, however, three other planes on which the 5.0 meV neutrons are Bragg-scattered (hkl=2-3-3, hkl=1-2-3 and hkl =1-3-2), apparently not toward the Q-channel, causing the slight dip of the peak at 5 meV. The spread of the neutrons after the sample is less significant than it was with pyrolytic graphite, so fewer neutrons are lost on the way toward the 5.0 meV analysers.

The time-averaged neutron intensities in the plane of the 5 meV detector tubes depicted in Figure 7.8 show a similar diagonal shape as for pyrolytic graphite because of the energy dependence of the scattering angle both for sample and analysers. The time-averaged incident neutron rate for the detector tubes in Table 7.5 – acquired by integration over the area of the tubes – shows that the neutrons are distributed more evenly among the tubes as a result of the flattened top of the energy spectrum. The maximum of the time-averaged incident rate for a single tube is found to be 41 MHz.

Detector tube	McStas [Hz]	Geant4 [Hz]
Top	$4.08{\cdot}10^{7}$	$4.07{\cdot}10^{7}$
Central	$4.13{\cdot}10^{7}$	$4.13{\cdot}10^{7}$
Bottom	$3.88{\cdot}10^{7}$	$3.86{\cdot}10^{7}$

Table 7.5: Time-averaged incident neutron rates of the 5 meV detector tubes in McStas and Geant4 simulations, with an Y_2O_3 sample.

Doing the calculations only for the incident neutrons that arrive at the peak (0.1 ms range) of the ToF spectra of each tube the peak incident rates are acquired, presented

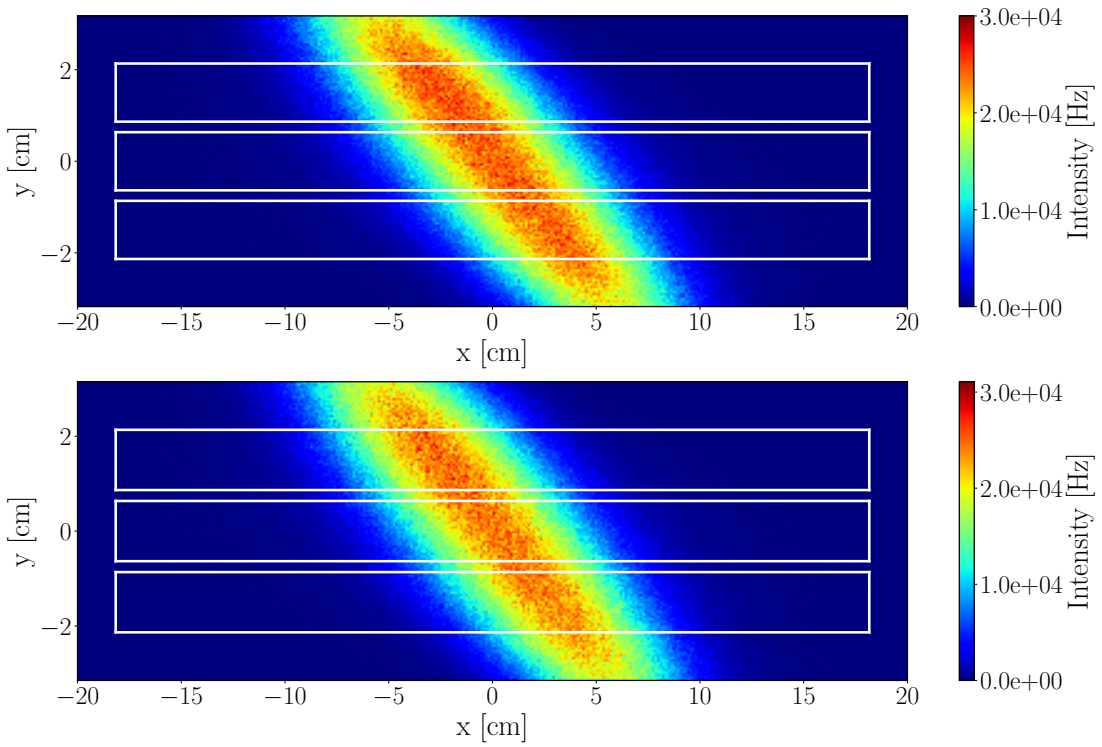

Figure 7.8: Time-averaged neutron intensities in the plane of the 5 meV detector tubes in McStas (top) and Geant4 (bottom) simulations, with an Y_2O_3 sample. The white lines indicate the outlines of the detector tubes.

in Table 7.6. The peak incident rate for a single detector tube with an Y_2O_3 sample is found to be 1 GHz.

Comparing the time-averaged and peak rates to those acquired for pyrolytic graphite, both are lower by a factor of 1.7 but still on the order of 10 MHz for time-averaged and GHz for peak rates. This means that even with a non-worst-case sample, the rates can be well above the capabilities of the standard ^{3}He detector tubes.

Detector tube	McStas [Hz]	Geant4 [Hz]
Top	$1.03{\cdot}10^9$	$1.02{\cdot}10^9$
Central	$1.05{\cdot}10^9$	$1.04{\cdot}10^9$
Bottom	$9.78{\cdot}10^8$	$9.84{\cdot}10^8$

Table 7.6: Peak incident rates of the 5 meV detector tubes in McStas and Geant4 simulations, with an Y_2O_3 sample.

This section also demonstrated that the McStas and Geant4 simulation results are in excellent agreement, regarding the detector rates.

Chapter 8

Parameter scan of BIFROST rates

Chapter 7 aimed at defining the highest possible time-averaged and peak incident detector rates of the BIFROST instrument. In order to do that, worst-case conditions are considered, and simulations are done for these fix scenarios. However, the effects of some instrument and sample parameters on the incident detector rates, are not necessarily straightforward and worth investigating. Beside proving that the results presented in Chapter 7 can be regarded as the worst-case rates, it is also important to evaluate conditions that are closer to normal operation. Therefore, in this chapter multiple parameters are scanned in order to determine their effect on the incident detector rates and simulations are done for conditions representative for normal operation.

To carry our the simulations of beam transport and conditioning system the McStas model of the instrument introduced in Section 2.1.2 is used. As demonstrated in this Chapter 7, the McStas and Geant4 simulation results of the scattering characterisation system are in excellent agreement, regarding the detector rates. For this reason, further simulations are only performed using the Geant4 model introduced in Section 6.1. The change in the incident detector rates due to modifying the studied parameters are expected to have the same trend for all single crystals, so all simulations are done using the Y_2O_3 sample. The base parameters for the simulations are the ones of the worst-case scenario defined in Section 7.1. The parameter scans are performed by changing only one parameter at a time.

In the following sections the effects of sample mosaicity, analyser mosaicity, sample size and pulse-shaping chopper opening time are investigated on the incident detector rates. Finally in the last section elastic peak rates are defined with parameters that are representative for normal operational conditions.

8.1 Sample mosaicity

The mosaicity of the sample has multiple effects on the neutron beam Bragg-scattered on a selected scattered plane toward the Q-channel. As discussed in Section 1.3, higher crystal mosaicity enables scattering neutrons of a wider energy and incident angle range due to the higher spread of crystal plane orientations, enabling them to fulfil the Bragg-criteria. For a divergent incident beam this can result in a higher total reflectivity. On the other hand, it is also stated that this higher spread of crystal plane orientations lowers the probability of scattering neutrons with energy and incident angle close to the ideal values, that can give lower peak reflectivity. The cumulative effect is depicted in Figure 8.1, showing the energy spectra of the scattered beam at the 2.7 meV analysers and the 5.0 meV detector triplet for an Y_2O_3 sample with different mosaicities.

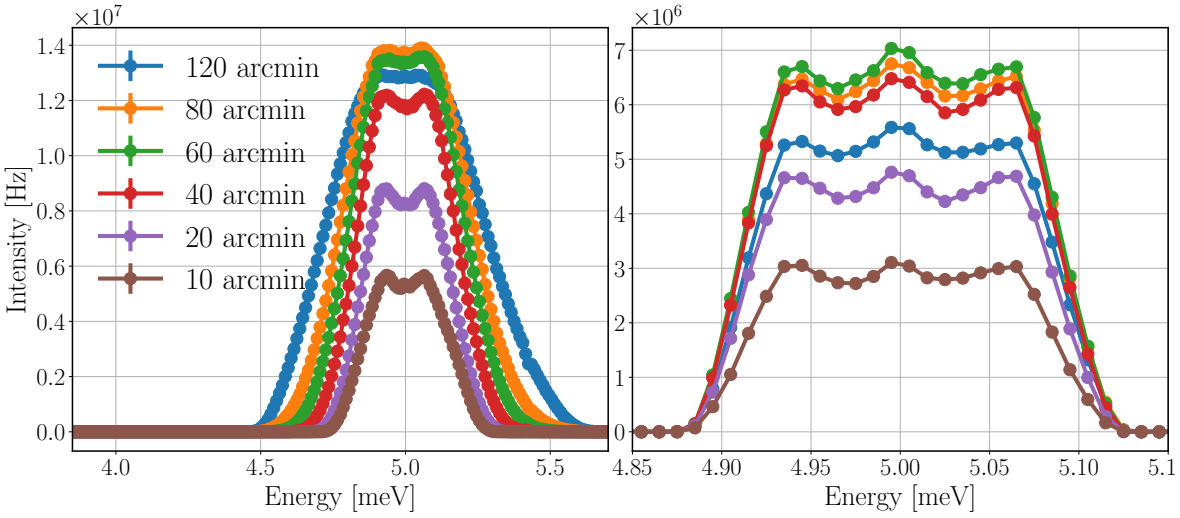

Figure 8.1: Energy spectra of the neutron beam on the set of analysers for 2.7 meV neutrons (left) and of the neutrons hitting the detector triplet for 5.0 meV (right) for different sample mosaicities with an Y_2O_3 sample. The lines are only joining the points.

The energy spectra of the beam at the 2.7 meV analyser arc shows that the sample with higher mosaicities scatters neutrons of a wider energy range toward the analysers, as expected. It also shows that the intensities at this point of the instrument are getting higher for mosaicities up until 80 arcmin and therefore intensities for 80 arcmin are higher than those for 60 arcmin. It is the energy spectrum of neutrons hitting the detector triplet for 5.0 meV, that shows that these additional neutrons do not reach the detectors, as the highest intensities are found at 60 arcmin sample mosaicity. The resulting time-averaged and peak incident rates of the central detector tube are presented in Table 8.1.

The results are in compliance with the expectation that the highest rates occur

Mosaicity [arcmin]	Time-averaged rate [Hz]	Peak rate [Hz]
120	$3.30{\cdot}10^7$	$8.37{\cdot}10^8$
80	$3.99{\cdot}10^7$	$1.02{\cdot}10^9$
60	$4.13{\cdot}10^7$	$1.04{\cdot}10^9$
40	$3.84{\cdot}10^7$	$9.63{\cdot}10^8$
20	$2.80{\cdot}10^7$	$7.07{\cdot}10^8$
10	$1.81{\cdot}10^7$	$4.54{\cdot}10^8$

Table 8.1: Time-averaged and peak incident neutron rates of the central 5 meV detector tube for different sample mosaicities with an Y_2O_3 sample.

when the mosaicity of the sample matches that of the analysers, but also show that within the ±20 arcmin range it is less than a 10% effect.

8.2 Analyser mosaicity

The mosaicity of the analysers is a fixed value of 60 arcmin for BIFROST, but it is worth briefly investigating how it would affect the rate of the detector tubes. Figure 8.2 depicts the neutron energy spectra of the 5.0 meV detector triplet for different analyser mosaicities with an Y_2O_3 sample with a mosaicity of 60 arcmin.

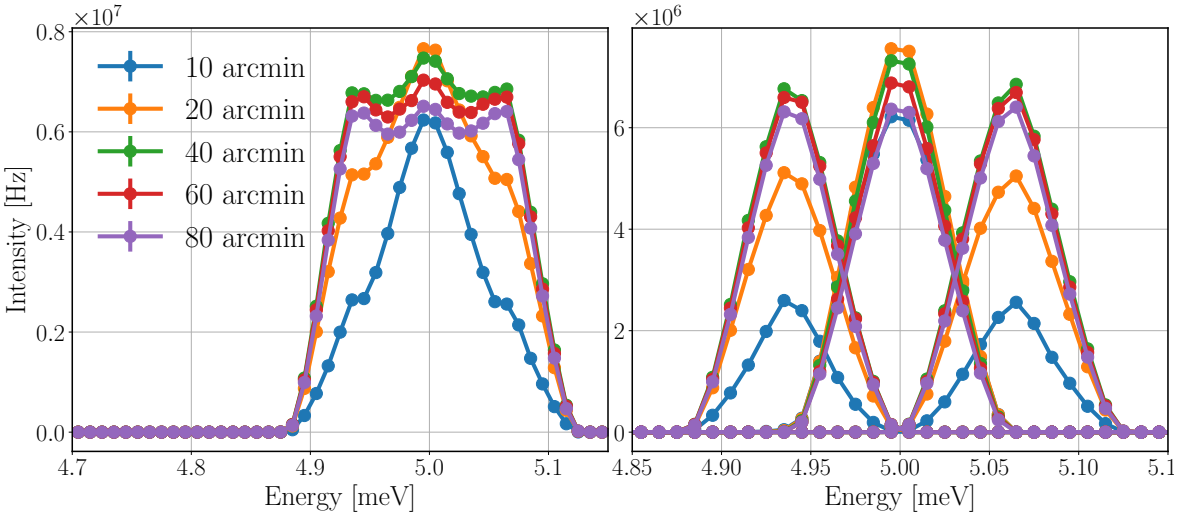

Figure 8.2: Energy spectra of the neutrons hitting the detector triplet for the three tubes together (left) and separately (right) for 5.0 meV for different analyser mosaicities with an Y_2O_3 sample. The lines are only joining the points.

The spectra of the three tubes separately show that for mosaicities below 40 arcmin the two tubes on the sides are under-illuminated compared to the tube in the centre, as

Mosaicity [arcmin]	Time-averaged rate [Hz]	Peak rate [Hz]
10	$4.10 \cdot 10^7$	$1.04 \cdot 10^9$
20	$4.68 \cdot 10^7$	$1.19 \cdot 10^9$
40	$4.45 \cdot 10^7$	$1.12 \cdot 10^9$
60	$4.13 \cdot 10^7$	$1.04 \cdot 10^9$
80	$3.84 \cdot 10^7$	$9.64 \cdot 10^8$

Table 8.2: Time-averaged and peak incident neutron rates of the central 5 meV detector tubes for different analyser mosaicities with an Y_2O_3 sample.

expected from the study of the prismatic analyser concept [58]. In order to harness the benefits of the prismatic analyser concept, the analyser mosaicity has to be large enough to sufficiently cover all used detectors. Increasing the mosaicity above 40 arcmin, the intensity in all three tubes is getting slightly lower. The resulting time-averaged and peak rates of the central detector tube are presented in Table 8.2.

The results show that the incident rate in a single detector tube could be 13–14% higher in the central tube with 20 arcmin mosaicity compared to the result with 60 arcmin, however the mosaicity has to be higher to sufficiently illuminate all three detectors, and in the range of 40–80 arcmin the change is less than 10%.

8.3 Sample size

Sample size is the limiting factor in many scientific cases, as it is not easy to grow large samples of some types. The beam delivery system of BIFROST is optimised for sample cross-sections up to 15×15 mm^2 but the realistic sample sizes for the intended applications are much smaller than that, with an expected minimum sample size going down to 1 mm^3. The heigh, width and thickness of the sample can have different effects on the incident detector rates, but in this parameter scan their cumulative effects are investigate, using cylindrical samples with equal diameter and height. The energy spectra of the scattered beam at the 2.7 meV analysers and the 5.0 meV detector triplet for an Y_2O_3 sample of different sizes are depicted in Figure 8.3. The resulting time-averaged and peak incident rates of the central detector tube are presented in Table 8.3.

As expected, the larger the sample, the higher the intensities are. By reducing the sample size parameter (height and diameter) from 15 mm to 5 mm and 1 mm, the time-averaged incident rate of the centre tube drops by a factor of 10.5 and 900

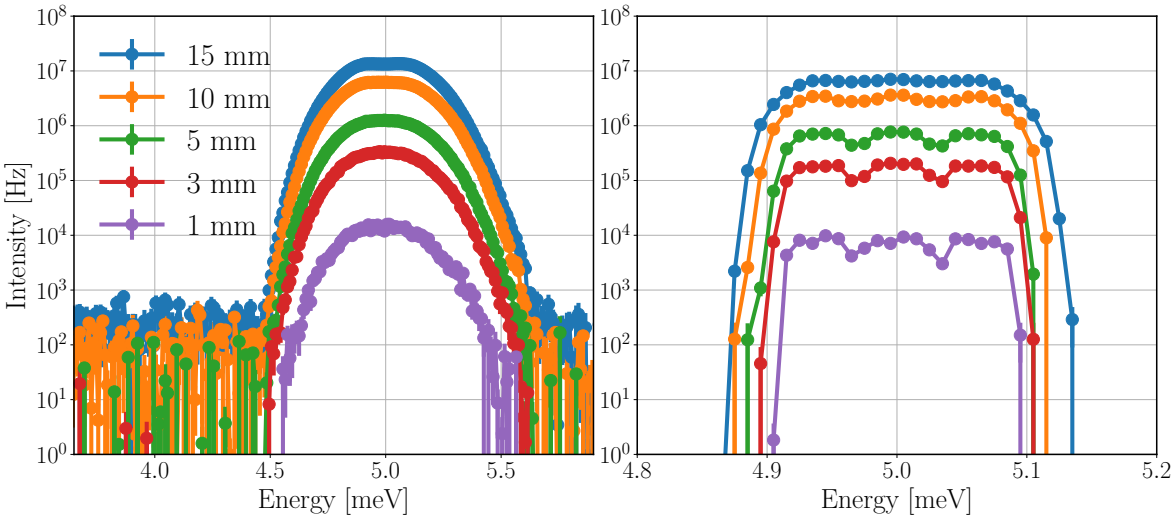

Figure 8.3: Energy spectra of the neutron beam on the set of analysers for 2.7 meV neutrons (left) and of the neutrons hitting the detector triplet for 5.0 meV (right) for an Y_2O_3 sample of different sizes. The diameter and height of the cylindrical samples are equal, with the magnitude indicated in the legend. The lines are only joining the points.

Sample size [mm]	Time-averaged rate [Hz]	Peak rate [Hz]
15	$4.13{\cdot}10^7$	$1.04{\cdot}10^9$
10	$1.93{\cdot}10^7$	$4.93{\cdot}10^8$
5	$3.92{\cdot}10^6$	$1.01{\cdot}10^8$
3	$1.04{\cdot}10^6$	$2.8{\cdot}10^7$
1	$4.6{\cdot}10^4$	$1.6{\cdot}10^6$

Table 8.3: Time-averaged and peak incident neutron rates of the central 5 meV detector tube for an Y_2O_3 sample of different sizes.

respectively. Due to the better resolutions in case of smaller samples the drop in the peak incident rate is lower, a factor of 10.3 for 5 mm and a factor of 650 for 1 mm.

Another effect of the better resolution is visible in the energy spectra of the detector triplets, where the three-peak structure is more apparent for smaller samples.

8.4 Pulse-shaping chopper opening time

The energy resolution of the instrument can be increased at the cost of neutron intensity by modifying the opening time of the pulse-shaping chopper. The flux on the sample and the detectors are both expected to drop significantly in case of the high resolution setting of BIFROST, where the pulse-shaping chopper opening time is merely 0.1 ms, compared to the high flux mode achieved by an opening time of 5 ms.

The energy spectra of the neutron beam at the sample and the 5.0 meV detector triplet for an Y_2O_3 sample for different pulse-shaping chopper opening times are depicted in Figure 8.4, with the time-averaged intensities presented in Table 8.4. The resulting time-averaged and peak rates of the central detector tube are presented in Table 8.5.

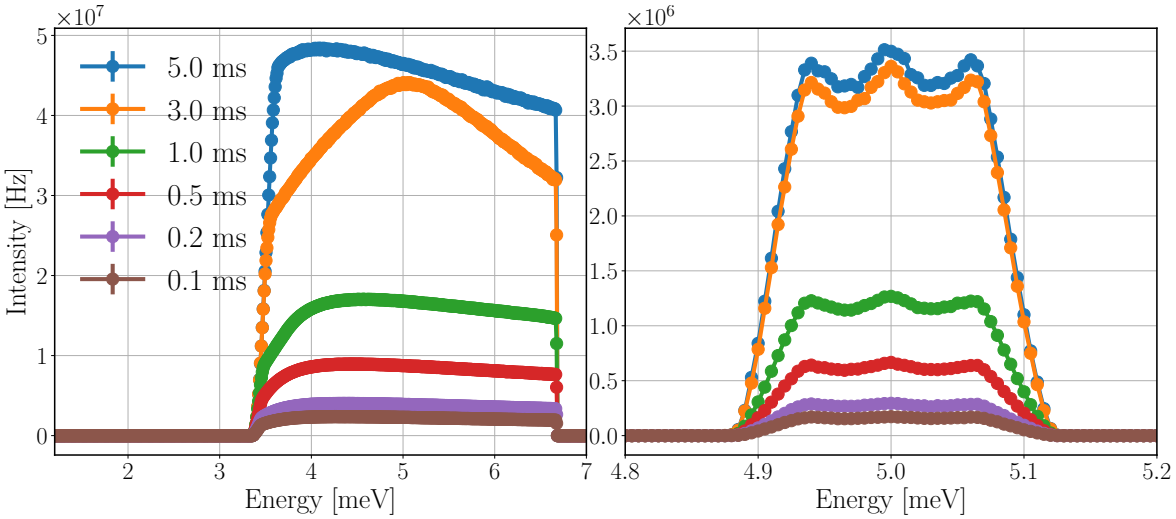

Figure 8.4: Energy spectra of the neutron beam on the sample (left) and of the neutrons hitting the detector triplet for 5.0 meV (right) for an Y_2O_3 sample for different pulse-shaping chopper opening times. The lines are only joining the points.

PSC opening time [ms]	Sample [Hz]	5.0 meV detectors [Hz]
5.0	$1.44{\cdot}10^{10}$	$1.21{\cdot}10^{8}$
3.0	$1.22{\cdot}10^{10}$	$1.14{\cdot}10^{8}$
1.0	$5.05{\cdot}10^{9}$	$4.38{\cdot}10^{7}$
0.5	$2.67{\cdot}10^{9}$	$2.27{\cdot}10^{7}$
0.2	$1.20{\cdot}10^{9}$	$1.01{\cdot}10^{7}$
0.1	$7.03{\cdot}10^{8}$	$5.93{\cdot}10^{6}$

Table 8.4: Time-averaged neutron intensities at the sample and the 5.0 meV detector tubes with an Y_2O_3 sample for different pulse-shaping chopper (PSC) opening times.

As expected, the time-averaged rates on the sample and on the detectors decrease with shorter pulse-shaping chopper opening times. The difference in time-averaged incident rates between the high flux mode (5 ms) and the high resolution mode (0.1 ms) is approximately a factor of 20 for both the detector triplet and the central tube. Regarding the peak rates in the central tube, however, this drop is less apparent. The highest rate for a 3 ms opening time is the same (within statistical uncertainty) as the

PSC opening time [ms]	Time-averaged rate [Hz]	Peak rate [Hz]
5.0	$4.13{\cdot}10^7$	$1.04{\cdot}10^9$
3.0	$3.91{\cdot}10^7$	$1.04{\cdot}10^9$
1.0	$1.50{\cdot}10^7$	$8.76{\cdot}10^8$
0.5	$7.79{\cdot}10^6$	$5.31{\cdot}10^8$
0.2	$3.46{\cdot}10^6$	$2.52{\cdot}10^8$
0.1	$2.03{\cdot}10^6$	$1.50{\cdot}10^8$

Table 8.5: Time-averaged and peak incident neutron rates of the central 5 meV detector tube with Y_2O_3 sample for different pulse-shaping chopper opening times.

rate for 5 ms, and the difference compared to 0.1 ms opening time is only a factor of 6.9. The reason for this difference is the better ToF resolution with shorter pulse-shaping chopper opening times. The higher time-averaged rates are distributed over a longer period of time on the detectors, as it is demonstrated in Figure 8.5, showing the effect of the pulse-shaping chopper opening time on the ToF spectrum of neutrons hitting the detectors.

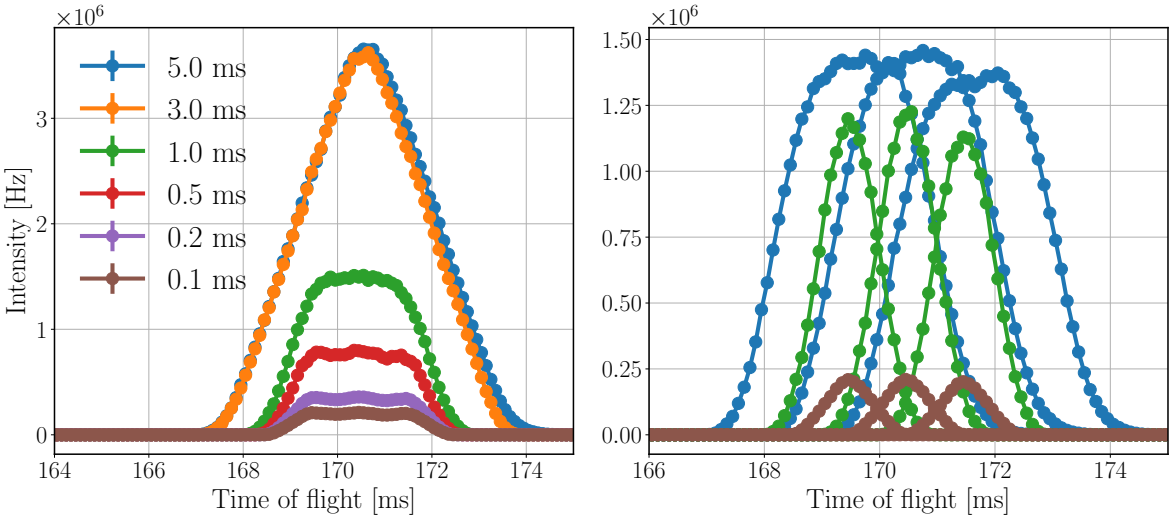

Figure 8.5: ToF spectrum of neutrons at the 5 meV detector triplet for the three tubes together (on left) and separately (on right) with Y_2O_3 sample for different pulse-shaping chopper opening times. The separated spectrum is not displayed in all cases in the righthand figure to avoid the figure being overcrowded. The lines are only joining the points.

The longer the opening time, the broader the ToF peaks are. This directly affects the energy resolution, and also increases the dead time in case of saturation. If one tube of a triplet is saturated, then none of the three can read out data, as they are connected in series. This means that for the detector triplet in the presented case for 5.0 ms pulse-shaping chopper opening time no data is recorded for more than 6 ms.

8.5 Elastic peak rates in representative operational conditions

Parameters chosen in Chapter 7 correspond to a possible worst-case scenario and rates acquired are far above the capabilities of ^{3}He tubes. However, the combination of a strongly scattering large sample and the highest flux mode is rather artificial, so it is worth evaluating a more representative operational scenario.

BIFROST is designed for small samples, as sample size is the limiting factor in many science cases. Hence, cm-size crystals are not to be expected very often, only large samples with small magnetic moments, and therefore small magnetic Bragg peak intensity. There is another parameter directly affecting the intensities but not discussed yet, the accelerator power of the ESS source. As mentioned in earlier sections, the source power of 5 MW is used for all simulations. In Section 1.1 it is explained that this is the eventual operational power of ESS, however, it will initially operate at 2 MW. The intensities are expected to scale linearly with the source power, and in terms of simulations, the source power is in fact only a multiplication factor in the ESS butterfly moderator source component as pointed out in Section 2.1.2.

For these reasons, the following parameters are selected to define the rates in a more representative operational case: 2 MW source power, 1 ms pulse-shaping chopper opening time, an Y_2O_3 single crystal sample with a height and diameter of 3 mm, and mosaicity of 60 arcmin. The time-averaged energy spectra of the neutron beam at the sample and different positions of the scattering characterisation system, acquired with these parameters are demonstrated in Figure 8.6, along with the integral values presented in Table 8.6. The resulting time-averaged and peak incident neutron rates of the 5 meV detector tubes are presented in Table 8.7.

Position	Intensity [Hz]
Sample Incident	$1.07{\cdot}10^8$
Sample Transmission	$1.01{\cdot}10^8$
2.7 meV Analyser	$1.84{\cdot}10^6$
5.0 meV Analyser	$1.70{\cdot}10^6$
5.0 meV Detector	$4.1{\cdot}10^5$
Analyser Transmission	$8.71{\cdot}10^5$

Table 8.6: Time-averaged neutron intensities at the sample and different parts of the scattering characterisation system with an Y_2O_3 sample, using 2 MW source power, 1 ms PSC opening time, 3 mm height and diameter sample size and 60 arcmin sample mosaicity.

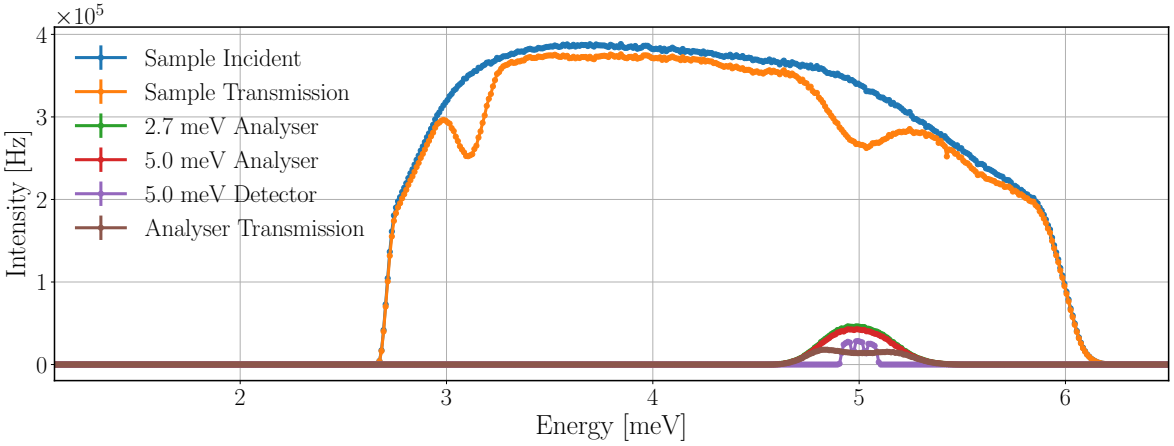

Figure 8.6: Time-averaged neutron energy spectra at the sample and the scattering characterisation system with an Y_2O_3 sample in Geant4 simulation using 2 MW source power, 3 mm height and diameter sample size and 60 arcmin sample mosaicity. Incident beam on sample (in blue), beam transmitted through the sample (in orange), beam on the set of analysers for 2.7 meV neutrons (in green), beam on the set of analysers for 5.0 meV neutrons (in red), neutrons hitting the detector triplet for 5.0 meV (in purple), beam transmitted through all sets of analysers (in brown). The lines are only joining the points.

Detector tube	Time-averaged rate [Hz]	Peak rate [Hz]
Top	$1.3{\cdot}10^5$	$9.3{\cdot}10^6$
Central	$1.5{\cdot}10^5$	$9.9{\cdot}10^6$
Bottom	$1.3{\cdot}10^5$	$9.4{\cdot}10^6$

Table 8.7: Time-averaged and peak incident neutron rates of the 5 meV detector tubes with an Y_2O_3 sample, using 2 MW source power, 1 ms PSC opening time, 3 mm height and diameter sample size and 60 arcmin sample mosaicity.

The combined effect of the lower source power, shorter pulse-shaping chopper opening time and smaller sample size (cross-section) decreased the time-averaged neutron intensity on the sample significantly, by a factor of 136 compared to the worst-case scenario with an Y_2O_3 sample presented in Section 7.4. Due to the reduced sample thickness, the transmission through the sample is increased to 94% from 77%, as a result of lower absorption and weaker Bragg peaks.

The lower incident intensity on the sample, and weaker Bragg peak lead to a drop by a factor of 322–326 in the time-averaged neutron intensity on both the 2.7 and 5.0 meV analysers. The drop in the time-averaged neutron intensity on the 5.0 meV detector triplet is a little bit lower, a factor of 295, due to the smaller divergence and better energy resolution of the neutron beam compared to the worst-case scenario.

The highest time-averaged incident neutron rate on a single tube is found to be

0.15 MHz, that means a drop by a factor of 275, but the peak incident rate is 9.9 MHz, which is lower only by a factor 105 compared to the worst-case results. The numbers and reduction factors are in accordance with previous simulations in Sections 8.3 and 8.4 where the effect of sample size and pulse-shaping chopper opening time were investigated separately.

There are factors not taken into account in the current study, that may further reduce the intensities slightly on the detectors, like the non-ideal transmission of the filtering system, and the effect of the divergence jaws applicable for reducing the angular spread of neutrons

Chapter 9

Summary and outlook

The European Spallation Source is designed to operate using the most powerful spallation neutron source in the world. This source is expected to subject the detectors to unprecedented neutron fluxes, that can saturate the detectors and therefore degrade the performance of the instruments. The presented PhD work aimed to help avoiding such cases, by implementing full simulation models of two ESS instruments using the combination of multiple simulation tools, and use them to study the detector rates and performance in various scenarios.

In Chapter 3 the study of the LoKI detector rates is presented, that is representative for both small-angle neutron scattering instruments at ESS. A generic Geant4 simulation model of the rear detector bank is developed, consisting of Boron-Coated Straws detector tubes. This detector bank model is connected with the McStas model of the instrument with the application of the MCPL tool, and the resulting full simulation model is used to study the incident and detected rates for multiple instrument settings.

It is found that the instantaneous detection rate of a single straw, the functional unit of the detector can be as high as 458 kHz at 5 MW ESS source power. Given that such a straw is expected to start saturating at 50–100 kHz, some straws are expected to saturate at 800–1000 kW of source power. The results demonstrate that the BCS tubes with the conventional parameters can potentially compromise the instrument performance for high flux configurations.

The generic BCS detector model implemented for Geant4 simulations is used in Chapter 4 to carry out a complex analysis in order to evaluate various aspects of the BCS detector performance. This study is made in the context of most realistic applications that might be envisaged. The aim is to have a complete set of generally applicable results.

The detection efficiency of a single straw, and even of complete detector tubes with seven straws are shown to be low, as expected. Therefore, overlapping layers (panels)

of detectors are needed to achieve a decent efficiency. The cost-efficient number of panels depends on the application and the relevant neutron wavelength range.

The absorption (not resulting in conversion to detectable particles) in B_4C is 6.5–8 times more than in Al and Cu combined. The absorption from these two mechanical materials in the detector is in the range of 1.5–4.5% of the incident neutrons depending on the wavelength. Pure unalloyed material was modeled in the study; alloyed materials and impurities may significantly increase this and need to be considered. At smaller wavelengths the fraction of neutrons transmitted through the detector is high (50–60% at 0.6 Å) and therefore absorbant shielding behind the detector is a must for applications below 5 Å.

Activation analysis of such a detector has been implemented. The activation is dominated by copper, as expected, with a cooling time of a few days. The radiation background from activated materials will not interfere with the data acquisition. The activation during operation at ESS is not expected to be a limitation for maintenance. The calculated numbers have been presented in a fashion that could be scaled to real applications.

As presented in Chapter 5, the scattering has been studied in detail, namely its effect on quantities like the position along and perpendicular to the straws, the neutron time of flight, polar and azimuthal angle, neutron wavelength and energy, and scattering vector, all in terms of the fraction of neutrons that end up as signal, scattered background, transmitted through the detector or absorbed and non-detected. The effect of the detector geometry on the natural shape of the resolution function is shown. Scattering is highest at low wavelengths and is significant below the Bragg cut-off. It can be considered to be at acceptable levels for applications such as SANS, however, may be considerable for applications which are highly sensitive to it such as spectroscopy. Any application for spectroscopy would need detailed consideration of its effect on performance.

A polyethylene *"afterburner"* block placed behind the detector was investigated and found to increase signal by up to 4%, however, background correspondingly increased up to 15%. Therefore this is not a good solution for most applications. It also re-emphasises the need for the layer of shielding closest to the detector to be made of materials with very low neutron albedo.

As of Chapter 6 the focus is shifted to the BIFROST instrument, and in particular to the time-averaged and peak incident detector rates, that are expected to be highest in case of elastic peaks. There is no scientific reason to measure the elastic peaks as they are considered background for this instrument, however it is vital that the detectors

are not degraded by such intensity and remain capable of measuring weak inelastic signals, as soon as possible after saturation. This implies that the detector aspects of recovery time and high rate tolerance have to be carefully evaluated by measurements to prove that scientific performance will be intact.

A flexible model of the sample and the complete geometrical coverage of the scattering characterisation system implemented in Geant4 combined with the NCrystal simulation tool for correct treatment of neutron transport in crystalline materials. The first application of the special NCrystal pyrolytic graphite is presented, demonstrating its capabilities for modelling analysers for neutron scattering applications. This Geant4 model is connected to the McStas model of the instrument through the MCPL simulation tool. The use of the resulting full simulation model demonstrated with a vanadium sample. The incident detector rates for the common calibration sample are defined, the neutron energies selected by the analyser system, and the energy resolutions are found to be in accordance with the intended values of the instrument.

In Chapter 7 a reduced geometry model of the BIFROST scattering characterisation system implemented in McStas is introduced. The development of this model served the dual purpose of defining the "worst-case" incident detector rates for BIFROST in two ways, using either the McStas or the Geant4 model, and by that comparing the McStas and Geant4 simulation software to highlight their strengths and weaknesses.

The results of the McStas and Geant4 model of the scattering characterisation system are compared using various single crystal samples. The results show perfect agreement with the only exception being the transmission through the sample where a difference less than 10% is found in one case, due to the more detailed modelling of absorption in Geant4. It is concluded that McStas is capable of simulating instruments as long as 160 m, and even handling beam splitting to some extent, to treat simulations with multiple set of analysers, however the latter comes with great complexity and some limitations, as it is not within the natural usage of this simulation software. Geant4 on the other hand is not suited to simulate the beam transport system of an instrument, but with the use of NCrystal, it is an entirely appropriate tool for a scattering characterisation system with any level of geometrical complexity, and even offers the possibility to include parts like filtering system and cross-talk shielding, and taking into account back-scattering.

The incident detector rates anticipated for the BIFROST instrument for different configurations are presented. For instrument configurations and sample parameters representing worst-case conditions, it is determined that the peak rate can reach the value of 1–1.7 GHz for a single detector tube with time-averaged rates of 40–70 MHz.

These tubes are expected to reach saturation well below that, at 50–100 kHz. These tubes will also be saturated for a minimum of 5 ms, but the saturation deadtime for detecting signals is more like 6 ms because the counting detector tubes are coupled in triplets.

In Chapter 8 the impact of sample and analyser mosaicity, sample size, and pulse-shaping chopper opening time is studied on the incident detector rates. The parameter space including the sample and analyser mosaicity, sample size, and pulse-shaping chopper opening time, ended with the presentation of the incident detector rates in case of a representative operational scenario. The results demonstrated, that more "everyday" realistic samples give a lower rate challenge, however these samples will still saturate detectors. To overcome challenges caused by these rates, an operational evaluation of a measurement strategy will be the key to the successful operation of this instrument.

The results here show the potential power of source to detector simulation for neutron scattering. These simulations are now possible due to tools recently developed. It is now possible to realistically simulate very complex systems. This models presented in this thesis can now be used to predict experimental conditions from specific proposed samples, i.e. sample size and composition for experiment planning purposes for users.

9.1 Outlook

The method of chaining different simulation tools to carry out full simulation of instruments from source to detectors, as presented in this work is very novel to the neutron scattering field and carries lot of potential. There are cumulative effects in a neutron scattering instrument that are hard to predict by analysing its segments separately, and features that are expected but can not be calculated adequately analytically due to the complexity of the system. The implemented models, and the acquired results have already impacted the instruments, therefore not only their possible future usage but also their current and past application is presented in this section.

Regarding BIFROST, the rate challenge was anticipated even at the proposal of the instrument, however the magnitude of the peak rates exceeded the expectations. The acquired rate values were used at advisory meetings at the European Spallation Source, and the studies helped the instrument team to better understand the challenge of the detector rates. The simulations offered valuable input in finalising the detector requirements before the instrument tendered the procurement of the scattering characterisation system. As a result the detectors are expected to withstand Bragg peak

bursts of 3 ms duration, with peak fluxes up to 10^8 n/s/cm^2, and with time-averaged flux below 10^7 n/s/cm^2 [108]. Careful evaluation of the performance of the detectors is planned, but the foreseen potential solutions to the detector rate challenge include the limitation of sample size and type for the instrument.

Work has been scoped to simulate inelastic signal using the full simulation model of the BIFROST instrument. Results presented in this thesis focused on acquiring coherent elastic (Bragg) and incoherent elastic peaks, however the source of signal to be measured at the instrument is coherent inelastic scattering. The next major release of NCrystal aims to provide a detailed treatment for the inelastic scattering by sampling directly from the scattering kernels generated either computationally or experimentally. This method would provide proper scattering angles and energy transfer, replacing the current approximation of isotropic inelastic scattering, and the scattered neutron energy being sampled from a temperature dependent Maxwellian distribution. Efforts has been made already using the development version of NCrystal, but simulation of weak inelastic signal is time consuming even for the BIFROST instrument. Implementing cross-talk shielding in the Geant4 model of the scattering characterisation system would also give the option to analyse effects of cross-talk on signals and to evaluate shielding strategies.

The implemented simulation tools, and acquired results for the LoKI instrument and the BCS detectors are also in use. The results of the detector rate study were used in the decision making and review processes at the European Spallation Source, e.g, at the "Phase 2" review of LoKI [109], and the generic model of the BCS detectors, presented in this thesis has been expanded into the full simulation model of the LoKI detector system depicted in Figure 9.1 by the LoKI instrument team and the ESS Detector Group [21].

In all detector banks of the LoKI instrument 4 overlapping panels of BCS detectors will be employed, providing sufficient detection efficiency in the wavelengths range of interest, centred around 3 Å. The thickness of the converter layer in the first two panels of detectors will be 0.6 micrometers, significantly thinner that the 1 micron thickness in the last two panels, and the generic simulations presented in this thesis. This solution is expected to mitigate the rate challenge by spreading the detection event among the panels more evenly.

The full simulation model of the LoKI detector system is connected to the Mantid software, where reduction and analysis of simulated data is done. With this connection, the full simulations of the LoKI instrument from the neutron source to the data analysis

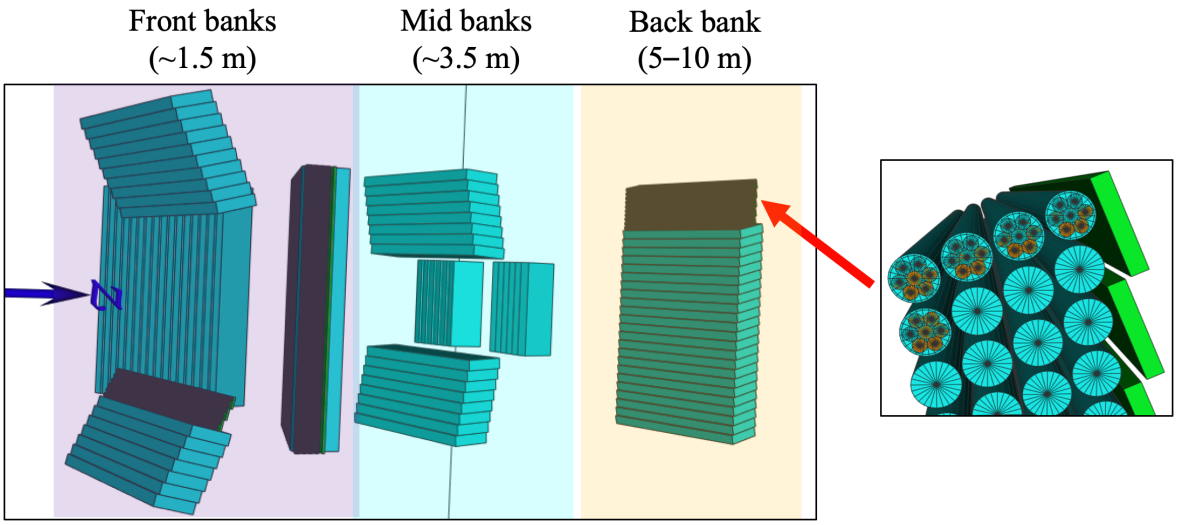

Figure 9.1: Geant4 simulation model of the LoKI detector system with all three detector banks. From [21]

software will be used to facilitate corrections and calibration routines prior to the start of the operation of the instrument.

The complex study of the BCS detector tubes is not exclusively in the interest of the ESS, as this is the first time that such study of the scattering effects of the structural materials of the detector is done, and the producing company intends to reduce secondary scattering inside the detector [110].

Thesis points

The new scientific results of the thesis can be summarised in the following points:

1. I developed a generic Geant4 Monte Carlo simulation model of the Boron-Coated Straws, a solid ^{10}B-enriched boron-carbide converter based, Ar/CO_2-filled neutron detector. I used this model to estimate the incident and detection rates that are anticipated for detectors operated in small-angle neutron scattering instruments planned for the European Spallation Source. I found that for instrument configurations representing realistic operational conditions, the instantaneous detection rate will significantly exceed the rate capability of the detectors having conventional parameters, and therefore they would limit the scientific performance at higher source power. The model has since been adopted as the full simulation model for simulating instrument performance of LoKI instrument at the European Spallation Source. [P0 and P1]

2. With the Geant4 model of a Boron-Coated Straws detector system from thesis point 1 I carried out a simulation study of absorption, activation and efficiency in order to evaluate the detector performance. I found that in the wavelength range of 0.6–11 Å 13–33% of the incident neutrons are absorbed in the detectors without enough energy deposited in the counting gas to trigger detection event. This level of absorption is acceptable for neutron scattering application. However, at smaller wavelengths the fraction of neutrons transmitted through the detector is high (60–27% for 0.6–1.8 Å) and therefore absorbant shielding behind the detector is a must for applications below 5 Å. I demonstrated that the radiation from activated materials will not influence the signal-to-background ratio, or cause limitation due to high doses for maintenance in case of envisaged application at the European Spallation Source. I showed that the detection efficiency of the detector is low, however with application of overlapping layers of detectors, 50–66% detection efficiency is achievable in the 1.8–11 Å wavelength range. [P1 and P2]

3. With the Geant4 model of a Boron-Coated Straws detector system from thesis point 1 I studied the impact of scattering inside the detectors on the signal-

to-background ratio for quantities relevant for different neutron scattering techniques. I found that the fractional scattering (as generally defined as the ratio of the background intensity, and the combined intensity of signal and background) increased with the amount of the material budged, it became the highest at low wavelengths, and significant below the Bragg cut-off. According to the results, the scattering can be considered to remain on acceptable levels for applications such as small-angle neutron scattering, however, may be considerable for applications which are highly sensitive to it such as spectroscopy. I found the application of a polyethylene "afterburner" block placed behind the detector system to noticeably increase the number of neutrons contributing to the signal, however significantly increase the background, therefore the only considerable application field could be homeland security, where position resolution is not a concern. [P2]

4. I elaborated and implemented the first simulation model with complete geometrical coverage of the scattering characterisation system of the BIFROST instrument designed for the European Spallation Source. This is the first application of the special NCrystal pyrolytic graphite material, developed for modelling analysers for neutron scattering applications. I connected this Geant4 model with the existing McStas model of the BIFROST instrument using the MCPL tool and carried out the full simulation of the instrument from source to detector position, which is very novel for neutron scattering. I demonstrated the usefulness of the model by simulating the incident detector rates in case of a common vanadium calibration sample, and matched the acquired energy resolutions of the analyser system to the intended values of the instrument. [P3]

5. I elaborated and implemented a McStas model of the scattering characterisation system of the BIFROST instrument, and used it with the same configurations as the Geant4 model of the system in order to compare the two software packages, and define the highest possible incident detector rates. I demonstrated that Geant4 is more suitable for modelling such a complex geometry, and that the results of McStas and Geant4 are in perfect agreement with the only exception being the transmission where in one case I found a difference of 10%. I found that for instrument configurations and sample parameters representing worst-case conditions the instantaneous rates can be in the range of 1–1.7 GHz for a single detector tube with time-averaged rates of 40–70 MHz. These numbers are well beyond the rate capability of the detector tubes of state of the art, therefore the saturation of the detectors is expected that may last for longer than 6 ms for electronically coupled triplets. [P3]

6. With the joint McStas and Geant4 model of the BIFROST instrument from thesis point 4 I studied the impact of parameters such as sample and analyser mosaicity, sample size, pulse-shaping chopper opening time, and accelerator source power on the incident detector rates for elastic peaks. I demonstrated the impact of the listed parameters, and concluded that in case of a representative operational scenario the incident detector rates are orders of magnitude lower than in the worst-case scenario, however, the values are still beyond the rate capability of the detector tubes. This implies that the detector features of recovery time and high rate tolerance have to be carefully evaluated by measurements to prove that the presumed scientific performance will be provided. [P3]

List of Publications

[**P0**] M. Klausz, "Geant4 based Monte Carlo simulation of neutron detector with boron carbide converter layer". In: Simon, Ferenc (szerk.) Proceedings of the PhD workshop of the Physics Doctoral School at the Faculty of Science Budapest University of Technology and Economics, Budapest, Hungary : BME (2017)

[**P1**] K. Kanaki, M. Klausz, T. Kittelmann, G. Albani, E. Perelli Cippo, A. Jackson, S. Jaksch, T. Nielsen, P. Zagyvai, R. Hall-Wilton, "Detector rates for the Small Angle Neutron Scattering instruments at the European Spallation Source". Journal of Instrumentation 13.07 (2018), P07016.

[**P2**] M. Klausz, K. Kanaki, P. Zagyvai, R.J. Hall-Wilton,"Performance evaluation of the Boron Coated Straws detector with Geant4", Nucl. Instrum. Methods Phys. Res. A 943 (2019), 162463

[**P3**] M. Klausz, K. Kanaki, T. Kittelmann, R. Toft-Petersen, J.O. Birk, M.A. Olsen, P. Zagyvai, R.J. Hall-Wilton, "A simulational study of the indirect geometry neutron spectrometer, BIFROST at the European Spallation Source, from neutron source position to detector position", submitted to J. Appl. Cryst., 2020. arXiv: 2004.00335 [physics.ins-det].

Acknowledgement

First I would like to thank my closest colleague during my PhD work, Kalliopi Kanaki who played the role of a supervisor but could not appear on the cover page merely due to administrative reasons. Without her professional help and life coaching I would not have been able to finish half of this work in the given time.

I would like to thank my supervisor Péter Zagyvai and consultant Richard Hall-Wilton for their invaluable time and effort invested in guiding and helping me. I am particularly grateful to Thomas Kittelmann for the software and IT support that facilitated my work, and for his high standard toward code quality that set an example for me. I would like to give special thanks to Rasmus Toft-Petersen for the BIFROST related essential inputs and useful consultations. I am also grateful to my university consultant Dávid Légrády, who guided me in the same role to my bachelor and masters degree.

I would like to express my eternal gratitude to my family for providing me the everything I needed, that allowed me to concentrate on my studies. I would also like to mention my girlfriend and friends who supported and upheld me when I most needed it.

Last but not least, I am thankful to both the Centre for Energy Research (MTA EK) and the European Spallation Source for providing a great PhD topic and all the necessary background, and also to the DMSC Computing Centre which provided the computing resources for the simulations.

This work has been supported by the In-Kind collaboration between ESS ERIC (contract number: NIK5.4 #10 [ESS]) and the Hungarian Academy of Sciences, Centre for Energy Research.

Appendix A – Verification of simulation results

Verification of simulation models is essential in order to gain confidence in the validity of the results acquired with them. Using an open framework with validated simulation tools such as the simulation framework of the ESS Detector Group is greatly beneficial in this task, as it not only enhances the capabilities of the Geant4 simulation tool for simulation of detectors, but also ensures that the models are easier to validate and results are more reliable. This framework also supports the use of public repositories for the models and supplementary codes. This kind of sharing eases the effort of simulation work by code reuse, and increases the reproducibility of studies. It also mitigates the problem, that most "common knowledge" is often not published in the neutrons scattering community. For the same reason, in order to increase accessibility, the results presented in this thesis are published with open access.

Although direct comparison of simulation results to measured data in not possible until after the instruments are built, comparison with analytical calculations and measurements under similar conditions is possible, as well as cross-validation with different simulation tools or models. Such validations are already presented throughout the thesis, but additional verifications are provided in this appendix for both the BCS detector model and the BIFROST scattering characterisation system models.

Boron-Coated Straws

All results produced with the BCS detector model are well understood and consistent. The wavelength dependence of the efficiency presented in Section 4.1 is physically reasonable, and for multiple layers of detectors the consequent effect of the hardening of the neutron spectra is apparent, as demonstrated in Section 3.3. The analytical estimation of the absorption in the mechanical materials of the detectors, presented in Section 4.2 shows good agreement with the simulations. The trends in the scattering effect experienced for different types and amount of materials, and different

neutron wavelengths are also physically reasonable and consistent, as demonstrated in Section 5.2.

The additional verification of the BCS detector model presented in this appendix concerns the pulse-height spectra, detection to conversion ratio, and detection efficiency.

As explained in Section 3.2 and further discussed in Section 4.1, a detection event is recorded in the simulations if the conversion products of a neutron deposit more energy in the counting gas than a preset threshold applied to mimic discrimination of the gamma background. The underlying physical process in which the conversion products are created in the converter layer is the ^{10}B(n,α)^{7}Li reaction, detailed in Equation 1.2 and discussed in Section 1.2.1.

The simulated pulse-height spectra of the BCS detector is depicted in Figure A.1 and A.2 on linear and logarithmic scale respectively. In these figures the pulse-height spectra is shown for the conversion products (^{7}Li and α-particle) and the gammas from the de-excitation of ^{7}Li* both separately and cumulatively. The later is the measurable pulse-height spectra.

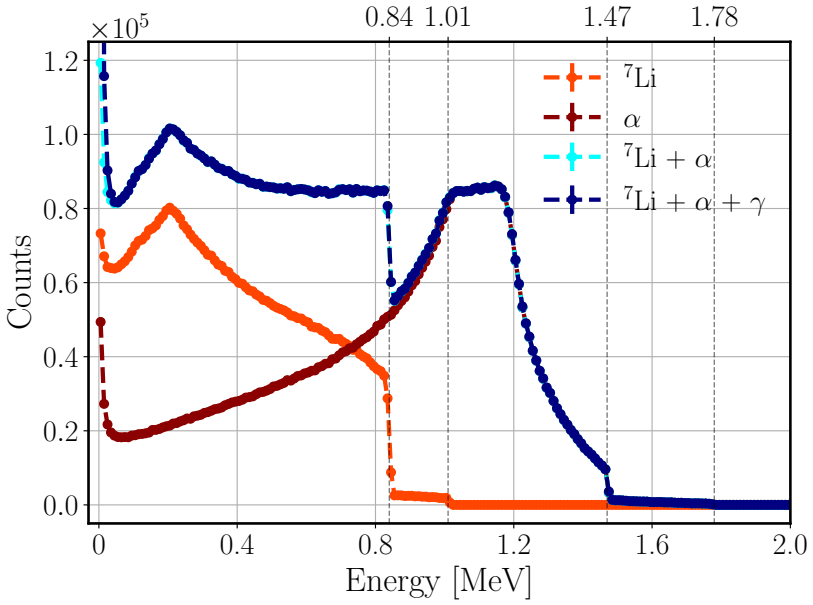

Figure A.1: Pulse-height spectrum of the BCS detector on linear scale for ^{7}Li, α-particle and γ together and separately from simulation with 1.8 Å neutrons. The dashed lines only connect the markers.

As expected, significant drop is apparent in the spectrum of the ^{7}Li and the α-particle at the energies corresponding to the initial kinetic energy of these particles in the main (∼94% probability) reaction branch (E_{Li}=0.84 MeV and E_{α}=1.47 MeV). Also, their spectrum end at the energies corresponding to their initial kinetic energy in the

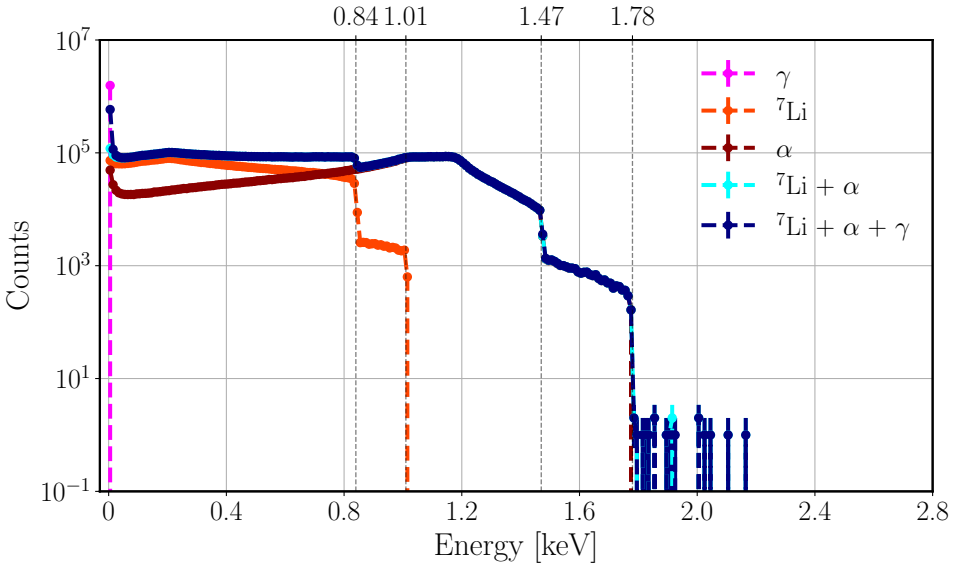

Figure A.2: Pulse-height spectrum of the BCS detector on logarithmic scale for ^{7}Li, α-particle and γ together and separately from simulation with 1.8 Å neutrons. The dashed lines only connect the markers.

less probable (∼6% probability) reaction branch (E_{Li}=1.01 MeV and E_{α}=1.78 MeV), due to the higher kinetic energies. These energy limits are reached in cases when one of the particles exit the converter layer without losing energy, and then deposit all its energy in the counting gas. The quite rare events when more than 1.78 MeV energy is deposited can happen only if both conversion products escape the converter layer and deposit energy in the counting gas, that is possible despite their opposite direction in case of scattering inside the converter layer. Accordingly, these events appear only in the cumulative spectrum. The gammas from the de-excitation of ^{7}Li* in the main reaction branch contribute <10 keV, demonstrating the low gamma sensitivity of the detector.

The shape of pulse-height spectra is in accordance with expectations based on analytical calculations, measurements, and simulations of ^{10}B-based thin film neutron converters and similar detector geometries [93, 111, 112]. More detailed explanation of the shape of the pulse-height spectra for ^{10}B-based detectors where the particle ranges ($R_{Li(0.84\ MeV)}$=1.7 μm and $R_{\alpha(1.47\ MeV)}$=3.4 μm) are longer than the thickness of the converter layer (d=1 μm) is given here [93].

The referenced study do not take into account the loss of signal amplitude in cases when conversion products hit the wall of the detector before depositing all their kinetic energy, called wall effect, that is relevant for detectors with such small diameters. To highlight this effect, the pulse-height spectra is also depicted for double-sized straws with the same 1 μm converter layer thickness in Figure A.3, where energies above

∼1.2 MeV are visibly more probable. The change of the pulse-height spectra due to the wall effect is in accordance with the study of wall effect in similar detector geometries [113].

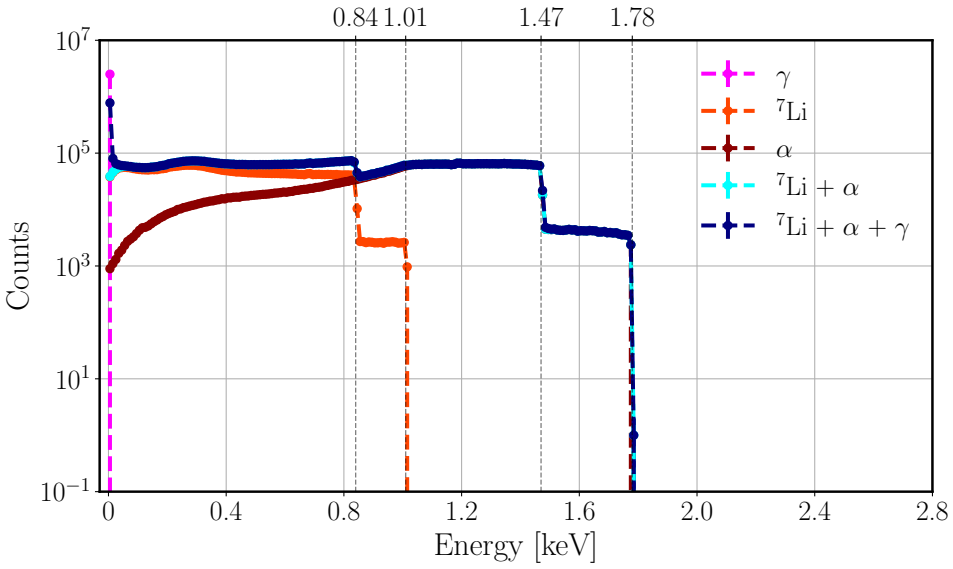

Figure A.3: Pulse-height spectrum of double-sized BCS detector on logarithmic scale for ^{7}Li, α-particle and γ together and separately from simulation with 1.8 Å neutrons. The dashed lines only connect the markers.

As stated in Section 1.2.1, it is claimed that for 1 μm of B_4C, one of the two charged conversion products has a 78% probability to escape the converter and ionise the counting gas in the BCS straw [43]. This value is the theoretical maximum for the detection to conversion ratio, with no energy threshold, that gives an upper limit for the detection efficiency. The results show that in this case at least one of the ^{7}Li and α-particle escape the converter layer and deposit energy in the counting gas with 77.7% probability, which agrees within rounding error with the published value. Technically, in this case the de-excitation gammas could also trigger detection events that would increase the detection to conversion ratio to 81.3%, however it is only theoretical due to the presence of radiation background that always necessitates energy threshold for measurements.

Throughout the thesis the applied threshold is 120 keV, as stated in Section 4.1, where it is also mentioned that this results in a detection to conversion ratio of 70%, regardless of the wavelength of the converted neutrons, due to the small thickness of the B_4C layer. As a matter of fact, weak neutron wavelength dependence of the detection to conversion ratio is observable, as demonstrated in Figure A.4 showing the energy threshold dependence of the detection to conversion ratio for neutron wavelengths between 0.6–11 Å.

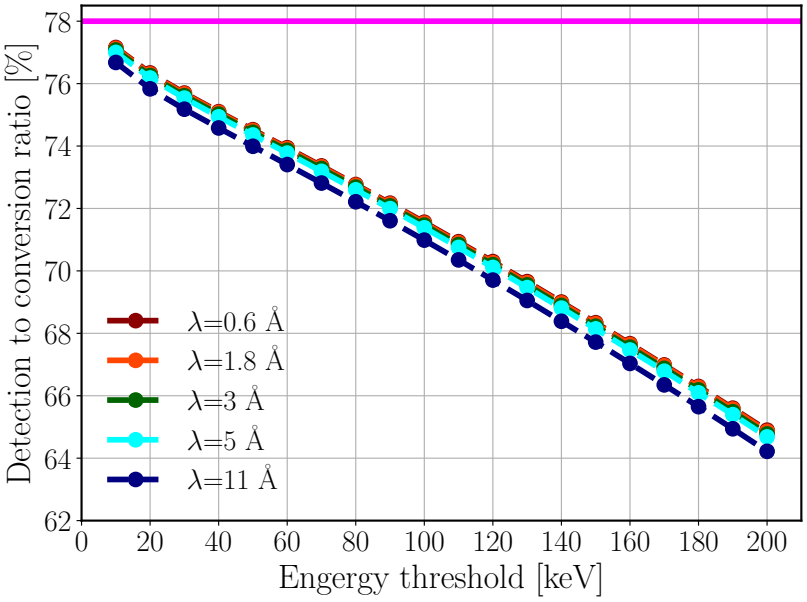

Figure A.4: Detection to conversion ratio as a function of the applied energy threshold from different neutron wavelengths. The magenta line marks the claimed theoretical maximum of detection to conversion ratio (78%). The dashed line only connects the markers.

The difference in the detection to conversion ratio for different neutron wavelengths is small but consistent, with generally higher values for higher wavelengths. For the applied threshold of 120 keV the detection to conversion ratio is within the narrow range of 69.7–70.3%. The energy threshold dependence of the detection to conversion ratio on the other hand is much more significant, and appears to be practically linear in the observed energy range. The energy threshold dependence of the detection to conversion ratio translates directly to the detection efficiency, where such dependence is expected [111], and the experienced linear correlation is in accordance with study of similar detector geometry where the observed total counts depended linearly on the threshold value [113].

The detection efficiency of the BCS detector is examined Section 4.1 for multiple neutron wavelengths and with different number of overlapping panels. The results acquired for the 5 panel arrangement are compared to one simulated and two measured datasets corresponding to similar detector arrangements, depicted in Figure A.5.

Efficiency values in “Measurement 2” are lower than in all other datasets, consistently ∼10% lower than values from the Geant4 simulations. The accordance is better with the “Measurement 1” and “MCNP simulation” datasets, where the difference is <5% in the most relevant 1.8–5 Å wavelength region and <8% for 11 Å.

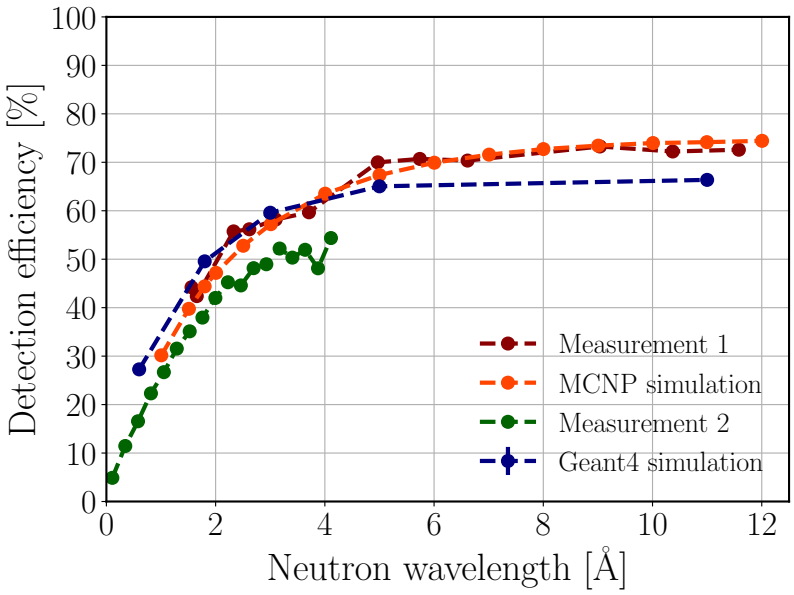

Figure A.5: Comparison of detection efficiency for 5 panel BCS detector arrangement from different simulations and measurements. The legends denote the following datasets: "Measurement 1" and "MCNP simulation" [114], "Measurement 2" [88]. "Geant4 simulations" refer to results presented in this thesis. The dashed lines only connect the markers.

BIFROST scattering characterisation system

All results produced with the Geant4 model of the BIFROST scattering characterisation system are physically reasonable and consistent. The neutron energies selected by the analysers, and their energy resolutions are in accordance with the description of the instrument, as presented in Section 6.2. The cross-validation with the McStas simulation model in Sections 7.3 and 7.4 shows perfect agreement with the only exception found in the transmission of the sample that do not affect the rate results. The tendencies in the incident detector rates experienced in the parameter study presented in Chapter 8 including sample and analyser mosaicity, sample size, and pulse-shaping chopper opening time are also physically reasonable and consistent.

In this appendix the simulated incident detector rate for the 5 meV detector triplet with vanadium sample presented in Section 6.2 is validated by analytical calculations, and an estimate based on measured data from a triple-axis spectrometer.

Vanadium is a common calibration sample that is close to an ideal isotropic incoherent elastic scatterer. In this analytical calculation, first the fraction of neutrons scattered on the sample is calculated for the relevant 4.9–5.1 meV energy range, by estimating the fraction of absorption and transmission through the sample.

Using Equation 4.2 and Equation 4.3, the fraction of absorption can be calculated for a given sample thickness, density and neutron energy. Assuming uniform parallel

beam of neutrons, the average path length through a cylindrical sample with a radius r is $l = r^2 \cdot \pi/(2 \cdot r)$. The density of vanadium in the simulations is 6.118 g/cm^3. For 5 meV neutron energy (4.04 Å), the microscopic absorption cross-section is σ_a=11.5 b as demonstrated in Figure A.6.

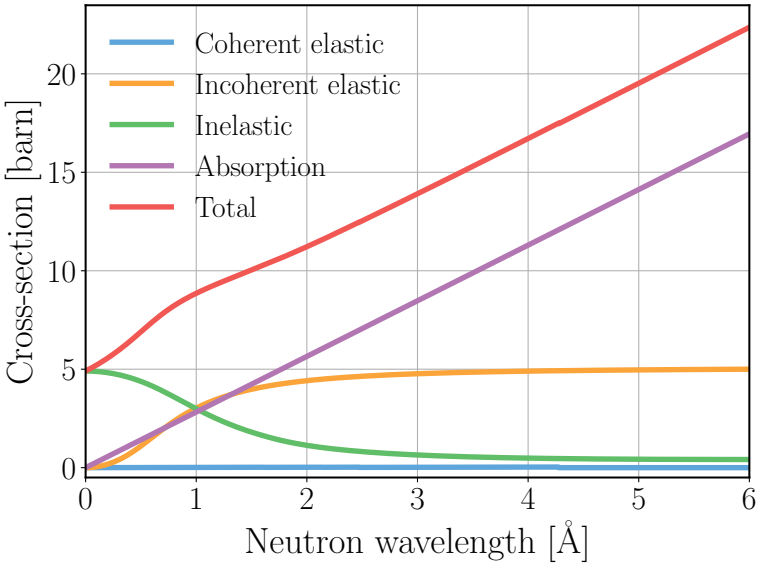

Figure A.6: Cross-sections of vanadium from the NCrystal library [75, 96].

Inserting these values into the formulae for a sample with a diameter of 1.5 cm, the result shows that 62% of the 5 meV incident neutrons are expected to be absorbed in the sample. The numbers from the simulation show good agreement with this result with 59% of the incident neutrons in the energy range of 4.9–5.1 meV absorbed given the 9.288 $\cdot 10^8$ Hz incident rate and 5.514 $\cdot 10^8$ Hz absorption rate.

The fraction of transmission through the sample can be calculated similarly, using the total microscopic cross-section of σ_t=16.8 b for 5 meV neutron energy. Based on this calculation 24% of the 5 meV incident neutrons are expected to be transmitted through the sample. In the simulation the transmission rate of 2.385 $\cdot 10^8$ Hz in the energy range of 4.9–5.1 meV gives only slightly higher 26% transmission.

According to the analytical calculations the remaining 14% of the incident neutrons on the sample are expected to be scattered. Assuming isotropic scattering, the incident rate on a set of analysers can be estimated knowing the solid angle coverage. For a symmetric Q-channel the 5 meV analyser set consists of nine blades of 1.35 cm height and 18.16 cm width. Assuming 37.067° rotation angle and 1.623 m distance from a point-like sample for all nine analyser blades, the covered solid angle is Ω=0.000401 sr. Using the 9.288$\cdot 10^8$ Hz incident neutron rate on the sample in the energy range of 4.9–5.1 meV, the expected neutron rate on the analysers in this energy range is 9.288$\cdot 10^8 \cdot$0.14$\cdot$0.000401$\approx$52 kHz. The simulated incident neutron rate in on the

analysers shows perfect agreement with 51±2 kHz. According to the simulation ∼25% of these neutrons are transmitted through the analysers due to the divergence of the beam and the wide energy range, and ∼68% of the selected neutrons reach the detector triplet, resulting in the 26±2 kHz incident detector rate presented in Section 6.2.

The incident detector rate anticipated for BIFROST can also be estimated based on measured data from similar instruments. The data serving as basis for the estimate is measured during the instrument upgrade of the cold neutron triple-axis spectrometer FLEXX at the BER-II reactor [115]. In order to characterise the gains from the upgrade, measurement of the incident neutron rate at the sample position is carried out, as well as measurement of detected intensity from vanadium sample.

Knowing the detection rate ($D_{det,FLEXX}(E)$) and the incident rate on the vanadium sample ($S_{FLEXX}(E)$) for a specific neutron energy (E), an estimation can be given for the incident detector rate at BIFROST ($D_{inc,BIFROST}(E)$) for a specific incident rate on the sample ($S_{BIFROST}(E)$), using the formula in Equation A.1, taking into account the detection efficiency ($\epsilon_{det,FLEXX}(E)$), and the ratio of the solid angle coverage of the two analyser systems ($R_{solidangle}$).

$$D_{inc,BIFROST}(E) = \frac{D_{det,FLEXX}(E)}{\epsilon_{det,FLEXX}(E)} \cdot \frac{S_{BIFROST}(E)}{S_{FLEXX}(E)} \cdot R_{solidangle}. \tag{A.1}$$

According to the measurements with a vanadium rod with 1 cm diameter, the detection rate for 5 meV (incident wave vector k_i=1.55 Å^{-1}) is $D_{det,FLEXX}$=585 Hz. The efficiency of ^{3}He detector tubes for this energy is approximately $\epsilon_{det,FLEXX}$=0.8 [114]. The fitted energy resolution for this energy is reported to be 0.155 meV, that agrees with the simulated energy resolution of the 5 meV detector triplet for BIFROST (see Table 6.3). The incident flux at 5 meV on the sample is ∼3·10^7 n/s/cm^2, that results in an integrated intensity of S_{FLEXX}=8·10^7 Hz.

The analyser system at FLEXX measurement consists of 15 1×10 cm pyrolytic graphite blades placed 1.4 m from the sample position. For 5 meV neutrons, assuming 37.067° rotation angle for all analyser blades and point-like sample, the solid angle covered by the analysers is Ω=0.000461 sr. The resulting ratio of the BIFROST and FLEXX analyser system solid angle coverage is $R_{solidangle}$=1.8.

From simulations with 5 MW source power, the neutron intensity at BIFROST on a vanadium sample with 1 cm diameter and 1.5 cm height in the relevant energy range of 4.9–5.1 meV is $S_{BIFROST}$=6.5·10^8 Hz. Inserting these values into Equation A.1 gives an estimate of $D_{inc,BIFROST}$=11 kHz, that is 39% lower than the simulated 18±2 kHz for the 5 meV detector triplet. Given that it is a rough estimation, the result is acceptable and supports the validity of the simulation model.

Appendix B – Signal limits

In chapter 5 qualitative and quantitative analysis of the scattering effects inside a Boron-Coated Straws detector system is presented, investigating the effects of scattering on quantities relevant for different neutron scattering techniques. The quantification of scattering is performed by separating detection events into signal and background based on defining signal limits for each quantity of interest. Figures demonstrating visually the defined signal limits for some of these quantities are presented in section 5.1. In this appendix figures similar to those are presented for the remaining quantities.

Figures B.1–B.2 demonstrate the signal limits defined for $\delta\Theta$ and $\delta\Phi$ (similarly as Figures 5.2–5.3 demonstrated the limits for δX and δY). In addition, as an example, Figures B.3–B.5 depict the signal limits for δTOF, $\delta\lambda$ and δQ for one of the wavelengths of interest.

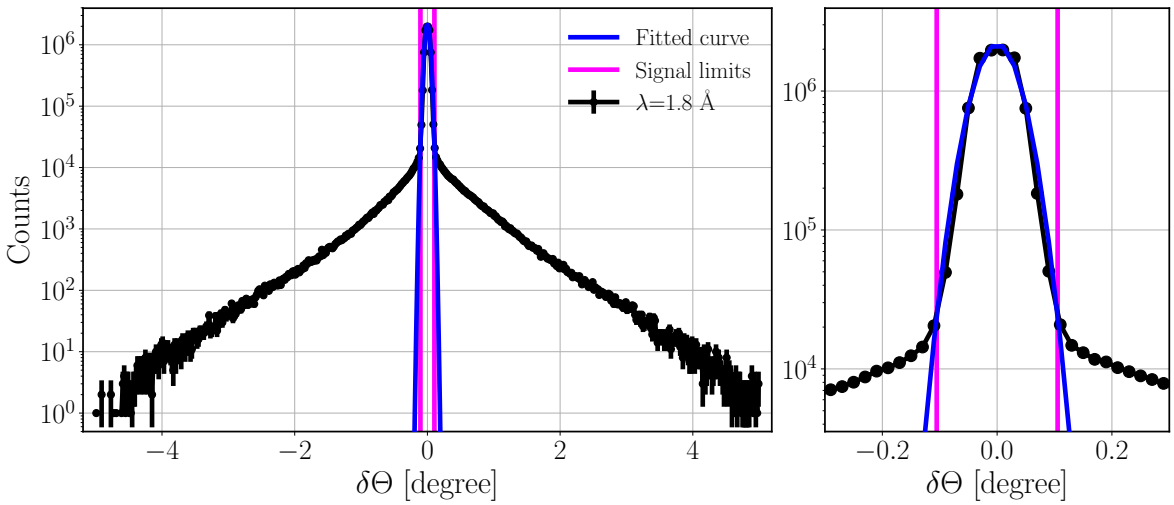

Figure B.1: Finding the limits for signal and background separation for $\delta\Theta$ with a 1.8 Å monoenergetic beam. The figure on the right shows an enlarged view of the centre part of the figure on the left. The lines are only joining the points.

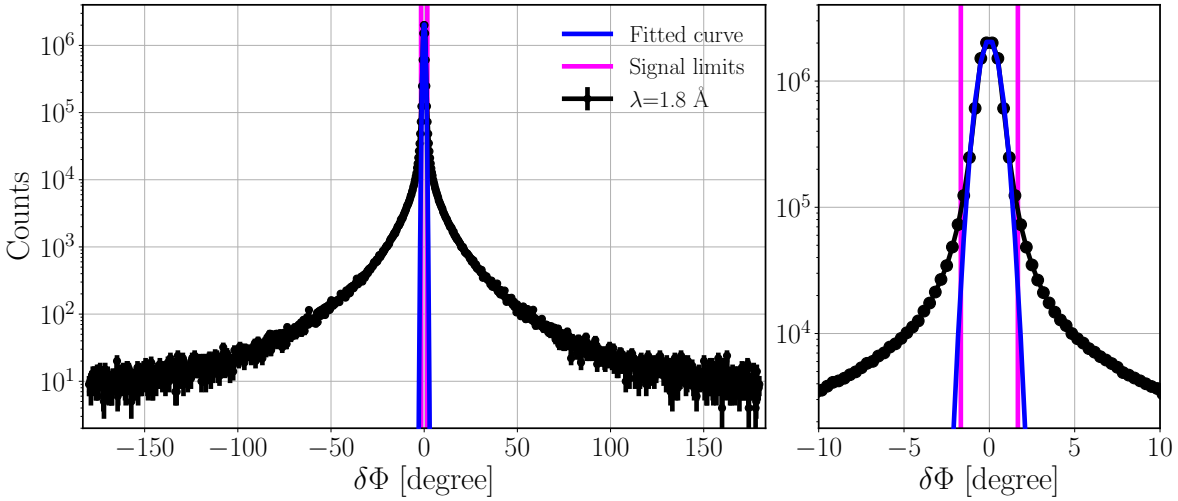

Figure B.2: Finding the limits for signal and background separation for $\delta\Phi$ with a 1.8 Å monoenergetic beam. The figure on the right shows an enlarged view of the centre part of the figure on the left. The lines are only joining the points.

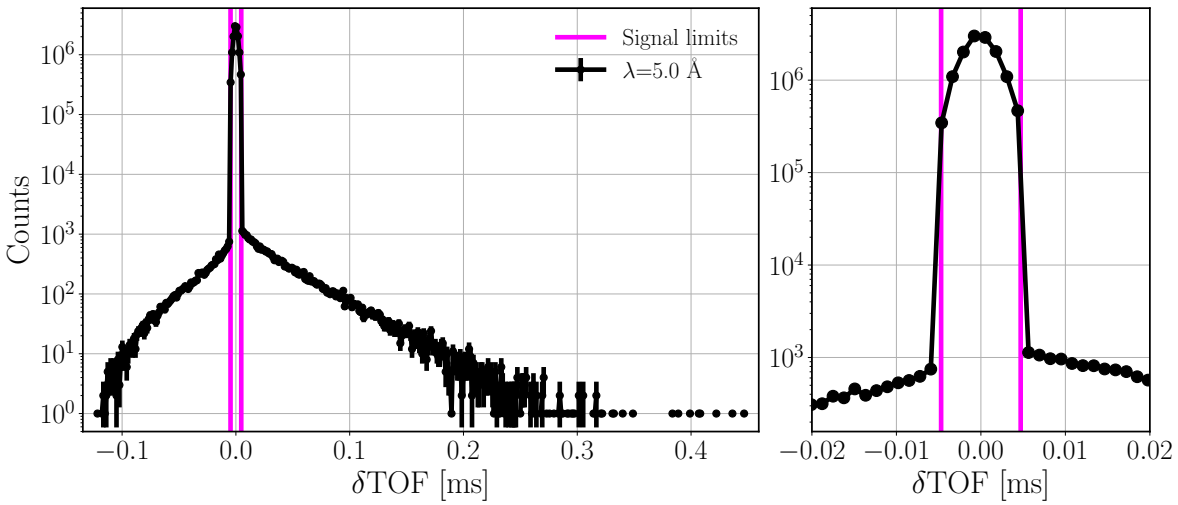

Figure B.3: Finding the limits for signal and background separation for δTOF with a 5 Å monoenergetic beam. The figure on the right shows an enlarged view of the centre part of the figure on the left. The lines are only joining the points.

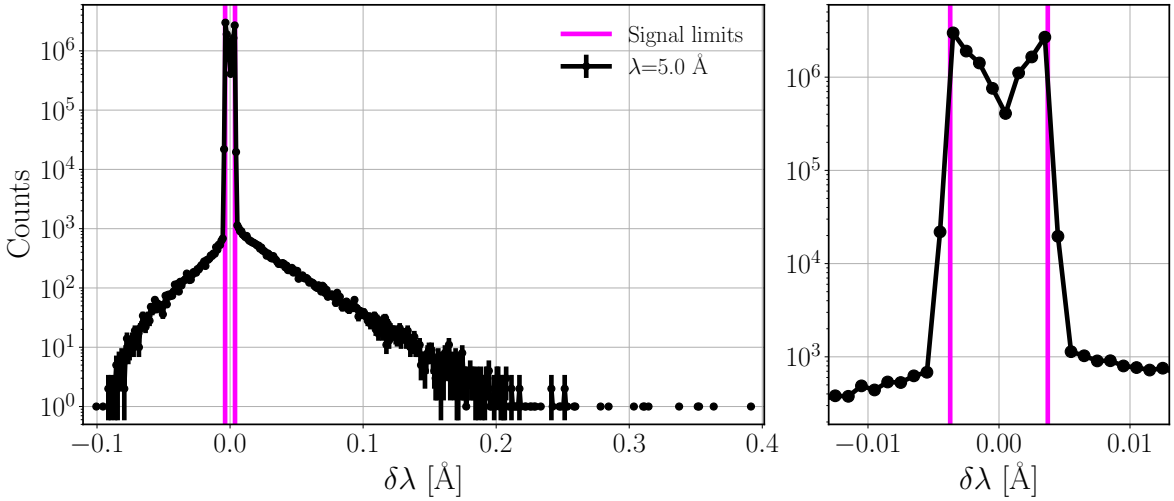

Figure B.4: Finding the limits for signal and background separation for $\delta\lambda$ with a 5 Å monoenergetic beam. The limits are derived from the straw inner radius, using Eq. 5.3. The figure on the right shows an enlarged view of the centre part of the figure on the left. The lines are only joining the points.

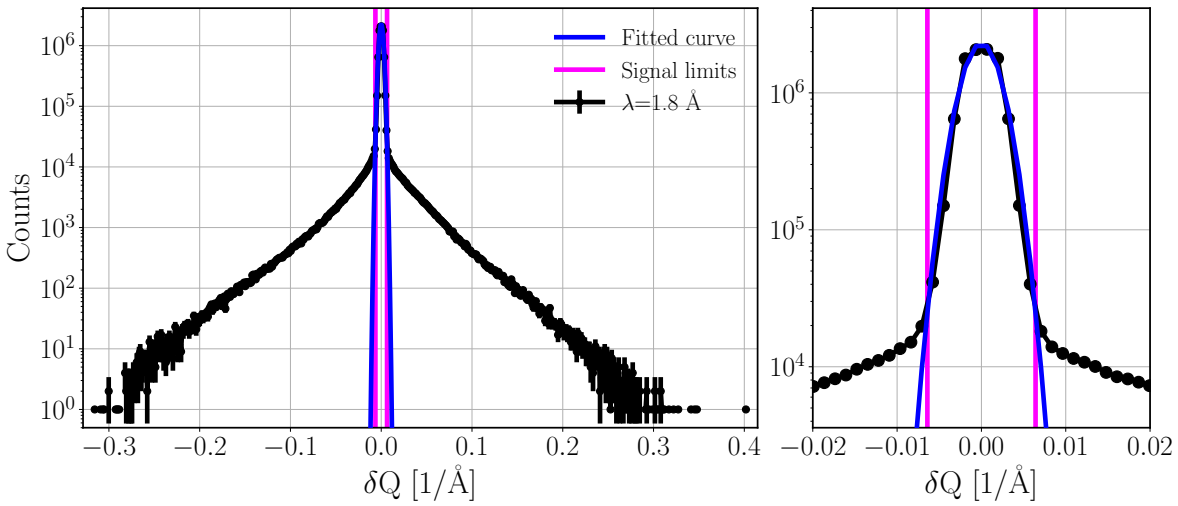

Figure B.5: Finding the limits for signal and background separation for δQ with a 1.8 Å monoenergetic beam. The figure on the right shows an enlarged view of the centre part of the figure on the left. The lines are only joining the points.

Bibliography

[1] S. Peggs et al. *ESS Technical Design Report, ESS 2013-001*. 2013. URL: https://europeanspallationsource.se/sites/default/files/downloads/2017/09/TDR_online_ver_all.pdf.

[2] R. Garoby et al. "The European Spallation Source Design". *Physica Scripta* 93.1 (2017), p. 014001. DOI: 10.1088/1402-4896/aa9bff.

[3] K. H. Andersen et al. "The instrument suite of the European Spallation Source". *Nucl. Instrum. Methods Phys. Res. A* 957 (2020), p. 163402. ISSN: 0168-9002. DOI: 10.1016/j.nima.2020.163402.

[4] O. Kirstein et al. "Neutron Position Sensitive Detectors for the ESS". *PoS* Vertex2014 (2014), p. 029. DOI: 10.22323/1.227.0029.

[5] A. J. Jackson et al. "LoKI - A Broad Band High Flux SANS Instrument for the ESS". *Proceedings ICANS XXI* (2015). DOI: 10.11484/jaea-conf-2015-002.

[6] A. J. Jackson et al. *LoKI- A broad-band SANS instrument*. 2012. URL: https://europeanspallationsource.se/sites/default/files/files/document/2017-09/loki_proposal_stc_sept2013.pdf.

[7] H. Ronnow et al. *BIFROST Instrument proposal*. 2014. URL: https://ess-public-legacy.esss.se/sites/default/files/bifrost_proposal_may_2014.pdf.

[8] P. G. Freeman et al. "CAMEA ESS – The continuous angle multi-energy analysis indirect geometry spectrometer for the European Spallation Source". *EPJ Web Conf.* 83 (2015), p. 03005. DOI: 10.1051/epjconf/20158303005.

[9] J. L. Lacy et al. "Boron-coated straw detectors: A novel approach for helium-3 neutron detector replacement". In: *IEEE Nuclear Science Symposuim Medical Imaging Conference*. 2010, pp. 3971–3975. DOI: 10.1109/nssmic.2010.5874561.

[10] J. L. Lacy et al. "The Evolution of Neutron Straw Detector Applications in Homeland Security". *IEEE Transactions on Nuclear Science* 60.2 (2013), pp. 1140–1146. ISSN: 0018-9499. DOI: 10.1109/TNS.2013.2248166.

[11] H. Danared et al. "The ESS Design: Accelerator". *Physica Scripta* 93.1 (2017), pp. 6–65. DOI: 10.1088/1402-4896/aa9bff.

[12] K. H. Andersen et al. "Optimization of moderators and beam extraction at the ESS". *Journal of Applied Crystallography* 51.2 (2018), pp. 264–281. DOI: 10.1107/S1600576718002406.

[13] L. Zanini et al. "Design of the cold and thermal neutron moderators for the European Spallation Source". *Nucl. Instrum. Methods Phys. Res. A* 925 (2019), pp. 33–52. ISSN: 0168-9002. DOI: 10.1016/j.nima.2019.01.003.

[14] F. Mezei et al. "Low dimensional neutron moderators for enhanced source brightness". *Journal of Neutron Research* 17 (2014), pp. 101–105. DOI: 10.3233/JNR-140013.

[15] D. B. Pelowitz et al. *MCNPX 2.7.0 Extensions*. Tech. rep. LA-UR-11-02295. Los Alamos National Laboratory, 2011. DOI: 10.2172/1058045.

[16] L. A. Feigin and D. I. Svergun. *Structure Analysis by Small-Angle X-Ray and Neutron Scattering*. Springer, 1987. DOI: 10.1007/978-1-4757-6624-0.

[17] B. T. M. Willis and C. J. Carlile. *Experimental Neutron Scattering*. OUP Oxford, 2009. ISBN: 9780198519706.

[18] S. Jaksch et al. "Concept for a time-of-flight Small Angle Neutron Scattering instrument at the European Spallation Source". *Nucl. Instrum. Methods Phys. Res. A* 762 (2014), pp. 22–30. ISSN: 0168-9002. DOI: 10.1016/j.nima.2014.04.024.

[19] S. Jaksch. "Considerations about chopper configuration at a time-of-flight SANS instrument at a spallation source". *Nucl. Instrum. Methods Phys. Res. A* 835 (2016), pp. 61–65. ISSN: 0168-9002. DOI: 10.1016/j.nima.2016.07.041.

[20] LoKI CAD view. 2017. URL: https://indico.esss.lu.se/event/831/attachments/6361/9051/LoKI_CAD_Views.pdf.

[21] J. Houston et al. *Combining Simulation and Measurement to Understand Complex Detector Geometries*. International Collaboration on Advanced Neutron Sources (ICANS XXIII). 2019. URL: https://conference.sns.gov/event/138/contributions/407/contribution.pdf.

[22] A. Cho. "Helium-3 Shortage Could Put Freeze On Low-Temperature Research". *Science* 326.5954 (2009), pp. 778–779. DOI: 10.1126/science.326_778.

[23] T. M. Persons and G. Aloise. "Technology Assessment: Neutron Detectors: Alternatives to Using Helium-3" (2011). GAO-11-753.

[24] K. Zeitelhack. "Search for alternative techniques to Helium-3 based detectors for neutron scattering applications". *Neutron News* 23.4 (2012), pp. 10–13. DOI: 10.1080/10448632.2012.725325.

[25] I. Stefanescu et al. "A ^{10}B-based neutron detector with stacked MultiWire Proportional Counters and macrostructured cathodes". *J. Instrum.* 8.12 (2013), P12003–P12003. DOI: 10.1088/1748-0221/8/12/p12003.

[26] A. Khaplanov et al. "Multi-Grid Detector for Neutron Spectroscopy: Results Obtained on Time-of-Flight Spectrometer CNCS". *J. Instrum.* 12 (2017), P04030. DOI: 10.1088/1748-0221/12/04/P04030.

[27] A. Muraro et al. "Performance of the high-efficiency thermal neutron BAND-GEM detector". *Prog. Theor. Exp. Phys.* 023H01 (2018). DOI: 10.1093/ptep/pty005.

[28] L. M. S. Margato and A. Morozov. "Boron-10 lined RPCs for sub-millimeter resolution thermal neutron detectors: conceptual design and performance considerations". *J. Instrum.* 13.08 (2018), P08007–P08007. DOI: 10.1088/1748-0221/13/08/p08007.

[29] L. M. S. Margato et al. "Boron-10 lined RPCs for sub-millimeter resolution thermal neutron detectors: Feasibility study in a thermal neutron beam". *J. Instrum.* 14.01 (2019), P01017–P01017. DOI: 10.1088/1748-0221/14/01/p01017.

[30] F. Piscitelli and others. "Characterization of the Multi-Blade 10B-based detector at the CRISP reflectometer at ISIS for neutron reflectometry at ESS". *J. Instrum.* 13 (2018), P05009.

[31] R. Qiao et al. "Charge reconstruction study of the DAMPE Silicon-Tungsten Tracker with ion beams". *Nucl. Instrum. Methods Phys. Res. A* 886 (May 2017). DOI: 10.1016/j.nima.2018.01.007.

[32] A. Mazzone et al. "GEANT4 simulations of a novel 3 He-free thermalization neutron detector". *Nucl. Instrum. Methods Phys. Res. A* 889 (Feb. 2018). DOI: 10.1016/j.nima.2018.02.011.

[33] A. Kok et al. "Silicon sensors with pyramidal structures for neutron imaging". *J. Instrum.* 9.04 (2014), pp. C04011–C04011. DOI: 10.1088/1748-0221/9/04/c04011.

[34] G. J. Sykora et al. "ZnO:Zn/6LiF scintillator - A low afterglow alternative to ZnS:Ag/6LiF for thermal neutron detection". *Nucl. Instrum. Methods Phys. Res. A* 883 (Mar. 2018), pp. 75–82. DOI: 10.1016/j.nima.2017.11.052.

[35] G. J. Sykora et al. "Large area wavelength shifting fibre thermal neutron detectors using 64 channel flat panel PMTs". In: *2015 IEEE Nuclear Science Symposium and Medical Imaging Conference (NSS/MIC)*. 2015, pp. 1–4. DOI: 10.1109/NSSMIC.2015.7581838.

[36] C. L. Wang et al. "Wavelength-shifting-fiber scintillation detectors for thermal neutron imaging at SNS". In: *2011 IEEE Nuclear Science Symposium Conference Record*. 2011, pp. 4877–4882. DOI: 10.1109/NSSMIC.2011.6152489.

[37] S. Jaksch et al. "Recent Developments SoNDe High-Flux Detector Project". *Proc. Int. Conf. Neutron Optics (NOP2017)* 22 (2018), p. 011019. DOI: 10.7566/JPSCP.22.011019.

[38] S. Jaksch et al. *Cumulative Reports of the SoNDe Project July 2017*. 2017. arXiv: 1707.08679 [physics.ins-det].

[39] M. Katagiri. "Neutron Detectors with Scintillators Using ZnS: Ag Phosphor: Development Summary". *IEEE NSS, Anaheim* He-2-2 (2012).

[40] K. Sakasai et al. "Development of neutron detector for engineering materials diffractometer at J-PARC". *Nucl. Instrum. Methods Phys. Res. A* 600.1 (2009), pp. 157–160. ISSN: 0168-9002. DOI: 10.1016/j.nima.2008.11.023.

[41] Z. W. Bell. "Thermal Neutron Detection System Based on ZnS/LiF Scintillator". *Proceedings of IEEE NSS conference, Anaheim* He-2-1 (2012).

[42] Inc. Proportional Technologies. URL: https://proportionaltech.myshopify.com/.

[43] J. L. Lacy et al. "Initial performance of sealed straw modules for large area neutron science detectors". In: *2011 IEEE Nuclear Science Symposium Conference Record*. 2011, pp. 431–435. DOI: 10.1109/NSSMIC.2011.6154533.

[44] F. Sauli. *Gaseous Radiation Detectors: Fundamentals and Applications*. Cambridge University Press, 2014. ISBN: 110704301. DOI: 10.1017/CBO9781107337701.

[45] Z. Xie et al. "Experimental study of boron-coated straws with a neutron source". *Nucl. Instrum. Methods Phys. Res. A* 888 (2018), pp. 235–239. ISSN: 0168-9002. DOI: 10.1016/j.nima.2018.01.090.

[46] H. Yu et al. "A multiplex readout method for position sensitive boron coated straw neutron detector". *Nucl. Instrum. Methods Phys. Res. A* 797 (2015), pp. 324–329. ISSN: 0168-9002. DOI: 10.1016/j.nima.2015.05.038.

[47] W. Lohstroh et al. *ESS Instrument Construction Proposal C-SPEC – Cold chopper spectrometer*. 2013. URL: https://ess-public-legacy.esss.se/sites/default/files/c-spec_proposal_0.pdf.

[48] T. Brückel et al. *ESS Instrument Construction Proposal T-REX: A Time-of-flight Reciprocal space Explorer*. 2015. URL: https://indico.esss.lu.se/event/739/attachments/5717/7971/t-rex_proposal.pdf.

[49] M. Zanetti et al. "Neutronic developments on TOSCA and VESPA: Progress to date". *Physica B: Condensed Matter* 562 (2019), pp. 107–111. ISSN: 0921-4526. DOI: 10.1016/j.physb.2018.12.034.

[50] N. Tsapatsaris et al. "Conceptual design of the time-of-flight backscattering spectrometer, MIRACLES, at the European Spallation Source". *Review of Scientific Instruments* 87.8 (2016), p. 085118. DOI: 10.1063/1.4961569.

[51] S. Holm-Dahlin et al. "Optimization of Performance, Price, and Background of Long Neutron Guides for European Spallation Source". *Quantum Beam Science* 3.3 (2019), p. 16. ISSN: 2412-382X. DOI: 10.3390/qubs3030016.

[52] BIFROST Instrument at ESS. URL: https://europeanspallationsource.se/instruments/bifrost.

[53] M. Marko et al. "Prototype of the novel CAMEA concept – A backend for neutron spectrometers". *Review of Scientific Instruments* 89 (Jan. 2018), p. 015105. DOI: 10.1063/1.5018233.

[54] F. Groitl et al. "CAMEA – A novel multiplexing analyzer for neutron spectroscopy". *Review of Scientific Instruments* 87.3 (2016), p. 035109. DOI: 10.1063/1.4943208.

[55] F. Groitl et al. "A combined radial collimator and cooled beryllium filter for neutron scattering". *Nucl. Instrum. Methods Phys. Res. A* 819 (2016), pp. 99–103. ISSN: 0168-9002. DOI: 10.1016/j.nima.2016.02.056.

[56] D. F. R. Mildner, M. Arif, and S. A. Werner. "Neutron transmission through pyrolytic graphite monochromators". *Journal of Applied Crystallography* 34.3 (2001), pp. 258–262. DOI: 10.1107/S0021889801002254.

[57] M. Skoulatos, K. Habicht, and K. Lieutenant. "Improving energy resolution on neutron monochromator arrays". *Journal of Physics: Conference Series* 340 (2012), p. 012019. DOI: 10.1088/1742-6596/340/1/012019.

[58] J. O. Birk et al. "Prismatic analyser concept for neutron spectrometers". *Review of Scientific Instruments* 85.11 (2014), p. 113908. DOI: 10.1063/1.4901160.

[59] G. F. Knoll. *Radiation detection and measurement; 4th ed.* New York, NY: Wiley, 2010. URL: https://cds.cern.ch/record/1300754.

[60] I. Lux and L. Koblinger. *Monte Carlo Particle Transport Methods: Neutron and Photon Calculation*. Boca Raton: CRC Press., 1991. ISBN: 9780849360749.

[61] K. Kanaki et al. "Simulation tools for detector and instrument design". *Physica B: Condensed Matter* 551 (2018), pp. 386–389. ISSN: 0921-4526. DOI: 10.1016/j.physb.2018.03.025.

[62] K. Kanaki et al. "Detector rates for the Small Angle Neutron Scattering instruments at the European Spallation Source". *J. Instrum.* 13.07 (2018), P07016. DOI: 10.1088/1748-0221/13/07/p07016.

[63] I. Stefanescu et al. "Performance study of the Jalousie detector baseline design for the ESS thermal powder diffractometer HEIMDAL through GEANT4 simulations". *J. Instrum.* 14.10 (2019), P10020–P10020. DOI: 10.1088/1748-0221/14/10/p10020.

[64] M. Klausz et al. *A study of the indirect geometry cold neutron spectrometer, BIFROST, from neutron source position to detector position*. 2020. arXiv: 2004.00335 [physics.ins-det].

[65] K. Lefmann and K. Nielsen. "McStas, a general software package for neutron ray-tracing simulations". *Neutron News* 10.3 (1999), pp. 20–23. DOI: 10.1080/10448639908233684.

[66] P. Willendrup, E. Farhi, and K. Lefmann. "McStas 1.7 - a new version of the flexible Monte Carlo neutron scattering package". *Physica B: Condensed Matter* 350.13, Supplement (2004). Proceedings of the Third European Conference on Neutron Scattering, E735–E737. ISSN: 0921-4526. DOI: 10.1016/j.physb.2004.03.193.

[67] P. Willendrup et al. *User and Programmers Guide to the Neutron Ray-Tracing Package McStas, version 2.6*. P72–P73. Jan. 2020. URL: http://mcstas.org/documentation/manual/mcstas-2.6-manual.pdf.

[68] *McStas model of the ESS LoKI instrument*. URL: https://bitbucket.org/europeanspallationsource/nosg-baselines/src/dev/LOKI/Optics/McStas/.

[69] *McStas model of the ESS butterfly moderator*. URL: http://mcstas.org/download/components/sources/ESS_butterfly.html.

[70] *McStas model of the ESS BIFROST instrument*. URL: https://bitbucket.org/europeanspallationsource/nosg-baselines/src/dev/BIFROST/Optics/McStas/.

[71] S. Agostinelli et al. "GEANT4: A Simulation toolkit". *Nucl. Instrum. Methods Phys. Res. A* A506 (2003), pp. 250–303. DOI: 10.1016/S0168-9002(03)01368-8.

[72] J. Allison et al. "Geant4 developments and applications". *IEEE Trans. Nucl. Sci.* 53 (2006), p. 270. DOI: 10.1109/TNS.2006.869826.

[73] J. Allison et al. "Recent developments in Geant4". *Nucl. Instrum. Methods Phys. Res. A* (2016). DOI: 10.1016/j.nima.2016.06.125.

[74] T. Kittelmann et al. "Geant4 based simulations for novel neutron detector development". *J. Phys: Conf. Ser.* 513 (2014), p. 022017. DOI: 10.1088/1742-6596/513/2/022017.

[75] X.-X. Cai and T. Kittelmann. "NCrystal: A library for thermal neutron transport". *Computer Physics Communications* 246 (2020), p. 106851. ISSN: 0010-4655. DOI: 10.1016/j.cpc.2019.07.015.

[76] T. Kittelmann et al. "Monte Carlo Particle Lists: MCPL". *Computer Physics Communications* 218 (2017), pp. 17–42. DOI: 10.1016/j.cpc.2017.04.012.

[77] *MCPL documentation and GitHub repository*. 2017. URL: https://mctools.github.io/mcpl/.

[78] E. Knudsen et al. "McXtrace: A Monte Carlo software package for simulating X-ray optics, beamlines and experiments". *Journal of Applied Crystallography* 46 (June 2013), pp. 679–696. DOI: 10.1107/S0021889813007991.

[79] T. Sato et al. "Features of Particle and Heavy Ion Transport code System (PHITS) version 3.02". *Journal of Nuclear Science and Technology* 55.6 (2018), pp. 684–690. DOI: 10.1080/00223131.2017.1419890.

[80] C. J. Werner (editor). *MCNP Users Manual - Code Version 6.2*. Tech. rep. LA-UR-17-29981. Los Alamos National Laboratory, 2017.

[81] E. Nilsson et al. "Beam Dynamics Simulation with an Updated Model for the ESS Ion Source and Low Energy Beam Transport". In: *Proc. 10th International Particle Accelerator Conference (IPAC'19), Melbourne, Australia, 19-24 May 2019*. 10. 2019, pp. 1042–1045. ISBN: 978-3-95450-208-0. DOI: 10.18429/JACoW-IPAC2019-MOPTS083.

[82] D. Pfeiffer et al. "Interfacing Geant4, Garfield++ and Degrad for the simulation of gaseous detectors". *Nucl. Instrum. Methods Phys. Res. A* 935 (2019), pp. 121–134. ISSN: 0168-9002. DOI: 10.1016/j.nima.2019.04.110.

[83] D. Pfeiffer et al. "First Measurements with New High-Resolution Gadolinium-GEM Neutron Detectors". *J. Instrum.* 11 (2016), P05011. DOI: doi:10.1088/1748-0221/11/05/P05011.

[84] O. Arnold et al. "Mantid – Data analysis and visualization package for neutron scattering and μ SR experiments". *Nucl. Instrum. Methods Phys. Res. A* 764 (2014), pp. 156–166. ISSN: 0168-9002. DOI: 10.1016/j.nima.2014.07.029.

[85] E. Dian et al. "Scattered neutron background in thermal neutron detectors". *Nucl. Instrum. Methods Phys. Res. A* 902 (2018), pp. 173–183. ISSN: 0168-9002. DOI: 10.1016/j.nima.2018.04.055.

[86] F. Piscitelli et al. "The Multi-Blade Boron-10-based neutron detector for high intensity neutron reflectometry at ESS". *J. Instrum.* 12 (2017), p. 03013. DOI: 10.1088/1748-0221/12/03/P03013.

[87] I. Stefanescu et al. "Neutron Detectors for the ESS diffractometers". *J. Instrum.* 12 (2016), P01019. DOI: 10.1088/1748-0221/12/01/P01019.

[88] D. Raspino. *Performance of boron lined straw tubes*. URL: http://icnd.org/index.php?article_id=15&file=raspino_strasbourg_2016.pdf. 2016.

[89] A. Athanasiades et al. "Straw detector for high rate, high resolution neutron imaging". In: *IEEE Nuclear Science Symposium Conference Record, 2005*. Vol. 2. 2005, pp. 623–627. DOI: 10.1109/NSSMIC.2005.1596338.

[90] G. Croci et al. "Measurements of γ-ray sensitivity of a GEM based detector using a coincidence technique". *J. Instrum.* 8.04 (2013), P04006–P04006. DOI: 10.1088/1748-0221/8/04/p04006.

[91] A. Khaplanov et al. "Investigation of gamma-ray sensitivity of neutron detectors based on thin converter films". *J. Instrum.* 8 (2013), P10025. DOI: 10.1088/1748-0221/8/10/P10025.

[92] G. Mauri et al. "Fast neutron sensitivity of neutron detectors based on Boron-10 converter layers". *J. Instrum.* 13.03 (2018), P03004–P03004. DOI: 10.1088/1748-0221/13/03/p03004.

[93] F. Piscitelli and P. Van Esch. "Analytical modeling of thin film neutron converters and its application to thermal neutron gas detectors". *J. Instrum.* 8 (2013), P04020. DOI: 10.1088/1748-0221/8/04/P04020.

[94] F. Piscitelli. "Boron-10 layers, Neutron Reflectometry and Thermal Neutron Gaseous Detectors". PhD thesis. University of Perugia – Institut Laue-Langevin, 2014. arXiv: 1406.3133 [physics.ins-det].

[95] Á. C. Basaez, K. Kanaki, and F. Piscitelli. "DECal, a Python tool for the efficiency calculation of thermal neutron detectors based on thin-film converters" (2018). arXiv: 1801.07124 [physics.comp-ph].

[96] *NCrystal: a library for thermal neutron transport in crystals*. URL: https://github.com/mctools/ncrystal/wiki.

[97] MakeItFrom.com, 5754 aluminium. URL: https://www.makeitfrom.com/material-properties/5754-AlMg3-3.3535-A95754-Aluminum/.

[98] E. Dian et al. "Neutron activation and prompt gamma intensity in Ar/CO_2-filled neutron detectors at the European Spallation Source". *Applied Radiation and Isotopes* 128 (Jan. 2017). DOI: 10.1016/j.apradiso.2017.06.003.

[99] The Lund/LBNL Nuclear Data Search. URL: http://nucleardata.nuclear.lu.se/toi/.

[100] ESS-0019931, rev. 3. *ESS Procedure for designing shielding for safety*. 2017.

[101] R. Firestone et al. "Database of prompt gamma rays from slow neutron capture forelemental analysis" (Jan. 2007). DOI: 10.2172/882898.

[102] G. Galgczi et al. "Investigation of neutron scattering in the Multi-Blade detector with Geant4 simulations". *J. Instrum.* 13 (Dec. 2018), P12031–P12031. DOI: 10.1088/1748-0221/13/12/P12031.

[103] E. Dian et al. "Suppression of intrinsic neutron background in the Multi-Grid detector". *J. Instrum.* 14.01 (2019), P01021–P01021. DOI: 10.1088/1748-0221/14/01/p01021.

[104] T. Kittelmann et al. "Using Backscattering to Enhance Efficiency in Neutron Detectors". *IEEE Transactions on Nuclear Science* 64.6 (2017), pp. 1562–1573. ISSN: 0018-9499. DOI: 10.1109/TNS.2017.2695404.

[105] J. Mayers. "The use of vanadium as a scattering standard for pulsed source neutron spectrometers". *Nucl. Instrum. Methods Phys. Res.* 221.3 (1984), pp. 609–618. ISSN: 0167-5087. DOI: 10.1016/0167-5087(84)90073-5.

[106] J. Mayers. "Contribution of inelastic scattering to the vanadium differential scattering cross section; implications for the calibration of neutron spectrometers". *Nucl. Instrum. Methods Phys. Res. A* 281.3 (1989), pp. 654–656. ISSN: 0168-9002. DOI: 10.1016/0168-9002(89)91504-0.

[107] R. Toft-Petersen and L. Whitelegg. *BIFROST – analyser designs*. URL: https://indico.esss.lu.se/event/1043/attachments/310/466/BIFROST_AnalyzerDesign_Ver2.pdf.

[108] L. Whitelegg and R. Toft-Petersen. *BIFROST Detectors Requirements Specification*. Unpublished internal document.

[109] K. Kanaki and M. Klausz. *Rate limitations for LoKI detectors && costing tables*. LoKI Phase 2 review. 2017. URL: https://indico.esss.lu.se/event/831/sessions/3163/attachments/6366/9104/Detectors_loki_phase2_review_20170628.pdf.

[110] J. L. Lacy et al. "Boron-Coated Straw Neutron Imaging Detector Testing at the CSNS". In: *2019 IEEE Nuclear Science Symposium and Medical Imaging Conference (NSS/MIC)*. 2019, pp. 1–3.

[111] R. T. Kouzes et al. "Neutron detection alternatives to 3He for national security applications". *Nucl. Instrum. Methods Phys. Res. A* 623.3 (2010), pp. 1035–1045. ISSN: 0168-9002. DOI: 10.1016/j.nima.2010.08.021.

[112] B. M. van der Ende et al. "Use of GEANT4 vs. MCNPX for the characterization of a boron-lined neutron detector". *Nucl. Instrum. Methods Phys. Res. A* A820 (2016), pp. 40–47. DOI: 10.1016/j.nima.2016.02.082.

[113] E. R. Siciliano and R. T. Kouzes. "Boron-10 Lined Proportional Counter Wall Effects" (May 2012). DOI: 10.2172/1039851.

[114] G. Ehlers et al. "Performance tests of boron-coated straw detectors with thermal and cold neutron beams". *Nucl. Instrum. Methods Phys. Res. A* 953 (2020), p. 163238. ISSN: 0168-9002. DOI: 10.1016/j.nima.2019.163238.

[115] M. D. Le et al. "Gains from the upgrade of the cold neutron triple-axis spectrometer FLEXX at the BER-II reactor". *Nucl. Instrum. Methods Phys. Res. A* 729 (2013), pp. 220–226. ISSN: 0168-9002. DOI: 10.1016/j.nima.2013.07.007.